Constrained Thorough Search 法による

複雑な系における EXAFS 解析の研究

Study on analysis for EXAFS data of complex structures using constrained thorough search method

城戸　大貴
Daiki Kido

Division of Quantum Science and Engineering,
Graduate School of Engineering, Hokkaido University

December, 2020

Contents

List of Abbreviations

CF :	Curve Fitting
CTS	Constrained Thorough Search
DFT :	Density Functional Theory
DXASF :	Dispersive X-ray Absorption Fine Structure
E-R mechanism :	Eley-Rideal mechanism
EM method :	Equation of Motion method
EXAFS :	Extended X-ray Absorption Fine Structure
HRTEM :	High Resolution Transmission Electron Microscope
IR :	Infrared
LEED :	Low Energy Electron Diffraction
L-H mechanism :	Langmuir-Hinshelwood mechanism
MD	Molecular Dynamics
m-RMC :	Micro Reverse Monte Carlo
PEFC :	Polymer Electrolyte Fuel Cell
QXAFS :	Quick X-ray Absorption Fine Structure
RMC :	Reverse Monte Carlo
SDD :	Silicon Drift Detector
SEM :	Scanning Electron Microscope
SSD :	Solid State Detector
STM :	Scanning Tunneling Microscope
TEM :	Transmission Electron Microscope
TS :	Thorough Search
UHV :	Ultra High Vacuum
UV :	Ultra Violet
XAFS :	X-ray Absorption Fine Structure
XANES :	X-ray Absorption Near Edge Structure
XAS :	X-ray Absorption Spectroscopy
XFEL :	X-ray Free Electron Laser

Chapter 1. General Introduction

1.1. Introduction

Catalysts are essential for daily life though people rarely see directly when these are working, for example, production of the fiber, desulfurization of exhaust gas, fuel cells and so on.[1,2] The noble example is Haber-Bosch process which produces ammonia using iron catalysts.[3,4] When this reaction was developed, the technique of nitrogen fixation is needed to solve the food problem. The Haber-Bosch process produces ammonia from nitrogen in the air. Therefore, this process was evolutionally at that time and F. Haber was awarded the 1918 Nobel Prize in Chemistry. In addition, Haber-Bosch process remains important processes today.[5] Though catalysts are used in wide field, higher efficiency than current status is hoped. It is because the part of high efficient catalysts is rare and expensive metals such as platinum or palladium. From the view of resource and industry, reducing the amount of such materials is demanded.

The role of catalysts is to help the chemical reaction without changing itself before and after the reaction. Catalysts not only promote the reaction but have selectivity of the product. Therefore, it is important that to consider the rate of reaction and selectivity for designing the more effective catalysts. In case of heterogeneous catalysts, the procedure of reaction is often described as the Langmuir-Hinshelwood (L-H) mechanism or Eley-Rideal (E-R) mechanism.[6-9] In L-H mechanism, both reactants adsorb to the surface of catalysts at first. Then they meet on surface and react. Finally, products desorb from catalysts. On the other hand, in E-R mechanism, one of the reactant adsorb to surface at first. Then another reactant hits the adsorbed one and reacts. Finally, products desorb from catalysts. In both mechanisms, catalysts changed itself during the reaction and promote the reaction. It was difficult to observe these processes directly a few decades ago though the mechanisms of catalytic reaction were described above. The mechanisms of catalytic reaction have been observed directly with the development of measurement method.

The surface science experiments such as Scanning Tunneling Microscope (STM), Low Energy Electron Diffraction (LEED) and so on have been developed in a few decades. The catalytic reaction is carried out on the surface of catalysts. Therefore, the characterizations of the surface on heterogeneous catalysts have been carried out.

These characterizations are carried out to the clean and single crystal surface under the Ultra High Vacuum (UHV) condition.[9,10] The clean condition is important to characterize precisely. The surface is easily contaminated and contaminations disturb the observation. The UHV condition is needed to avoid the adsorption of contamination from surroundings. Moreover, the interaction with support materials and catalysts are complex so that single crystal has been used as well defined system to make observation simply. In the ambient condition, it is also difficult to achieve the high resolution of measurement such as High Resolution Transmission Electron Microscope (HRTEM) because the electrons interact with gases. Therefore, the initial state of catalysts has been investigated under the UHV condition and characterized. Though such measurement is important to characterize the catalysts, the gaps which are called the "pressure gap" and the "material gap" remain between these ideal condition and real reactive conditions. In addition, catalysts are changed its structure and electronic state during the reaction continuously and come back to the initial state after the whole reaction. Thus it has been demanded that the new techniques to observe the surface with high quality in real reactive conditions. There have been many developments in the measurement method. The good examples are the papers from G. Ertl who was awarded the 2007 Nobel Prize in Chemistry.[4,11-14] He has had a large contribute to reveal the mechanism of catalytic reaction. He reported that the mechanism about the ammonia synthesis using iron catalysts and oxidation of carbon monoxide using platinum surface. These measurements which were carried out under the reactive condition are called as *in situ*. Since around 1990, the reports about *in situ* measurement has been increasing as shown in Figure 1-1.[15,17] For example, the Transmission Electron Microscope (TEM) has also been developed and the environmental TEM for *in situ* measurement was reported.[19] In addition, *operando* measurements are paid attention, recently.[20-22] The *operando* measurements are the measurement not only under the reactive condition but evaluation for the catalytic activity or selectivity is carried out simultaneously. The reports concerned with *in situ* or *operando* measurement also has been increasing with the development of measurement techniques as shown in Figure 1-1.

X-ray Absorption Spectroscopy (XAS) is one of the powerful methods for *in situ* and *operando* measurement.[23-28] It is because the incident X-ray for metal samples is high energy and goes through the gas or the solution phase. In addition, XAS is element selective method. Even though under the difficult condition such as high pressure or high temperature for TEM or Scanning Electron Microscope (SEM), the information of the catalysts under the reactive condition can be obtained using XAS.

1.2. X-ray Absorption Fine Structure (XAFS)

X-ray Absorption Spectroscopy (XAS) is measurement of the absorption coefficient of a sample. This absorption coefficient is determined by the decay of incident X-ray intensity I_0 with distance t. According to the Beer-Lambert Law, the X-ray absorption coefficient μ is described using intensity I which is transmitted through the sample as following.

$$I = I_0 \mathrm{e}^{-\mu t} \tag{1-1}$$

When the absorption coefficient is plotted as a function of incident X-ray energy E, the spectrum shows the sharp rise called as absorption edges as shown in Figure 1-2. Thus the energy of absorption edge is different depending on element. Therefore, XAS is element selective method. These absorption edges are named as K, L_1, L_2, L_3, M_1, and so on, depending on the initial orbital of electron.

Figure 1-3 shows the sketch of correlation. Around absorption edge, there is a fine oscillation structure and it is called as X-ray Absorption Fine Structure (XAFS). The structure near the absorption edge is called as X-ray Absorption Near Edge Structure (XANES) and higher energy region from 50 eV to 1000 eV is called as Extended X-ray Absorption Fine Structure (EXAFS). The information of electronic state and structure around X-ray absorbing atoms can be obtained from XAFS. The detail of each region is described later.

There are some advantages of XAFS compared with other methods. 1. In case of high energy X-ray for observing the metals, the allowed conditions around the sample is wide. High energy X-ray can go through the air or the solution so that *in situ* or *operando* measurement can be carried out. Thus XAFS can be applied to high temperature or high pressure condition.[29,30] 2. The sample is not need the single crystal. Even though the powder or the solution sample, measurements can be carried out. 3. XAFS is element specific so that the information of aimed element is extracted. 4. The information of the valence of X-ray absorbing atom and the structure around it can be obtained at the same time. Thus the correlation of valence and structural change can be obtained. On the other hand, there are some disadvantages, of course. 1. The sample can be damaged by high energy X-ray. 2. It is very sensitive around X-ray absorbing atoms but it is difficult to obtain the information of far atoms. 3. Sometimes it is difficult to interpret the obtained data.

1.2.1. X-ray Absorption Near Edge Structure (XANES)

X-ray Absorption Near Edge Structure (XANES) is the structure around absorption edge of X-ray absorption spectrum. The process of X-ray scattering is multiple scattering. The main information which XANES tells is as following.

1. Valence state of X-ray absorbing atom

2. Structural symmetry around X-ray absorbing atom

In XANES region, an X-ray absorption is the excitation from inner orbital to outer unoccupied orbital. It means that the height or area of XANES is concerned with the number of outer unoccupied orbital. The valence of atom is changed with electron transfer of outer orbital. Therefore, the valence state of X-ray absorbing atom can be extracted from the height or area of XANES. In addition, XANES spectrum can be shift to higher or lower energy depending on the sample at same absorption edge. It can be indicator of valence change, too. On the other hand, XANES can also be affected by the structural symmetry around X-ray absorbing atom.[31,32] For example, in the case of W L_1-edge XANES as reported by Yamazoe *et al.*[32], the pre-edge region which appears the lower energy of main peak changes depending on the symmetry around W atom. The transition from inner orbital to outer orbital is mainly approximated by the dipole transition and the quadrupole transition. W L_1-edge XANES is mainly derived from electron transition from W 2s orbital to W 6p orbital in dipole transition approximation. On the other hand, in the dipole transition approximation, electron transition from W 2s orbital to W 5d orbital is forbidden. The quadrupole transition allows the electron transition from 2s orbital to 5d orbital though its effect is much weaker than dipole transition. In case of distorted octahedral symmetry around W atoms, 6p orbital can be mixed to 5d orbital from the group theory. As the result of mixing, the pre-edge peak appears in the W L_1-edge XANES spectrum affected by the quadrupole transition. In addition, the height or area of pre-edge region has a correlation with the symmetry around W atom. Therefore, the information of symmetry around X-ray absorbing atom can be extracted from XANES region.

1.2.2. Extended X-ray Absorption Fine Structure (EXAFS)

Extended X-ray Absorption Fine Structure (EXAFS) refers to the oscillation appearing from 50 eV to 1000 eV above the X-ray absorption edge. It provides a local structure around the X-ray absorbing atom. The main information can be obtained from EXAFS is as following.

1. Bond lengths between X-ray absorbing atom and surrounding atoms

2. Coordination number of X-ray absorbing atom

3. The element of neighbor atom from X-ray absorbing atom

The oscillation of EXAFS was quantitative parametrized by Sayers *et al.* at 1971[33] and it has been represented by following equation.

$$\chi(k) = S_0^2 \sum_i \frac{N_i \cdot F_i(k)}{k \cdot r_i^2} \exp(-2k^2 \cdot {\sigma_i}^2) \cdot \sin\big(2k \cdot r_i + \varphi_i(k)\big)$$

$$k = \sqrt{\frac{2m}{\hbar^2}(E - E_0)}$$

(1-2)

Here, parameters are N_i is the coordination number, r_i is the interatomic length, ${\sigma_i}^2$ is the Debye Waller factor which is term for static disorder and thermal effect, and E_0 is correction of the origin of kinetic energy zero. In addition, $F_i(k)$ is the backscattering amplitude, $\varphi_i(k)$ is the phase shift of final state, and S_0^2 is inelastic loss factor. In the conventional analysis method (Curve fitting method), this Equation (1-2) is used to calculate the EXAFS oscillation. The introduction of Equation (1-2) is described in Section 1.2.3.

1.2.3. Introduction of the equation of EXAFS

Here, simple interpretation of EXAFS is described based on Ref.24,34-36. The K-edge X-ray absorption process which an electron is excited from s_1 orbital is considered to explain simply. The detail of EXAFS interpretation needs the electron scattering theory of quantum physics and described some papers and textbooks.[37,38]

The X-ray absorption process is excitation of electron from inner orbital. When the Hamiltonian which doesn't include the interaction from X-ray is written as $\mathcal{H}$, Schrödinger equation in the steady state is written using wave function Ψ and eigenenergy E as

$$\mathcal{H}\Psi_j = E_j\Psi_j \,.$$

(1-3)

When Born-Oppenheimer approximation is introduced, $\mathcal{H}$ and Ψ are Hamiltonian and wave function for all electrons, respectively. In Born-Oppenheimer approximation, the movement of nuclei is considered as enough slower than the movement of electron. When the Hamiltonian which doesn't include the interaction from X-ray is written as $\mathcal{H}'$, the X-ray absorption coefficient μ is proportional function according to Fermi's golden rule.

$$\mu \propto \sum_f \left|\langle \Psi_f | \mathcal{H}' | \Psi_i \rangle\right|^2 \delta\left(E_f - E_i - \hbar\omega\right) \tag{1-4}$$

Here, Ψ_i and Ψ_f are the wave function of initial state and final state with their energy are E_i and E_f, respectively. $\hbar$ is Dirac's constant and δ is Dirac's delta function. When the one-electron approximation is introduced, the Hamiltonian $\mathcal{H}'$ is written as

$$\mathcal{H}' = -\frac{e}{mc} A(\boldsymbol{r}) \cdot \boldsymbol{p} \,. \tag{1-5}$$

Here, $\boldsymbol{p}$ is the momentum operator, $A(\boldsymbol{r})=\hat{\mathbf{e}}A_0 e^{i\boldsymbol{k}\cdot\boldsymbol{r}}$ is the vector potential of the incident electromagnetic field, m is mass of an electron, c is a velocity of light, e is an elementary charge. $\boldsymbol{r}$ and $\hat{\mathbf{e}}$ are positional vector of photoelectron and unit vector of electronic field of X-ray. X-ray absorption process is deep-core excitation process so that dipole approximation can be applied. In dipole approximation, the spatial dependence of the electromagnetic field can be neglected because the wavelength of X-ray can be considered that it is larger than the expansion of wave function of electrons which lies inner shell. Therefore, $e^{i\boldsymbol{k}\cdot\boldsymbol{r}}$ is approximated to 1. In addition, commutation relation $[\boldsymbol{r}, \mathcal{H}]$ is approximate to $(i\hbar/m)\boldsymbol{p}$. Equation (1-4) becomes as

$$\mu \propto \sum_f \left|\langle \Psi_f | \hat{\mathbf{e}} \cdot \boldsymbol{r} | \Psi_i \rangle\right|^2 \delta\left(E_f - E_i - \hbar\omega\right) \,. \tag{1-6}$$

The wave function of initial state Ψ_i and final state Ψ_f is necessary to describe the EXAFS oscillation. Ψ_f is described mainly two wave functions, wave function of photoelectron Ψc which comes from X-ray absorbing atom and wave function of scattered electron Ψsc which comes from neighboring atoms.

$$\Psi_f = \Psi_c + \Psi_{sc} \tag{1-7}$$

Here, two atoms which are X-ray absorbing atom (atom A: O(0,0,0)) and neighbor X-ray scattering atom (atom B: (0,0,R)) is considered as a simple model. A photoelectron which comes from atom A is scattered only one time at atom B. In polar coordinate system, wave function of photoelectron in the initial state is written as

$$\Psi_i(\boldsymbol{r}) = R_{l_0}(r)\Omega_{l_0}(\hat{\boldsymbol{r}}) \tag{1-8}$$

Here, $R_{l_0}(r)$ and $\Omega_{l_0}(\hat{\boldsymbol{r}})$ are radial coordinate and angular coordinate, respectively, and $\hat{\boldsymbol{r}}$ is unit vector. In K-edge absorption process, l_0=0 and $\Omega_{l_0}(\hat{\boldsymbol{r}})$=$1/\sqrt{4\pi}$. The term $\hat{\mathbf{e}} \cdot \boldsymbol{r}$ in Equation (1-6) is written using spherical harmonics function $Y_{l,m}(\hat{\boldsymbol{r}})$ as

$$\hat{\mathbf{e}} \cdot \boldsymbol{r} = r\left[\sqrt{\frac{2\pi}{3}}\sin\theta_0\left\{Y_{1,-1}(\hat{\boldsymbol{r}}) - Y_{1,1}(\hat{\boldsymbol{r}})\right\} + \sqrt{\frac{4\pi}{3}}\cos\theta_0 Y_{1,0}(\hat{\boldsymbol{r}})\right],$$

and

$$Y_{1,0} = \sqrt{\frac{3}{4\pi}}\cos\Theta$$

$$Y_{1,1} = -\sqrt{\frac{3}{8\pi}}\sin\Theta \mathrm{e}^{i\Phi}$$

$$Y_{1,-1} = \sqrt{\frac{3}{8\pi}}\sin\Theta \mathrm{e}^{-i\Phi} \tag{1-9}$$

Here, Θ and Φ are angular coordinate of $\hat{\boldsymbol{r}}$.

As the potential energy of atom A and B, Muffin-tin approximation is introduced. Muffin-tin approximation consider that potential energy around the atom is spherical symmetry within the radius $r_{mt,A}$ and $r_{mt,B}$ region, on the other hand the potential energy is constant out of radius $r_{mt,A}$ and $r_{mt,B}$ region as shown in Figure 1-4. When the spherical potential energy around atom A is written as $v_A(r)$, the Schrödinger equation for photoelectron from X-ray absorbing atom is described as

$$\left\{-\frac{\hbar^2}{2m}\nabla^2 + v_A(r)\right\}\Psi_c = E\Psi_c \,. \tag{1-10}$$

The X-ray absorbing atom A within the radius $r_{mt,A}$, potential energy is spherical symmetry so that the wave function ${\Psi_c}^{in}$ is written using radial coordinate and angular coordinate like Equation (1-11).

$$ {\Psi_c}^{in}(\boldsymbol{r}) = R_l(r)\Omega_l(\hat{\boldsymbol{r}}) \tag{1-11} $$

In case of K-edge X-ray absorption, the azimuthal quantum number is only l=1 because the l=1 is allowed in dipole approximation but l=0 is forbidden. The potential $v_A(r)$ is spherical symmetry so that $\mu = \left|\langle\Psi_f|\hat{\mathbf{e}}\cdot\boldsymbol{r}|\Psi_i\rangle\right|^2$ should be independent from $\hat{\mathbf{e}}$. From the comparison of Equation (1-9), angular coordinate is written using spherical harmonics function $Y_{l,m}(\hat{\boldsymbol{r}})$.

$$ \Omega_l(\hat{\boldsymbol{r}}) = \frac{i}{2}\left\{Y_{1,-1}(\hat{\boldsymbol{r}}) - Y_{1,1}(\hat{\boldsymbol{r}})\right\} + \frac{1}{\sqrt{2}}Y_{1,0}(\hat{\boldsymbol{r}}) \tag{1-12} $$

Ψ_c in Equation (1-7) is this ${\Psi_c}^{in}$.

To introduce the wave function of scattered photoelectron Ψsc, the processes; (1) ${\Psi_c}^{out}$ which is photoelectron goes to neighbor atom B from X-ray absorbing atom A, (2) ψ_{in} which is photoelectron goes to neighbor atom B, (3) ψ_{SC} which is electron scattering at neighbor atom B, (4) ψ_{sc} which is scattered electron comes to X-ray absorbing atom A, have to be considered. The wave function of photoelectron out of radius $r_{mt,A}$ region, ${\Psi_c}^{out}$, can be described from ${\Psi_c}^{in}$. It is because the wave function have to be continuous at the r=$r_{mt,A}$. When the travelling wave goes to neighbor atom B with δ_l^A phase advance and comes back to X-ray absorbing atom A with δ_l^A phase delay, the wave function out of $r_{mt,A}$ is written as

$$ {\Psi_c}^{out} = C\left\{h_l(kr)\mathrm{e}^{i\delta_l^A} + h_l^*(kr)\mathrm{e}^{-i\delta_l^A}\right\}\Omega_l(\hat{\boldsymbol{r}}) \ . \tag{1-13} $$

Here, C is a factor for normalization, $h_l(kr)$ and $h_l^*(kr)$ are Hankel function. From this ${\Psi_c}^{out}$, the wave function of process (2) photoelectron goes to neighbor atom B can be written. The $h_l(kr)$ term shows the wave which go out to neighbor atom B, on the other hand, $h_l^*(kr)$ term shows the wave which comes back to X-ray absorbing atom A. Thus, the component which goes to neighbor atom B in ${\Psi_c}^{out}$ is

$$\psi_{in}(\boldsymbol{r}) = Ch_l(kr)\mathrm{e}^{i\delta_l^A}\Omega_l(\hat{\boldsymbol{r}})$$

(1-14)

In addition, Hankel equation is approximate as following under the $kr \gg 1$

$$h_l(kr) \sim (-i)^{l+1}\frac{\mathrm{e}^{ikr}}{kr}$$

(1-15)

From this approximation, wave function can be approximated to plane wave. When Θ=0 and Φ=0, $\Omega_l(\hat{r})$ is calculated from Equation (1-12) as

$$\Omega_l(\hat{r}) = \frac{i}{2}\{0-0\} + \frac{1}{\sqrt{2}}\sqrt{\frac{3}{4\pi}} = \sqrt{\frac{3}{8\pi}}$$

(1-16)

Then, the wave function of photoelectron which reached to the neighbor atom B which is at $\boldsymbol{R}$ is calculated from Equation (1-14).

$$\psi_{in}(\boldsymbol{r} \sim \boldsymbol{R}) = \sqrt{\frac{3}{8\pi}}Ch_l(kR)\mathrm{e}^{i\delta_l^A}\mathrm{e}^{i\boldsymbol{k}\cdot\boldsymbol{r}_\mathrm{B}}$$

(1-17)

Here, origin of positional vector is atom B and $\boldsymbol{r}$-$\boldsymbol{R}$ is represented as $\boldsymbol{r}_B$. In Equation (1-17), $\mathrm{e}^{i\boldsymbol{k}\cdot\boldsymbol{r}_\mathrm{B}}$ term shows the plane wave and expanded as

$$\mathrm{e}^{i\boldsymbol{k}\cdot\boldsymbol{r}_\mathrm{B}} = \sum_{l''}^{\infty}(2l''+1)i^{l''}j_{l''}(kr_B)P_{l''}(\cos\theta)\ .$$

(1-18)

Here, $j_{l''}(kr_B)$ is spherical Bessel function, $P_{l''}(\cos\theta)$ is Legendre polynominal, θ is scattering angle and $|\boldsymbol{r}_\mathrm{B}|$ is represented as r_B. This spherical Bessel function is

$$j_{l''}(kr_B) = \frac{1}{2}\left\{h_{l''}(kr_B) + h_{l''}^*(kr_B)\right\}.$$

(1-19)

The photoelectron geos to neighbor atom B with its wave function ψ_{in} and scattered. ψ_{sc} is the wave function of scattered photoelectron at atom B under the $v_B(r\text{-}R)$

potential energy. The travelling wave goes to neighbor atom B with $\delta_{l''}^{B}$ phase advance and comes back to X-ray absorbing atom A with $\delta_{l''}^{B}$ phase delay so that the wave function of scattered photoelectron ψ_{sc} is $2\delta_{l''}^{B}$ phase advance compared with ψ_{in}. Interference of ψ_{in} and ψ_{sc} is considered and spherical Bessel function becomes

$$j_{l''}(kr_B) = \frac{1}{2} h_{l''}(kr_B)\left(\mathrm{e}^{2i\delta_{l''}^{B}} - 1\right) .$$

(1-20)

Then, ψ_{sc} is written as,

$$\psi_{sc}(\boldsymbol{r}) = \sqrt{\frac{3}{8\pi}} C h_l(kR)\mathrm{e}^{i\delta_l^A} \sum_{l''}^{\infty} (2l''+1) i^{l''} j_{l''}(kr_B) P_{l''}(\cos\theta)$$

$$= \sqrt{\frac{3}{8\pi}} C h_l(kR)\mathrm{e}^{i\delta_l^A} \sum_{l''}^{\infty} (2l''+1) \widetilde{t_{l''}^{B}} P_{l''}(\cos\theta)\, h_{l''}(kr_B) .$$

(1-21)

Here,

$$\widetilde{t_{l''}^{B}} = \frac{1}{2i}\left(\mathrm{e}^{2i\delta_{l''}^{B}} - 1\right) = \mathrm{e}^{i\delta_{l''}^{B}} \sin\delta_{l''}^{B} .$$

(1-22)

ψ_{sc} is described superposition of waves which have azimuthal quantum number l''. $\widetilde{t_{l''}^{B}}$ term describes the photoelectron scattering for each azimuthal quantum number l''.

ψ_{sc} represents the plane wave of scattered photoelectron which comes from atom B to atom A. The term reached to X-ray absorbing atom A is important in ψ_{sc}. In this case, the scattered angle θ is π. Around the X-ray absorbing atom A is $kr_B \gg 1$ condition so that $h_{l''}(kr_B) \sim \mathrm{e}^{ikr_B}/r_B$. The wave function ψ_{sc} around atom A (0,0,0) is approximated as,

$$\psi_{sc}(\boldsymbol{r} \sim \boldsymbol{0}) = \sqrt{\frac{3}{8\pi}} C h_l(kR)\mathrm{e}^{i\delta_l^A} \frac{\mathrm{e}^{ikr_B}}{r_B} f_B(\pi) .$$

(1-23)

Here, $f_B(\pi)$ is backscattering amplitude.

$$f_B(\pi) = \frac{1}{k}\sum_{l''}^{\infty}(2l''+1)\widetilde{t_{l''}^{B}}P_{l''}(\cos\theta)$$

$$= \frac{1}{2ik}\sum_{l''}^{\infty}(2l''+1)\,(\mathrm{e}^{2i\delta_{l''}^{B}}-1)(-1)^{l''}$$

(1-24)

ψ_{sc} is needed to considered from X-ray absorbing atom A not neighbor atom B. The origin of position vector and azimuthal quantum number are replaced as

$$\psi_{sc}(\boldsymbol{r}) = \sum_{l'}\sum_{m'=-l'}^{l'}\alpha_{l',m'}2j_{l'}(kr)Y_{l',m'}(\hat{\boldsymbol{r}}) \quad .$$

(1-25)

Equation (1-23) is also written using expansion of plane wave function.

$$\psi_{sc}(\boldsymbol{r}\sim\boldsymbol{O})\sim\sqrt{\frac{3}{8\pi}}Ch_l(kR)\mathrm{e}^{i\delta_l^A}f_B(\pi)\cdot 4\pi ik\sum_{l'}\sum_{m'=-l'}^{l'}j_{l'}(kr)h_{l'}(kR)Y_{l',m'}(\hat{\boldsymbol{r}})Y_{l',m'}^{*}(\widehat{\boldsymbol{R}})$$

(1-26)

From the comparison of Equation (1-25) and (1-26),

$$\alpha_{l',m'} = \sqrt{\frac{3\pi}{2}}ikC\{h_l(kR)\}^2\mathrm{e}^{i\delta_l^A}f_B(\pi)\cdot Y_{l',m'}^{*}(\widehat{\boldsymbol{R}})$$

(1-27)

The azimuthal quantum number l' is 1 when K-edge X-ray absorption. Therefore, $Y_{l',m'}^{*}(\widehat{\boldsymbol{R}})$ is calculated only for l'=1 and m'=-1,0,1 at atom A (0,0,0) (Θ=π and Φ=0).

$$Y_{1,0}^{*}(\hat{\boldsymbol{R}}) = \sqrt{\frac{3}{4\pi}}\cos\Theta \; = \sqrt{\frac{3}{4\pi}}$$

$$Y_{1,1}^{*}(\hat{\boldsymbol{R}}) = -\sqrt{\frac{3}{8\pi}}\sin\Theta \mathrm{e}^{i\Phi} = 0$$

$$Y_{1,-1}^{*}(\hat{\boldsymbol{R}}) = \sqrt{\frac{3}{8\pi}}\sin\Theta \mathrm{e}^{-i\Phi} = 0$$

(1-28)

Then,

$$\alpha_{1,1} = \alpha_{1,-1} = 0$$

$$\alpha_{1,0} = \frac{3}{2\sqrt{2}} ikC\{h_l(kR)\}^2 \mathrm{e}^{i\delta_l^A} f_B(\pi)$$

(1-29)

When the travelling wave goes to X-ray absorbing atom A with $\delta_{l'}^{A}$ phase advance and comes back to neighbor atom B with $\delta_{l'}^{A}$ phase delay, the wave function out of $r_{mt,A}$ is written as

$$\Psi_{sc}{}^{out}(\boldsymbol{r}) = \alpha_{1,0}\left\{h_{l'}(kr)\mathrm{e}^{2i\delta_{l'}^{A}} + h_{l'}^{*}(kr)\right\} Y_{1,0}(\hat{\boldsymbol{r}}) \ .$$

(1-30)

Therefore, within $r_{mt,A}$, the wave function of scattered electron is written as

$$\Psi_{sc}{}^{in}(\boldsymbol{r}) = \alpha_{1,0}\mathrm{e}^{i\delta_{l'}^{A}} R_{l'}(r) Y_{1,0}(\hat{\boldsymbol{r}}) \ \ .$$

(1-31)

Finally, wave function of scattered electron Ψsc which comes from neighboring atom is described as following using Equation (1-11) and (1-31).

$$\begin{aligned}\Psi_f &= \Psi_c + \Psi_{sc} = \Psi_c{}^{in} + \Psi_{sc}{}^{in} \\ &= R_{l'}(r)\{\Omega_l(\hat{\boldsymbol{r}}) + XY_{1,0}(\hat{\boldsymbol{r}})\}\end{aligned}$$

(1-32)

here,

$$X = \alpha_{1,0} \mathrm{e}^{i\delta_{l'}^{A}} \xrightarrow{kR \gg 1} \frac{3}{2\sqrt{2}} i(-1)^{l'+1} \frac{\mathrm{e}^{2ikR}}{kR^2} f_B(\pi) \mathrm{e}^{i(\delta_l^A + \delta_{l'}^A)}$$

(1-33)

From these calculations, the Fermi's Golden rule which is described as Equation (1-4) becomes,

$$\begin{aligned}
&\mu = \mu_0\{1 + 2\sqrt{2}\cos^2\theta_0 \mathrm{Re}(X)\} \\
&\mu_0 \propto |\langle \Psi_c | \hat{\mathbf{e}} \cdot \boldsymbol{r} | \Psi_i \rangle|^2 \\
&\quad = \left| \int_0^\infty R_l^*(kr) R_{l_0}(kr) r^3 dr \int_0^{2\pi} \int_0^\pi \Omega_l^*(\hat{\boldsymbol{r}})\, \hat{\mathbf{e}} \cdot \hat{\boldsymbol{r}} \Omega_{l_0}^*(\hat{\boldsymbol{r}}) \sin\theta d\theta d\phi \right|^2 \\
&\quad = \frac{1}{6} \left| \int_0^\infty R_l^*(kr) R_{l_0}(kr) r^3 dr \right|^2
\end{aligned}$$

(1-34)

Here, μ_0 is the absorption coefficient of isolated atom. In equation of μ, term of X^2 is ignored because one scattering process is discussed here. EXAFS oscillation $\chi(k)$ is calculated from $(\mu - \mu_0)/\mu_0$ as,

$$\chi(k) = 2\sqrt{2}\cos^2\theta_0 \mathrm{Re}(X) = -\frac{3\cos^2\theta_0}{kR^2} \mathrm{Im}\left\{ \mathrm{e}^{2ikR + 2i\delta_l^A} f_B(\pi) \right\}.$$

(1-35)

The EXAFS equation for K-edge X-ray absorption was introduced to consider the two atoms and one scattering process. In reality, electrons interact with one another. Thus, effects as following have to be considered.

- Intrinsic loss factor : S_0^2
- Mean free path : λ
- Thermal vibration (Debye Waller factor) : σ^2

The effect of other coordinated atom around X-ray absorbing atom can be considered to sum up $\chi(k)$ for each bond.

Intrinsic loss factor : S_0^2

This factor originates from multielectron excitation. This is many-body effect. The kinetic energy of photoelectron becomes smaller than simple one electron excitation. This process occurs when the inner electron is excited before the photoelectron is scattered. S_0^2 affects the amplitude of EXAFS oscillation $\chi(k)$. Its

value is typically around 0.7-1.0. In EXAFS analysis, this factor is assumed from reference sample and used for aimed sample.

Mean free path : λ

This factor originates from inelastic scattering of photoelectron. This effect is described as mean free path of photoelectron, λ, and $e^{-2R/\lambda(k)}$ term. The wave number of photoelectron is reduced due to the inelastic scattering. Thus $e^{-2R/\lambda(k)}$ term affects the amplitude of EXAFS oscillation $\chi(k)$. In EXAFS analysis, this factor calculated in FEFF code. This factor is called as extrinsic loss factor compared with intrinsic loss factor.

Thermal vibration (Debye-Waller factor) : σ^2

Thermal vibration of atoms is also considered. This factor is called as Debye Waller factor. Thermal vibration makes fluctuation of bond length. When the distribution of fluctuation $\rho(r)$ is approximated to Gaussian function, Debye Waller factor, σ^2, is written as,

$$\rho(r) = \frac{1}{\sqrt{2\pi}\sigma} e^{-\frac{(r-R)^2}{2\sigma^2}} \quad . \tag{1-36}$$

Here, Debye Waller factor is deviation of Gaussian distribution. From the deconvolution of Equation (1-35) and (1-36), the thermal average of $\chi(k)$ is written as,

$$\langle\chi(k)\rangle = -\frac{3\cos^2\theta_0}{kR^2} \mathrm{Im}\left\{e^{2i\delta_l^A} f_B(\pi)\langle e^{2ikR}\rangle\right\}$$

and

$$\langle e^{2ikR}\rangle = \frac{1}{\sqrt{2\pi}\sigma}\int_0^\infty e^{2ikR-\frac{(r-R)^2}{2\sigma^2}} dr \cong e^{2ikR} e^{-2\sigma^2k^2} \tag{1-37}$$

From this equation, the fluctuation of bond length affects the amplitude of EXAFS oscillation as a $e^{-2\sigma^2k^2}$ term. Debye Waller factor is introduced as a fluctuation due to the thermal vibration, here. In addition to thermal vibration, Debye Waller factor also includes the static disorder of bond length. In practical, a more accurate expansion is needed including asymmetric system for real system such as surface atoms compared with bulk. This factor is considered using cumulant expansion.[39] In this

thesis, Debye Waller factor is considered from Gaussian distribution.

Finally, including these factors, equation of EXAFS is written as,

$$\chi(k) = -S_0^2 \sum_j \frac{N_j}{kR_j^2} F_j(k) \mathrm{e}^{-2\sigma_j^2 k^2} \sin\{2kR_j + \varphi_i(k)\} \quad .$$

(1-38)

Here, j means the shell. When there is the same element in the same bond length, it can be treated as one shell. Though the same bond length, different element is treated as different shell. The term of back scattering amplitude $f_B(\pi)$ in Equation (1-35) is written as $F_j(k)\mathrm{e}^{i\phi_j(k)}$. The term of phase shifts are summed up as $\varphi_i(k) = 2\delta_1^A + \phi_j(k)$ for simplicity. Mean free path of photoelectron λ is included to back scattering amplitude $F_j(k)$ and phase shift $\varphi_i(k)$. Equation (1-38) is for the unoriented sample. In case of oriented sample, coordination number N_j is written by effective coordination number.

In case of L-edge X-ray absorption

The K-edge X-ray absorption is assumed above. In case of L-edge X-ray absorption, the initial state of electron is p orbital. Thus, the azimuthal quantum number l_0=1. In dipole approximation for Ψ_c and Ψ_{sc}, allowed excitation is l=0, 2 and l'=0, 2, respectively. Though the details are omitted here, finally the EXAFS equation is written as,

$$\chi(k) = S_0^2 \sum_j \frac{N_j}{kR_j^2} F_j(k) \mathrm{e}^{-2\sigma_j^2 k^2} \sin\{2kR_j + \varphi_i(k)\} \ .$$

(1-39)

1.3. *In situ* or *operando* time-resolved XAFS measurement

XAFS can be applied to time-resolved measurement. The standard measurement system is called as step scan mode, the energy of incident X-ray is changed step by step and the signal is accumulated certain seconds. The technique to obtain time-resolved spectra and its time resolution are different in each method. The systems of measurement and features are introduced below.

1.3.1. Quick XAFS (QXAFS)

In Quick XAFS (QXAFS) method, monochromator which monochromatizes the incident X-ray is moved continuously and the spectra are obtained. Thus the loss of time is less than step scan mode. QXAFS method is proposed by Frahm in 1988.[40] QXAFS measurement is carried out by synchronize between the continuous move of monochromator and the signal processing. The special equipment is not necessary and many beamlines which can carry out the step scan mode can adopt the QXAFS measurement. Thus QXAFS measurement can be carried out for dilute sample with fluorescence mode. The time resolution is second to minute order as usual when the system for step scan mode is used. The time resolution is decided by mechanical part which is the continuous move of monochromator or time resolution of detector. In Japan, Nonaka *et al.* reported the 10 ms time resolution at beamline BL33XU on SPring-8 in 2012.[41] In addition, Sekizawa *et al.* reported the improvement and 800 μs time resolution was achieved at beamline BL36XU on SPring-8 in 2013.[42]

1.3.2. Dispersive XAFS (DXAFS)

In Dispersive XAFS (DXAFS) method, XFFS spectrum is obtained in one shot of X-ray.[43] DXAFS method is proposed by Matsushita in 1981.[44] DXAFS measurement is carried out using white X-ray which focused by polychromator and 2D detector which has the position resolution. The incident X-ray is focused on sample then dispersed by polychromator. The transmitted X-ray is detected by 2D detector so that the position of detection is corresponding to the energy of X-ray. Spectrum is obtained in one shot so that DXAFS is appropriate to trace the irreversible process and fragile sample which broken by X-ray. Optical arrangement of DXAFS gives the stability of the energy scale and focal spot position during the measurement. However, the measurement is limited to transmission mode so that dilute sample is hard to measure. The measurable range of EXAFS is limited by the energy width of polychromator. Intensity of incident X-ray is measured the same optics without the sample. The energy resolution is decided by precision of polychromator and positional resolution of detector. The time resolution is mainly decided by the speed of detection on the detector and data processing. The nanosecond order time resolution was reported at European Synchrotron Radiation Facility (ESRF), in France.[45]

1.3.3. Pump-probe XAFS

Pump-probe method is used for IR or UV time resolved measurement.[46-48] The pump laser is irradiated to the sample for excitation and then the probe laser is irradiated

to observe the excited state of sample with some delay. In case of pump-probe XAFS method, probe is X-ray and XAFS spectrum for the excited state of sample is obtained.[49-52] Time resolution is decided by the pulse width of laser or X-ray, mechanical part, or speed of data processing. When synchrotron radiation is used as X-ray source, the pulse width is scale of picosecond so that the time resolution is often picosecond order. Recently, new X-ray source called as X-ray Free Electron Laser (XFEL) has been available, for example, SACLA at SPring-8 in Japan.[53-56] The pulse width of X-ray obtained from XFEL is less than femtosecond order so that the femtosecond or shorter than femtosecond timeresolved measurement is expected from the view of X-ray pulse width. However, the time resolution is a few femtosecond because of the limitation of other parts.

1.3.4. *In situ* or *operando* time resolved XAFS measurement

The mechanism of reaction can be observed to combine *in situ* or *operando* measurement with time resolved measurement system.[57] For example, Tada *et al.* reported the *operando* QXAFS measurement for Polymer Electrolyte Fuel Cell (PEFC) catalysts.[58] They traced the change of Pt based cathode catalysts (Pt/C, Pt_3Co/C and Pt_3Ni/C) during the voltage cycling from Pt L_3-edge XAFS. The time resolution was 100 ms for XANES and 500 ms for EXAFS, respectively. The change of valence was obtained from the white line height of XANES. At the same time, the change of coordination number and bond length from Pt were obtained from the curve fitting analysis of EXAFS. In addition, they combined *operando* QXAFS technique with CT imaging technique and investigate the chemical kinetics and dynamics of Pt based cathode catalysts, recently.[59]

Time resolved XAFS methods are selected depending on the change of sample. At first, the scale of time which can observe the change of sample has to be considered. For example, QXAFS is the best way for millisecond to minute range measurement. Second is how to change the sample. When the trigger for changing is temperature, pump-probe measurement can be carried out using the pump laser for temperature increasing. However, precise control of temperature is difficult and the equipment to release the heat during the repetition of pump-probe measurement is needed. Third is concentration of sample. Though QXAFS and pump-probe XAFS can be applied for fluorescence mode, DXAFS can be carried out only the transmission mode. Therefore, it is difficult to carry out DXAFS method for diluted sample.

1.4. Analysis method for EXAFS

As mentioned above, EXAFS provides the information of structure around X-ray absorbing atom. To obtain the information, curve fitting (CF) method is generally used after the data processing such as background removal, normalization, Fourier transformation, and inversely Fourier transformation. In this section, I would like to introduce the detail of CF method and point out its problems. In addition, I would like to introduce other analysis method such as ratio method, grid search method and (micro) Reverse Monte Carlo ((m-)RMC) method.

1.4.1. Curve fitting (CF) method

EXAFS is usually analyzed using non-linear least square fitting method.[60,61] This method is often called as curve fitting (CF) method. Equation (1-2) is used to fit the observed data so that parameters are coordination numbers(N), correction of the origin of kinetic energy zero(ΔE_0), bond lengths(r) and Debye Waller factors(σ^2). The flowchart of CF method is as shown in Figure 1-5. The backscattering amplitude and phase shift in Equation (1-2) is calculated by FEFF code.[38] The residual of EXAFS oscillation between the experimental data and calculated one is minimized in the CF method. The degree of fitting is evaluated by R-factor as shown in Equation (1-40).

$$R-\text{factor}=\frac{\sum_i\left\{k^n\cdot\chi_{data,i}(k)-k^n\cdot\chi_{calculated,i}(k)\right\}^2}{\sum_i\left\{k^n\cdot\chi_{data,i}(k)\right\}^2} \tag{1-40}$$

Here, χ_{data} and $\chi_{calculated}$ were EXAFS oscillation of experimental data and calculated one, respectively, k^n was weighted value and n=0, 1, 2, or 3. The region of R-factor calculation was the k-range which used for Fourier transformation. These definitions were the same as REX2000 program (RIGAKU).[62,63] In conventional analysis program, REX2000 and Artemis [64] applied the Levenberg-Marquardt method for least square method. Though CF analysis is widely used for EXAFS analysis, there are some problems especially in case of the complex molecule.

Problem 1. Limitation of parameters

The degree of freedom, M, for fitting parameters is determined by Nyquist theory.[65]

$$M = \frac{2\Delta k \Delta r}{\pi} + \alpha \quad (\alpha = 0,1,2)$$

(1-41)

Here, Δk and Δr are the region when the observed data is Fourier and inversely Fourier transformed. When the CF analysis is carried out in r space, Δr is the range of CF analysis. Equation (1-41) is introduced from consideration of the finite Fourier transformation. Degree of freedom is a fundamental limitation to the amount of information that how many parameters can be determined by an EXAFS spectrum. Thus the number of searching parameters on CF analysis must not exceed this degree of freedom to obtain reliable results. From Equation (1-41), it is expected that the way to increase the degree of freedom is to measure as large a k range as possible at EXAFS measurement. The EXAFS oscillation damps at high k region because 1: the scattering ability of the surrounding atom for the electron with high k wave numbers (or large momenta) becomes small, 2: the reduction factors of 1/k term in the Equation (1-2), and 3: Debye Waller factor due to the thermal and static disorder. The thermal disorder can be reduced by the low temperature measurement. The EXAFS measurement at low temperature is recommended to obtain the high k-region data with a good quality. However, the limitation of degrees of freedom can be problem for complex system. For example, MoO_3 or WO_3 which has 6 metal-oxygen bonds demands 24 parameters to analyze each bond separately. Even though the 3-20 $Å^{-1}$ k-region can obtained from low temperature measurement, the degrees of freedom is around 18. Therefore, the limitation of degrees of freedom becomes problem for complex system. In addition, if the number of parameters can be increased enough, another problem, or the correlation of parameters, becomes conspicuous.

Problem 2. Correlation of parameters

As mentioned above, 4 parameters such as coordination numbers, correction of the origin of kinetic energy zero, bond lengths and Debye Waller factors are mainly searched in CF analysis. There are correlations among the structural parameters.[66-68] CF analysis is carried out to find the minimum of R-factor. Here, n dimensional parameter vector, $\boldsymbol{p}$, is defined whose components are fitting parameters $(p_1, p_2, p_3, \cdots p_n)$ where the number of fitting parameters is n. The function of R-factor is written as $R(\boldsymbol{p})$ and the residual $\delta\varepsilon_r(k_i)$ is defined as

$$\chi_{calculated}(k_i, \boldsymbol{p}) - \chi_{data}(k_i) = \delta\varepsilon_r(k_i)$$

$$\sum \delta\varepsilon_r(k_i)^2 = \sum |\chi_{calculated}(k_i, \boldsymbol{p}) - \chi_{data}(k_i)|^2$$
$$= R^2(\boldsymbol{p}) \sum |\chi_{data}(k_i)|^2 = R^2(\boldsymbol{p}) \cdot Const = R'^2(\boldsymbol{p})$$

(1-42)

After the CF analysis, the optimal parameters are determined as $\boldsymbol{p_f}$. Around the $\boldsymbol{p_f}$, $R'^2(\boldsymbol{p})$ can be expanded in a Talyor series. Since the

$$\frac{\partial R'^2(\boldsymbol{p_f})}{\partial p_i} = 0 \ \ (i = 1,2,3,\cdots,n) \ ,$$
$$R'^2(\boldsymbol{p}) = R'^2(\boldsymbol{p_f}) + \sum_{i,j}^{n} \frac{\partial^2 R'^2(\boldsymbol{p_f})}{\partial p_i \ \partial p_j} \Delta p_i \Delta p_j$$

(1-43)

and,

$$R'^2(\boldsymbol{p}) = R'^2(\boldsymbol{p_f}) + \sum_{i,j}^{n} B_{ij} \Delta p_i \Delta p_j$$

(1-44)

If the non-diagonal term, $B_{ij} = 0, (i \neq j)$, there is no correlation between the fitting parameters. In contrast, when $B_{ij} \neq 0, (i \neq j)$, there is a correlation. The correlations of parameters can be considered from Equation (1-2) when a single shell analysis. For amplitude of $\chi(k)$, coordination number and Debye Waller factor are mainly related. And inelastic loss factor (S_0^2) is also related to the amplitude of $\chi(k)$. For phase of $\chi(k)$, on the other hand, the correction of the origin of kinetic energy zero and bond length are mainly related. In addition, from the definition, Debye Waller factor correlates with bond length. Therefore, all parameters can correlate with each other. Correlation of parameters sometimes makes CF analysis unstable or prevents from converging to physically meaningful results. Even if the results of CF analysis give a reasonably low *R*-factor, it would be hard to exclude the other structural parameters. Teo *et al.* suggested one of the solutions that predetermine the values from analysing model compound as FABM (Fine Adjustment Based on Model Compounds) approach.[66] However, it cannot be applied to the unknown sample which its neighbour atoms' elements cannot be estimated exactly. In addition, even though the parameters are reduced by reference compound, the complex systems demands many

shells and sometimes make it hard to obtain reasonable results.

Problem 3. Dependence of initial parameters

The CF analysis requires the initial parameters, from which the algorism is started to reduce the *R*-factor efficiently. In case of complex molecules, dimension of structural parameters are increased. Thus the region which gives low *R*-factor can be also increased and local minima of *R*-factor are produced in the parameter space. In CF analysis, parameters are searched non-liner least square method, or using the steep of parameter space. If a local minimum has enough depth to trap the parameter searching, the parameters can converge to the local minimum not global minimum and difficult to escape.[69] When the fitting result is trapped at the wrong or meaningless local minimum, it is necessary to change the initial parameters to confirm the obtained minimum is not due to the local minimum but the global one or to search for the other possible structures. It is not the serious problem in a simple system with one coordination shell present with a symmetric distribution. The fitting result often gives the global minimum because the *R*-factor doesn't have local minima. The problem becomes serious in the complicated system where multi-shell fitting is necessary. In this case, the parameter dependence of the *R*-factor becomes small or B_{ij} in Equation (1-44) is small so that the shape of *R*-factor becomes dull and a tiny perturbation changes the *R*-factor minimum position easily. Moreover, the correlation between the parameters may give the physically unreasonable minimum. For example, in case of Mo/SiO_2 catalyst, Kikutani[70] pointed out that the possibility of local minimum of CF analysis about the bond length between the two molybdenum atoms which Iwasawa *et al.*[71] reported. It is difficult to decide the appropriate structural model only from the EXAFS in this case because both results reproduced experimental data well. Such differences of the results in CF analysis are often depending on initial parameter. It means if CF analysis starts certain parameter near a local minimum, the result is different from the case which the CF analysis starts near the global minimum. In addition, there is no guarantee that the obtained result is global minimum or not.

1.4.2. Ratio method

In the ratio method, the amplitude component and phase component are separated using Fourier transformation.[24,72-75] Then, these component compared with standard such as the result from the reference sample or theoretical calculation. The equation is described as following.

$$\ln(A) = \ln\frac{A_i(k)}{A_s(k)} = \ln\frac{N_i}{N_s} + \ln\frac{{r_s}^2}{{r_i}^2} - 2({\sigma_i}^2 - {\sigma_s}^2)\cdot k^2$$
$$\Phi = \Phi_i(k) - \Phi_s(k) = 2k(r_i - r_s) \tag{1-45}$$

Here, A and Φ were amplitude and phase shift, respectively. The index i and s were experimental data of unknown sample and standard sample. From the Φ vs k plot, the bond length is obtained and the correction of the origin of kinetic energy zero can be calculated. From the ln(A) vs k^2 plot, coordination number and Debye Waller factor were obtained. When these plots don't show the linearity, third and fourth cumulant component is added to Φ and A, respectively. Thus the ratio method can treat asymmetric distributions of radial distribution function. The advantage of the ratio method is to treat the correlation of parameters easier than the CF method. And to obtain the parameters which reproduce the experimental data within a specified error bar from the entire volume of parameter space. However, the ratio method can be applied only when the simple structure which the first shell consists of the same element and bond length. Therefore, the ratio method cannot be applied to the complex samples.

1.4.3. Grid search method

In grid search method, the parameters are surveyed step by step.[76] In the CF method, elegant method, or equations such as Levenberg-Marquardt method is used to search the parameters which reproduce the experimental data better than the initial parameter. The CF method shows the result quickly. On the other hand, in grid search method, parameter space is divided step by step and each point is compared one by one to search better parameter sets. This is time consuming and brute force method compared with CF method. However, it can obtain the existence of local minima in the survey region. Moreover, if large survey region is searched, it can avoid the dependence of initial parameter selection problem as mentioned Section 1.4.1. M. J. Schalken and C. T. Chantler carried out the grid search method for EXAFS analysis.[77] They analyzed Nickel coordination complexes successfully.

1.4.4. Reverse Monte Carlo method

Monte Carlo simulation is named after the town name Monte Carlo in Monaco famous for Casino. Monte Carlo simulation is based on the random walk to obtain the stable complex structures which all parts of the structures depend on each other. The energy, E_0 is calculated with one structure. Then the atomic positions are randomly

moved and the energy, E_1 of new structure is calculated. When the energy becomes smaller than the previous one, the new structure is accepted and then the structure is moved again from the new structure. On the other hand, when the energy becomes larger than the previous one, the new structure is accepted with the probability proportional to $\exp(-(E_1 - E_0)\beta)$. β is inverse proportional to the temperature or $\beta = 1/k_B T$(k_B is Boltzmann constant). If the new structure is rejected, the atom positions are returned to the previous one which is the starting point for the other new random walk. The system will reached stable state or no further change will occur in the energy, after all. This corresponds to the equilibrium at β. The structure at this equilibrium corresponds to the stable structure of the given system.

Reverse Monte Carlo (RMC) simulation uses the degree of fitting, *R*-factor, instead of energy, *E*. [78-86] RMC has been used for the analysis of X-ray and neutron scatterings where the medium range interaction is important. First the large number of atoms is prepared in a large box (called as cell) and then $R\text{-factor}_0$ is calculated for the initial atom positions in the large cell. The number of atoms in the box is more than 10^2-10^3. After the random walk, the new $R\text{-factor}_1$ is calculated for the new model. If $R\text{-factor}_1 < R\text{-factor}_0$, the new model is accepted for the next trial. Even if $R\text{-factor}_1 > R\text{-factor}_0$, the new model is accepted in the probability of the $\exp(-(R\text{-factor}_1 - R\text{-factor}_0)/\beta)$. Then the next calculation starts. The system reaches the equilibrium where no further improvement in *R*-factor after many cycles. The structure at the equilibrium is the final structure for this system. Thus the large number of atoms are contained in the large cell where the atoms move with the calculation of X-ray or neutron scattering intensity and the comparison with the experimental data by arrows shown in Figure 1-6(a). Revers Monte Carlo method has been applied to EXAFS analysis. In case of the EXAFS analysis, the nearest neighbour interaction is the most important so that it is not necessary to calculate the whole atomic pair in the large cell. Fujikawa *et al.* proposed a micro RMC (m-RMC) method.[87] In principle, the m-RMC method follows the conventional RMC procedure. In m-RMC, a large cell is divided into independent replica files each of which includes a small chemical species such as a molecule, a metal complex or a metal cluster as shown in Figure 1-6(b). The initial model structure in each replica file is assumed, and then m-RMC method is carried out using the set of replica files. Each replica file contains one molecule, one metal complex or one metal cluster as shown in Figure 1-6(b). A plenty number of replica files are prepared. Based on the structure in each replica file, $\chi^i_{calculated}(k)$ of the *i* th file is calculated. For the molecule, the central atom is regarded as X-ray absorbing atom and the others are treated as scattering

atoms. In the metal cluster which have several absorbing atoms. For example, in Au cluster, all Au atoms in Au nanoclusters are all absorbers and at the same time scatterers. The $\chi_{cal}^{i}(k)$ in the replica file is obtained from the initial configuration using the Equation (1-2). The $\chi_{calculated}^{i}(k)$'s are averaged up over all absorbing atoms in replica files to obtain the averaged $\chi_{calculated}(k)$. The averaged $\chi_{calculated}(k)$ is then compared with $\chi_{data}(k)$ to estimate the degree of fitting, *R*-factor. In order to avoid being trapped at the local minimum and to decrease the calculation time, β is set at a large value of approximately 10^2 at first. Then β is gradually decreased to obtain an accept/reject ratio nearly unity. After 10^4–10^5 steps of cycles, the *R*-factor reaches the equilibrium. Finally, the radial distribution function is calculated using all replica files. The flowchart of m-RMC is as shown in Figure 1-7. The cumulant coefficients from the final configurations are given by the following equations:

$$\begin{aligned} C_1 &= R = \langle r \rangle \\ C_2 &= \langle (r-R)^2 \rangle \\ C_3 &= \langle (r-R)^3 \rangle \ . \end{aligned} \tag{1-46}$$

Here, symbol 〈 〉 means the thermal average. The m-RMC can include the asymmetric distribution. Regulations of multi-edge analysis are automatically included. For example, the bond length of A-B must be the same when it is observed from the edge A or from the edge B since the same cluster structure is used for the analysis of both edges and hence the A-B bond length is always the same. The m-RMC method is the promising analysis technique even if the resolution is not so good as CF method.

1.4.5. Problem remaining in EXAFS analysis

The main problems in the CF analysis are 1. The limitation of degree of freedom, 2. The correlation of parameters, and 3. The dependence of initial parameter, as mentioned Section 1.4.1. The other problem remains for EXAFS analysis even though the other methods such as m-RMC method have the possibility to solve these problems. These analysis methods mainly aim to avoid the local minima and to obtain the global minimum as the result of EXAFS analysis. The best fit model looks the appropriate model from the EXAFS data. However, there is no insurance that the best fit model is consistent with other results, especially in case of complex systems such as aimed element has the 6 different bond lengths or it is surrounded by some elements. Main 4

parameters for EXAFS analysis have the correlations. The problems of local minima and initial parameter become remarkable in complex structure. In addition, there is a possibility that the local minima show the result which consistent with other results. Thus, the researchers should consider the whole parameter sets which reproduce the EXAFS in certain significance level. It is difficult to evaluate multidimensional parameter space. However, this problem becomes serious when the other experiment is difficult.

The estimation of error for each parameter also can be the problem. Ideally, the error of each data point, ε_i, should be estimated. The ε_i does not only include the probability(statistical) error which can be estimated from the statistical treatment of the data but also it contains the systematic (non-statistical) errors. Systematic errors arise from many uncontrollable origins so that the correct estimations are difficult. If the probability errors were larger than systematic errors, I could represent the errors ε_i^2 by the probability error. But the standard data quality obtained in synchrotron facilities in a transmission mode is very good and the probability errors can be neglected. The Hamilton test can be applied for error estimation using *R*-factor.[88] In Hamilton method, significance tests are allowed by *R*-factor ratio, $\Re=R_1/R_0$, where R_0 and R_1 are *R*-factor of a refinement model and another refinement model with additional constrained condition on some parameters, respectively. The ratio of *R*-factor is approximated to the ratio of two χ^2-distribution functions. Thus the ratio of *R*-factor is approximated to *F*-distribution as,

$$\Re_{b,M-n,\alpha} = \frac{R_1}{R_0} = \frac{b}{M-n} F_{b,M-n,\alpha} + 1 \quad . \tag{1-47}$$

Here, *M* is the degrees of freedom, *n* is the number of parameters which used to obtain the refinement model, *b* is the number of restrained parameters which used to obtain the refinement model with restraints on some parameters and $F_{b,M-n,\alpha}$ is *F*-distribution function for significance level α. For EXAFS analysis, the degree of freedom *M* is defined from Nyquist theory.[65] The null hypothesis for significance test is "the degree of fitting between experimental data and calculated spectrum is the same as that of the best fit one". Hamilton method is based on *F*-test. Therefore, statistical treatment for error estimation and comparison of two results are allowed. However, Hamilton method has two weak points especially for complex structure. 1: The obtained statistical significance is relative value between the best model and the other. When *R*-factor of the best model is large, worse models can be picked up. 2: When the

parameters are used as much as the degrees of freedom, $F_{b,M-n,\alpha}$ becomes larger and meaningless models which don't reproduce the experimental data can be picked up. Thus the large error can be obtained from such problems.

Another problem is asymmetry of distribution. The CF method is assumed that the radial distribution function is Gaussian or symmetric distribution as mentioned above. Therefore, the asymmetric distributed system with a large static disorder cannot be analyzed by the CF method, using the Equation (1-2). [89] In order to include the effect of asymmetry, one way is to use the asymmetric distribution function. The term $Ne^{-2\sigma^2 k^2}$ in Equation (1-2) can be replaced by asymmetric distribution function. However, it is not useful to introduce the asymmetric distribution function for the analysis. Therefore, if the asymmetry was not so large, cumulant expansion method is applied.[90] Though the number of fitting parameter is increased, the asymmetric distribution is well considered by cumulant expansion. As mentioned in Section 1.4.2 and 1.4.4, ratio method and (m-)RMC method can consider the asymmetric distribution using cumulant expansion for calculation.

1.5. Purpose of this thesis

XAFS is suitable technique to characterize the catalysts not only the initial state but during the reaction. XAFS gives the information about electronic state of X-ray absorbing atom and surrounding local structure. In addition, it can be applied to in-situ or operando measurement easier than other characterization method. High time-resolved measurements enable to trace the change of catalysts during the reaction. However, the conventional analysis of EXAFS, or curve fitting (CF) method, has three difficulties, 1. Limitation of parameters, 2. Correlation of parameters, 3.Dependence of initial parameter. The degrees of freedom for analysis are the limitation of information which one can obtain from an EXAFS spectrum in problem 1. Especially in the CF analysis, degrees of freedom limit the number of free parameters. This limitation cannot be overcome in the analysis phase. It can be improved only in the experimental phase. The quality of raw data decides the degrees of freedom mainly. On the other hand, problem 2 and 3 occur mainly in analysis phase and these become remarkable in case of complex system which demands many shells for analysis. In addition, another problem is remaining in EXAFS analysis method. The problems, most of analysis method aim to obtain the global minimum and gave up evaluating the whole parameter space, the estimation of error, and the treatment of asymmetric distribution remain. In

this thesis, I would like to propose the new analysis method, “Constrained thorough search (CTS)” method. The way of searching parameters is grid search method but challenge the treatment of multidimensional parameter space. CTS method is brute force method and takes long time to analyze spectra comparing with CF method even though it takes lower cost than m-RMC. However, CTS method gives fruitful results especially for complex systems. CTS method has a potential to make correlations of parameters visible, to avoid the dependence of initial parameter for analysis, and to pick up the all candidates which reproduce the experimental data well in the searched parameter space. The errors of each parameters are also shown with new criterion. In Chapter 2, I introduce the experimental setup for conventional XAFS measurement and fundamental treatment of observed data. In Chapter 3, I show the overview of CTS method and comparison with other analysis method through the analysis of Pt L_3-edge EXAFS of Pt foil and Mo K-edge EXAFS of MoO_3 as examples of simple structure and complex structure, respectively. From these results, the advantages and the disadvantages of CTS method is mentioned. In Chapter 4, I reveal the structural change of WO_3 photocatalyst in the photoexcited state from picosecond timeresolved W L_3-edge EXAFS spectra using CTS method. In Chapter 5, CTS method is applied to the analysis of PtRu bimetallic nanoparticles. In the EXAFS analysis of bimetallic materials, additional constrained conditions have two be considered among the parameters of two absorption edges. The general *R*-factor to combine the results obtained from each spectrum gave the meaningful results. In Chapter 6, I discuss the general conclusion of this thesis.

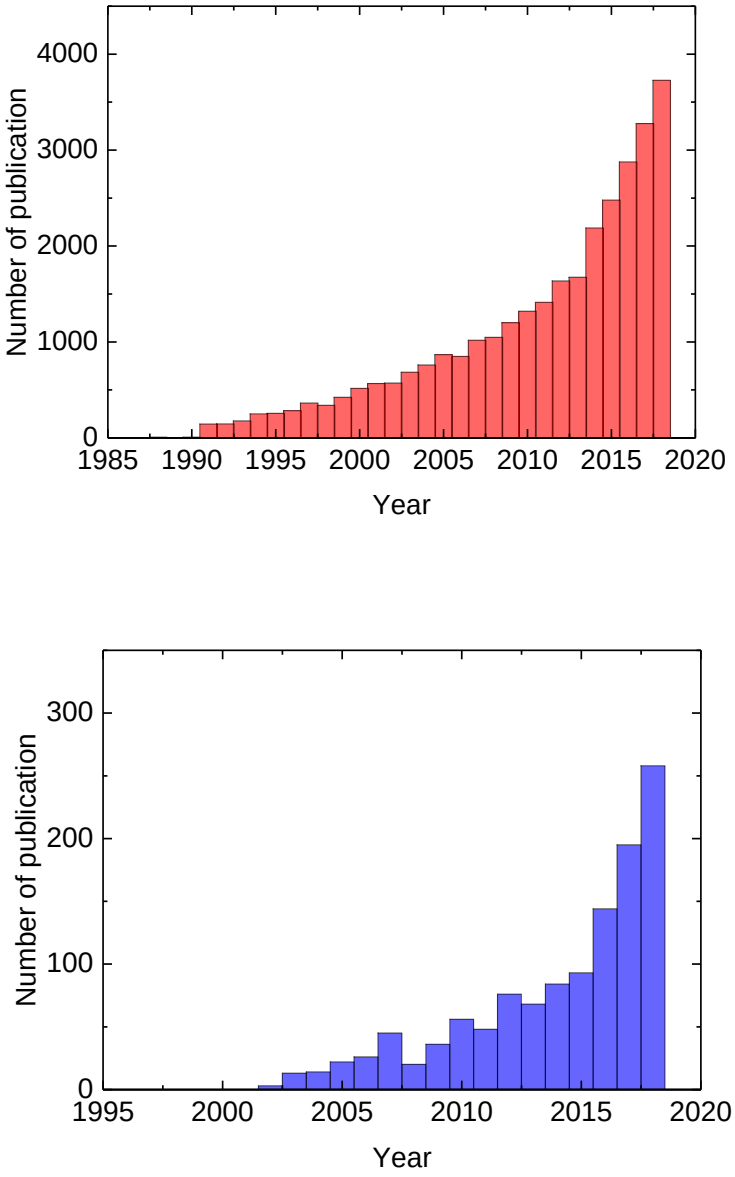

Figure 1-1. Number of publications when the words “catalyst” with “in-situ”(a) or “operando”(b) are searched as “topic” in Web of Science. The survey range of years was 1985-2018. This search was carried out at November 13th in 2019.

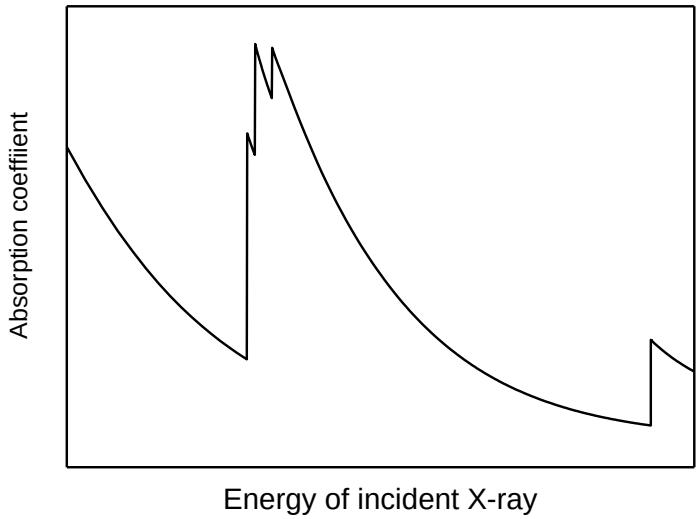

Figure 1-2. The correlation between energy of incident X-ray and absorption coefficient. The axis of energy is a logarithmic scale. This spectrum was calculated for Mo from database of X-ray absorption edges.

(URL:http://skuld.bmsc.washington.edu/scatter/AS_periodic.html)

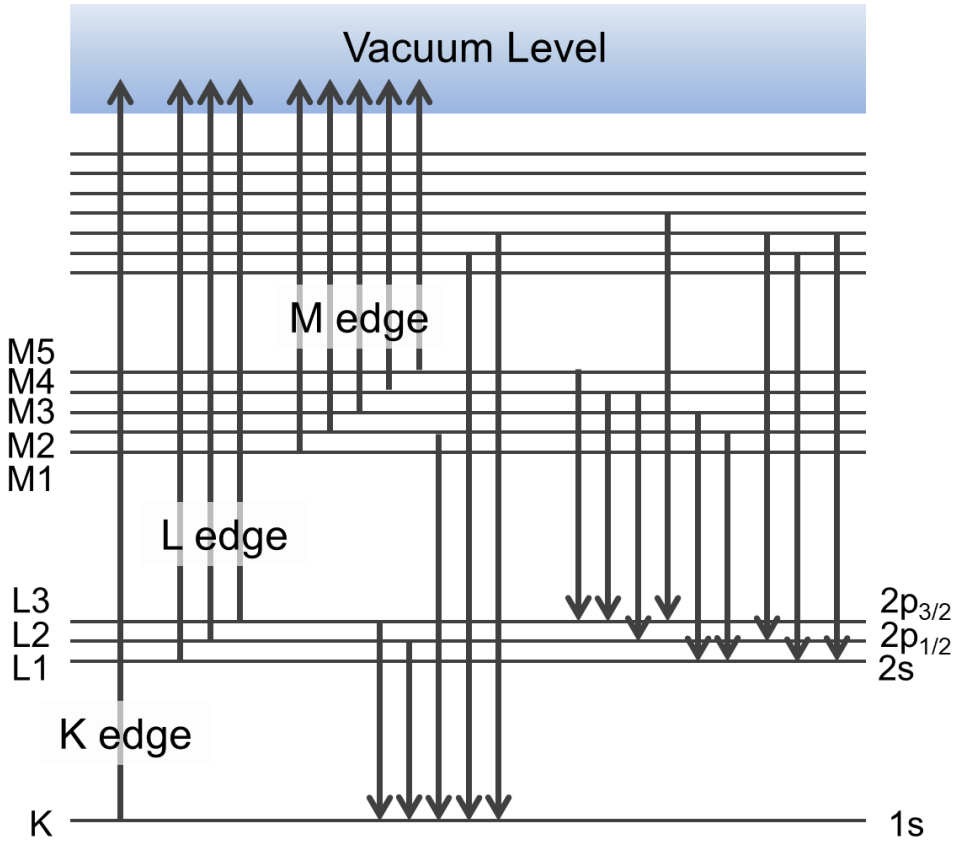

Figure 1-3. The sketch of X-ray absorption edge.

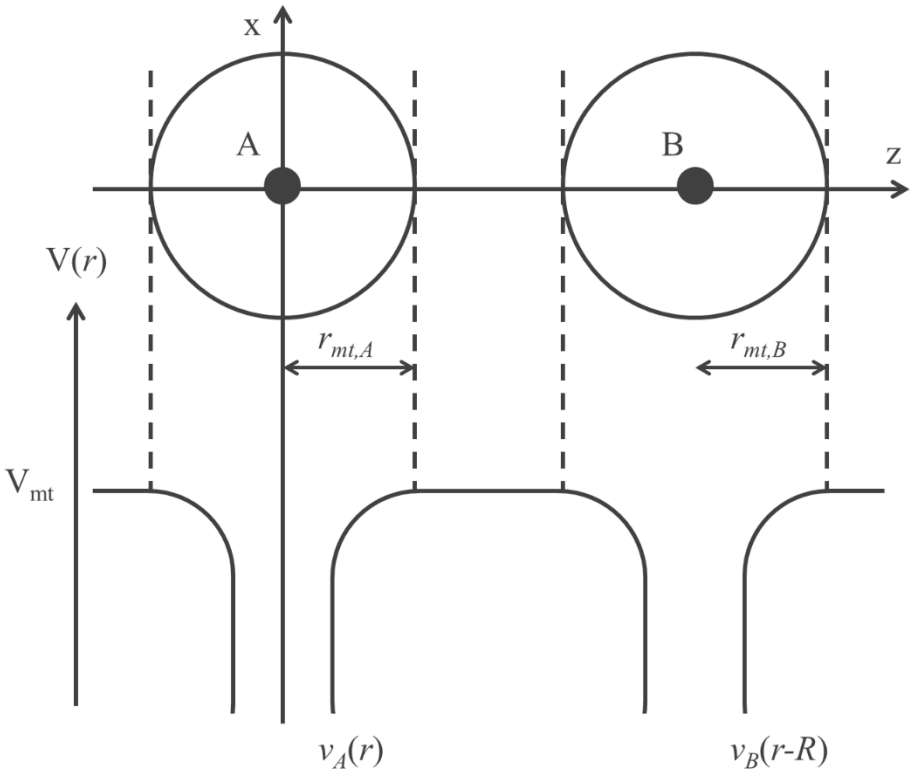

Figure 1-4. Muffin-tin approximation.

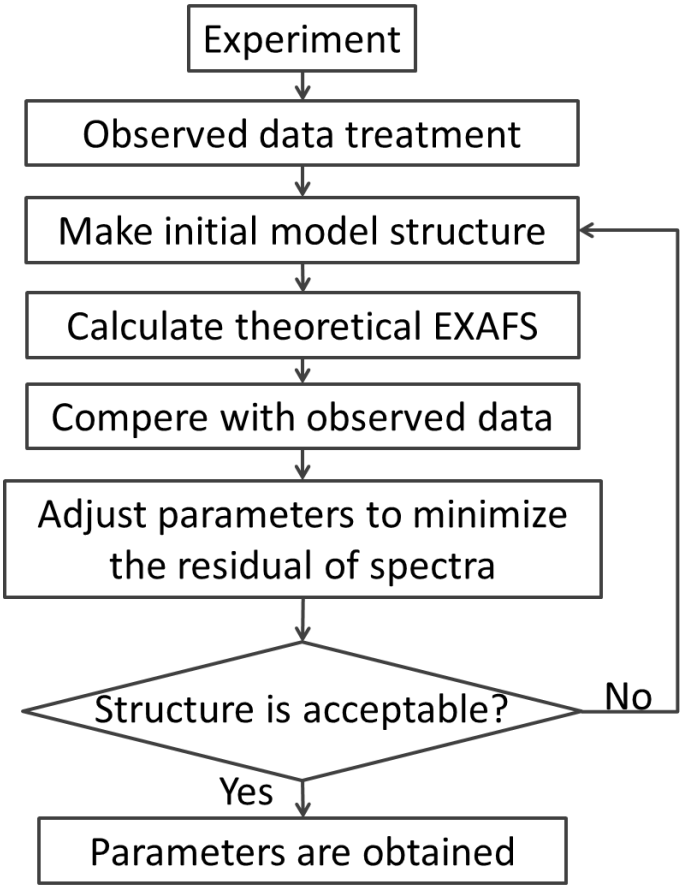

Figure 1-5. The flowchart for curve fitting (CF) analysis.

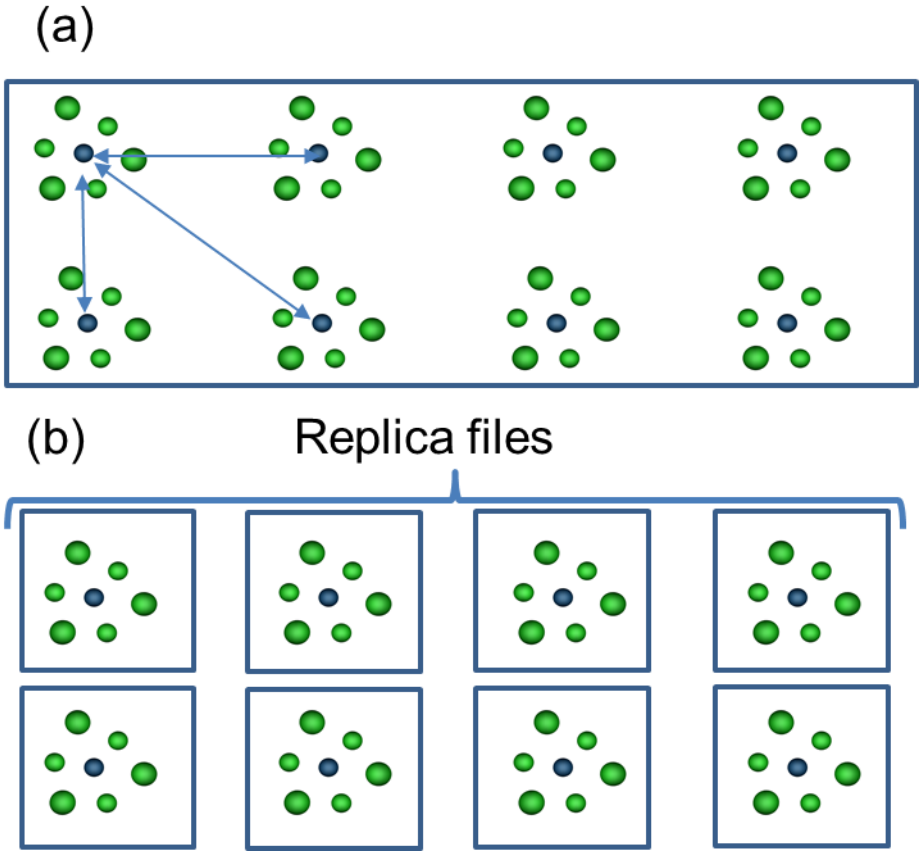

Figure 1-6. Caluculated cells in reverse Monte Carlo(RMC) (a) and micro reverse Monte Carlo(m-RMC)(b).

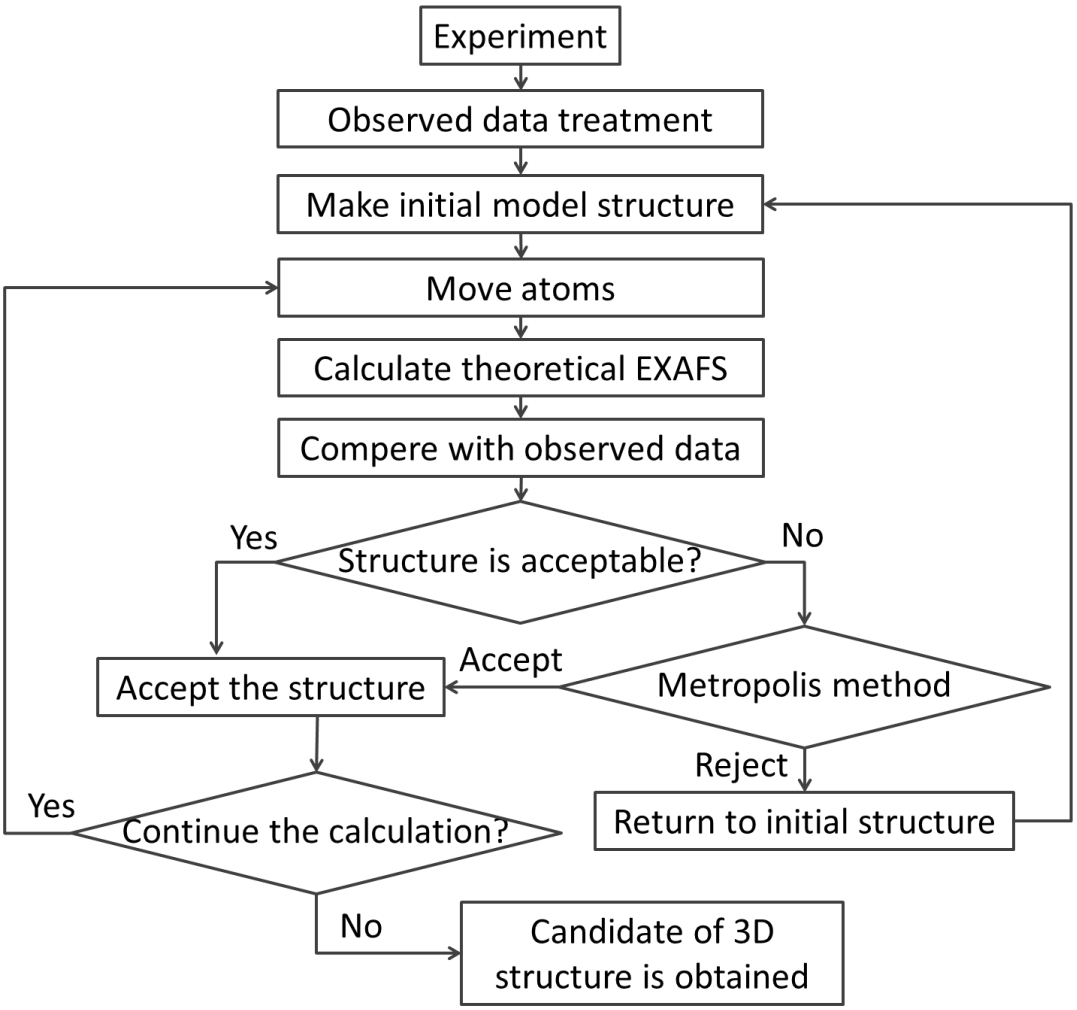

Figure 1-7. The flowchart for (micro-) reverse Monte Carlo analysis.

Reference

1. J. Hagen, Industrial catalysis : a practical approach, Wiley-VCH, Weinheim, New York, 1999.
2. J.H. Sinfelt, Role of surface science in catalysis, Surf. Sci., 500 (2002) 923-946.
3. K. Tamaru, in J. R. Jennings (Eds.) Catalytic Ammonia Synthesis Fundamentals and Practice, Plenum Press, 1991, p 1-17.
4. 日本表面科学会, 純. 久保田, 表面科学こと始め : 開拓者たちのひらめきに学ぶ, 共立出版, 東京, 2012.
5. J.W. Erisman, M.A. Sutton, J. Galloway, Z. Klimont, W. Winiwarter, How a century of ammonia synthesis changed the world, Nature Geoscience, 1 (2008) 636-639.
6. C.N. Hinshelwood, The kinetics of chemical change, Clarendon Press, Oxford, 1940.
7. D.D. Eley, E.K. Rideal, Parahydrogen Conversion on Tungsten, Nature (London), 146 (1940) 401-402.
8. Y. Iwasawa, J. Nakamura, K. Fukui, J. Yoshinobu, ベーシック表面化学, Kagaku-Dojin, Kyoto, 2010.
9. K.W. Kolasinski, Surface science : foundations of catalysis and nanoscience, 3rd ed., Wiley, Chichester, West Sussex, 2012.
10. G.A. Somorjai, Y. Li, Introduction to surface chemistry and catalysis, 2nd ed., John Wiley & Sons, Hoboken, N.J., 2010.
11. G. Ertl, Reactions at surfaces: From atoms to complexity (Nobel lecture), Angew. Chem. Int. Ed., 47 (2008) 3524-3535.
12. G. Ertl, Reactions at well-defined surfaces, Surf. Sci., 299-300 (1994) 742-754.
13. G. Ertl, Primary steps in catalytic synthesis of ammonia, J. Vac. Sci. Technol. A, 1 (1983) 1247-1253.
14. G. Ertl, ELEMENTARY STEPS IN HETEROGENOUS CATALYSIS, Angew. Chem. Int. Edit. Engl., 29 (1990) 1219-1227.
15. R. Schlögl, Heterogeneous catalysis, Angew. Chem. Int. Ed., 54 (2015) 3465-3520.
16. H.J. Freund, Model Studies in Heterogeneous Catalysis, Chem. Eur., 16 (2010) 9384-9397.
17. S. Takakusagi, K.-i. Fukui, R. Tero, K. Asakura, Y. Iwasawa, First Direct Visualization of Spillover Species Emitted from Pt Nanoparticles, Langmuir, 26 (2010) 16392-16396.
18. M.A. Bañares, Operando methodology: combination of in situ spectroscopy and simultaneous activity measurements under catalytic reaction conditions, Catal. Today, 100 (2005) 71-77.

19. J.B. Wagner, F. Cavalca, C.D. Damsgaard, L.D.L. Duchstein, T.W. Hansen, Exploring the environmental transmission electron microscope, Micron, 43 (2012) 1169-1175.
20. H. Topsøe, Developments in operando studies and in situ characterization of heterogeneous catalysts, J. Catal., 216 (2003) 155-164.
21. G.A. Somorjai, J.Y. Park, Concepts, instruments, and model systems that enabled the rapid evolution of surface science, Surf. Sci., 603 (2009) 1293-1300.
22. J. Dou, Z. Sun, A.A. Opalade, N. Wang, W. Fu, F.F. Tao, Operando chemistry of catalyst surfaces during catalysis, Chem. Soc. Rev., 46 (2017) 2001-2027.
23. Y. Iwasawa, in Y. Iwasawa, K. Asakura, M. Tada (Eds.), XAFS Techniques for Catalysts, Nanomaterials, and Surfaces, Springer, Cham, 2017, p. 3-10.
24. The Japanese XAFS Society, Foundations and Application of XAFS, Kodansha, Tokyo, 2017.
25. H. Uehara, Y. Uemura, T. Ogawa, K. Kono, R. Ueno, Y. Niwa, H. Nitani, H. Abe, S. Takakusagi, M. Nomura, Y. Iwasawa, K. Asakura, In situ back-side illumination fluorescence XAFS (BI-FXAFS) studies on platinum nanoparticles deposited on a HOPG surface as a model fuel cell: a new approach to the Pt-HOPG electrode/electrolyte interface, Phys. Chem. Chem. Phys., 16 (2014) 13748-13754.
26. C. Genovese, M.E. Schuster, E.K. Gibson, D. Gianolio, V. Posligua, R. Grau-Crespo, G. Cibin, P.P. Wells, D. Garai, V. Solokha, Operando spectroscopy study of the carbon dioxide electro-reduction by iron species on nitrogen-doped carbon, Nat. Commun., 9 (2018) 935.
27. U. Kashaboina, Y. Nishikawa, Y. Wakisaka, N. Sirisit, S.-I. Nagamatsu, D. Bao, H. Ariga-Miwa, S. Takakusagi, Y. Inami, F. Kuriyama, A.L. Dipu, H. Ogihara, S. Iguchi, I. Yamanaka, T. Wada, K. Asakura, Metamorphosis-like Transformation during Activation of In/SiO2 Catalyst for Non-oxidative Coupling of Methane: In Situ X-ray Absorption Fine Structure Analysis, Chem. Lett., 48 (2019) 1145-1147.
28. A. Bergmann, B. Roldan Cuenya, Operando Insights into Nanoparticle Transformations during Catalysis, Acs Catal., 9 (2019) 10020-10043.
29. K.I. Kimijima, T. Watanabe, Y. Takeichi, Y. Niwa, M. Kimura, Development of in situ cell for simultaneous XAFS/XRD measurements at high temperatures, Radiat. Phys. Chem.,175 (2020) 108153.
30. D. Wakabayashi, N. Funamori, T. Kikegawa, K. Watanabe, S. Kohara, H. Nitani, Y. Niwa, Y. Takeichi, H. Abe, M. Kimura, Nature of the transformation in liquid iodine at 4 GPa, Phys. Rev. B, 96 (2017) 024105.
31. T. Yamamoto, Advances in X-ray chemical analysis, 38 (2007) 45-65.

32. S. Yamazoe, Y. Hitomi, T. Shishido, T. Tanaka, XAFS study of tungsten L1-and L3-edges: Structural analysis of WO3 species loaded on TiO2 as a catalyst for photo-oxidation of NH3, J. Phys. Chem. C, 112 (2008) 6869-6879.
33. D.E. Sayers, E.A. Stern, F.W. Lytle, New Technique for Investigating Noncrystalline Structures: Fourier Analysis of the Extended X-Ray---Absorption Fine Structure, Phys. Rev. Lett., 27 (1971) 1204-1207.
34. E. A. Stern, in D. C. Koningsberger, R. Prins, (Eds.) X-ray absorption : principles, applications, techniques of EXAFS, SEXAFS, and XANES, Wiley, New York, 1988, p. 3-51.
35. M. Newville, Fundamentals of XAFS, University of Chicago, Chicago, 2004.
36. A.L. Ankudinov, C.E. Bouldin, J.J. Rehr, J. Sims, H. Hung, Parallel calculation of electron multiple scattering using Lanczos algorithms, Phys. Rev. B, 65 (2002) 104107.
37. 忠. 石井, EXAFSの基礎 : 広域X線吸収微細構造, 裳華房, 東京, 1994.
38. J.J. Rehr, R.C. Albers, Theoretical approaches to x-ray absorption fine structure, Reviews of Modern Physics, 72 (2000) 621-654.
39. G. Bunker, Application of the ratio method of EXAFS analysis to disordered systems, Nuclear Instruments and Methods in Physics Research, 207 (1983) 437-444.
40. R. Frahm, Quick scanning exafs: First experiments, Nucl. Instrum. Methods A, Detectors and Associated Equipment, 270 (1988) 578-581.
41. T. Nonaka, K. Dohmae, T. Araki, Y. Hayashi, Y. Hirose, T. Uruga, H. Yamazaki, T. Mochizuki, H. Tanida, S. Goto, Quick-scanning x-ray absorption spectroscopy system with a servo-motor-driven channel-cut monochromator with a temporal resolution of 10 ms, Rev. Sci. Instrum., 83 (2012) 083112.
42. O. Sekizawa, T. Uruga, M. Tada, K. Nitta, K. Kato, H. Tanida, K. Takeshita, S. Takahashi, M. Sano, H. Aoyagi, A. Watanabe, N. Nariyama, H. Ohashi, H. Yumoto, T. Koyama, Y. Senba, T. Takeuchi, Y. Furukawa, T. Ohata, T. Matsushita, Y. Ishizawa, T. Kudo, H. Kimura, H. Yamazaki, T. Tanaka, T. Bizen, T. Seike, S. Goto, H. Ohno, M. Takata, H. Kitamura, T. Ishikawa, T. Yokoyama, Y. Iwasawa, New XAFS beamline for structural and electronic dynamics of nanoparticle catalysts in fuel cells under operating conditions, J. Phys. Conf. Ser., 430 (2013) 012020.
43. S. Pascarelli, O. Mathon, in Y. Iwasawa, K. Asakura, M. Tada (Eds.), XAFS Techniques for Catalysts, Nanomaterials, and Surfaces, Springer, Cham, 2017, p.109-125.
44. T. Matsushita, R.P. Phizackerley, A Fast X-Ray Absorption Spectrometer for Use

with Synchrotron Radiation, Jpn. J. Appl. Phys., 20 (1981) 2223-2228.
45. R. Torchio, F. Occelli, O. Mathon, A. Sollier, E. Lescoute, L. Videau, T. Vinci, A. Benuzzi-Mounaix, J. Headspith, W. Helsby, S. Bland, D. Eakins, D. Chapman, S. Pascarelli, P. Loubeyre, Probing local and electronic structure in Warm Dense Matter: single pulse synchrotron x-ray absorption spectroscopy on shocked Fe, Scientific Reports, 6 (2016) 26402.
46. B. Ohtani, R.M. Bowman, D.P. Colombo Jr, H. Kominami, H. Noguchi, K. Uosaki, Femtosecond Diffuse Reflectance Spectroscopy of Aqueous Titanium(IV) Oxide Suspension: Correlation of Electron-Hole Recombination Kinetics with Photocatalytic Activity, Chem. Lett., 27 (1998) 579-580.
47. A. Yamakata, T.-a. Ishibashi, H. Onishi, Electron- and Hole-Capture Reactions on Pt/TiO2 Photocatalyst Exposed to Methanol Vapor Studied with Time-Resolved Infrared Absorption Spectroscopy, J. Phys. Chem. B, 106 (2002) 9122-9125.
48. K. Iwata, T. Takaya, H.-o. Hamaguchi, A. Yamakata, T.-a. Ishibashi, H. Onishi, H. Kuroda, Carrier Dynamics in TiO2 and Pt/TiO2 Powders Observed by Femtosecond Time-Resolved Near-Infrared Spectroscopy at a Spectral Region of 0.9−1.5 μm with the Direct Absorption Method, J. Phys. Chem. B, 108 (2004) 20233-20239.
49. L. Chen, X. Zhang, M. Shelby, Recent advances on ultrafast X-ray spectroscopy in the chemical sciences, Chemical Science, 5 (2014) 4136-4152.
50. L. X. Chen, in J. A. van Bpkhoven, C. Lamberti (Eds.), X-Ray Absorption and X-Ray Emission Spectroscopy: Theory and Applications, WILEY, 2016, p. 213-249.
51. T.J. Penfold, C.J. Milne, M. Chergui, Recent advances in ultrafast x-ray absorption spectroscopy of solutions, Adv. Chem. Phys., (2013) 1-41.
52. T.J. Penfold, J. Szlachetko, F.G. Santomauro, A. Britz, W. Gawelda, G. Doumy, A.M. March, S.H. Southworth, J. Rittmann, R. Abela, M. Chergui, C.J. Milne, Revealing hole trapping in zinc oxide nanoparticles by time-resolved X-ray spectroscopy, Nat. Commun., 9 (2018) 478.
53. M. Yabashi, H. Tanaka, T. Ishikawa, Overview of the SACLA facility, J. Synchrotron Rad., 22 (2015) 477-484.
54. Y. Obara, H. Ito, T. Ito, N. Kurahashi, S. Thurmer, H. Tanaka, T. Katayama, T. Togashi, S. Owada, Y. Yamamoto, S. Karashima, J. Nishitani, M. Yabashi, T. Suzuki, K. Misawa, Femtosecond time-resolved X-ray absorption spectroscopy of anatase TiO2 nanoparticles using XFEL, Struct. Dynam., 4 (2017) 044033.
55. T. Katayama, T. Northey, W. Gawelda, C.J. Milne, G. Vankó, F.A. Lima, R. Bohinc,

Z. Németh, S. Nozawa, T. Sato, D. Khakhulin, J. Szlachetko, T. Togashi, S. Owada, S.-i. Adachi, C. Bressler, M. Yabashi, T.J. Penfold, Tracking multiple components of a nuclear wavepacket in photoexcited Cu(I)-phenanthroline complex using ultrafast X-ray spectroscopy, Nat. Commun., 10 (2019) 3606.

56. T. Katayama, S. Nozawa, Y. Umena, S. Lee, T. Togashi, S. Owada, M. Yabashi, A versatile experimental system for tracking ultrafast chemical reactions with X-ray free-electron lasers, Struct. Dynam., 6 (2019) 054302.
57. K.K. Bando, T. Wada, T. Miyamoto, K. Miyazaki, S. Takakusagi, Y. Koike, Y. Inada, M. Nomura, A. Yamaguchi, T. Gott, S. Ted Oyama, K. Asakura, Combined in situ QXAFS and FTIR analysis of a Ni phosphide catalyst under hydrodesulfurization conditions, J. Catal., 286 (2012) 165-171.
58. N. Ishiguro, M. Tada, Structural Kinetics of Cathode Events on Polymer Electrolyte Fuel Cell Catalysts Studied by Operando Time-Resolved XAFS, Catal. Lett., 148 (2018) 1597-1609.
59. T. Uruga, M. Tada, O. Sekizawa, Y. Takagi, T. Yokoyama, Y. Iwasawa, SPring-8 BL36XU: Synchrotron Radiation X-Ray-Based Multi-Analytical Beamline for Polymer Electrolyte Fuel Cells under Operating Conditions, Chem. Rec., 19 (2019) 1444-1456.
60. K. Asakura, in Y. Iwasawa, (Eds.) X-ray absorption fine structure for catalysts and surfaces. Editor, World Scientific, Singapore, 1996, vol. 2, p 34-58.
61. B.K. Teo, M.R. Antonio, B.A. Averill, Molybdenum K-edge extended x-ray absorption fine structure studies of synthetic molybdenum-iron-sulfur clusters containing the MoS4 unit: development of a fine adjustment technique based on models, J. Am. Chem. Soc., 105 (1983) 3751-3762.
62. T. Taguchi, T. Ozawa, H. Yashiro, REX2000 Yet Another XAFS Analysis Package, Phys. Scripta., T115 (2005) 205.
63. T. Taguchi, REX2000 Version 2.5: Improved DATA Handling and Enhanced User-Interface, in, AIP, 2007, pp. 162-164.
64. B. Ravel, M. Newville, ATHENA,ARTEMIS,HEPHAESTUS: data analysis for X-ray absorption spectroscopy using IFEFFIT, J. Synchrotron Rad., 12 (2005) 537-541.
65. E.A. Stern, Number of relevant independent points in x-ray-absorption fine-structure spectra, Phys. Rev. B, 48 (1993) 9825.
66. B.K. Teo, M.R. Antonio, B.A. Averill, Molybdenum K-edge extended x-ray absorption fine structure studies of synthetic molybdenum-iron-sulfur clusters containing the MoS4 unit: development of a fine adjustment technique based on

models, J. Am. Chem. Soc., 105 (1983) 3751-3762.
67. H. Maeda, Accurate Bond Length Determination by EXAFS Method, J. Phys. Soc. Jpn, 56 (1987) 2777-2787.
68. S.J. Gurman, Interpretation of EXAFS Data, J. Synchrotron Rad., 2 (1995) 56-63.
69. A. Michalowicz, G. Vlaic, Multiple solutions in data fitting: a trap in EXAFS structural analysis and some ideas to avoid it, J. Synchrotron Rad., 5 (1998) 1317-1320.
70. Y. Kikutani, Structures of molybdenum silica catalysts reduced by ethanol, and their relations to catalytic oxidation reactions: I. Structure changes of Mo/SiO2 with gradual reduction by ethanol, J. Mol. Catal. A: Chem., 142 (1999) 247-263.
71. Y. Iwasawa, K. Asakura, H. Ishii, H. Kuroda, DYNAMIC BEHAVIOR OF ACTIVE-SITES OF A SIO2-ATTACHED MO(VI)-DIMER CATALYST DURING ETHANOL OXIDATION OBSERVED BY MEANS OF EXAFS, Zeitschrift Fur Physikalische Chemie Neue Folge, 144 (1985) 105-115.
72. E.A. Stern, D.E. Sayers, F.W. Lytle, Extended x-ray-absorption fine-structure technique. III. Determination of physical parameters, Phys. Rev. B, 11 (1975) 4836-4846.
73. J.M. Tranquada, R. Ingalls, Extended x-ray---absorption fine-structure study of anharmonicity in CuBr, Phys. Rev. B, 28 (1983) 3520-3528.
74. G. Bunker, Application of the ratio method of EXAFS analysis to disordered systems, Nuclear Instruments and Methods in Physics Research, 207 (1983) 437-444.
75. H. Kuroda, T. Yokoyama, K. Asakura, Y. Iwasawa, Temperature dependence of EXAFS spectra of supported small metal particles, Faraday Discussions, 92 (1991) 189-198.
76. J.C. Becsey, L. Berke, J.R. Callan, Nonlinear least squares methods: A direct grid search approach, J. Chem. Educ., 45 (1968) 728.
77. M.J. Schalken, C.T. Chantler, Propagation of uncertainty in experiment: structures of Ni (II) coordination complexes, J. Synchrotron Rad., 25 (2018) 920-934.
78. L. Pusztai, R. L. McGreevy, Reverse Monte Carlo Simulation: A New Technique for the Determination of Disordered Structures, Molecular Simulation, 1 (1988) 359-367.
79. S.J. Gurman, R.L. McGreevy, Reverse Monte Carlo simulation for the analysis of EXAFS data, J. Phys. Condens. Matter, 2 (1990) 9463-9473.
80. R.L. McGreevy, Reverse Monte Carlo modelling, J. Phys. Condens. Matter, 13 (2001) R877-R913.

81. J. Timoshenko, A. Kuzmin, J. Purans, Reverse Monte Carlo modeling of thermal disorder in crystalline materials from EXAFS spectra, Computer Physics Communications, 183 (2012) 1237-1245.
82. A. Kompch, A. Sahu, C. Notthoff, F. Ott, D.J. Norris, M. Winterer, Localization of Ag Dopant Atoms in CdSe Nanocrystals by Reverse Monte Carlo Analysis of EXAFS Spectra, J. Phys. Chem. C, 119 (2015) 18762-18772.
83. A.D. Cicco, F. Iesari, A. Trapananti, P. D'Angelo, A. Filipponi, Structure and atomic correlations in molecular systems probed by XAS reverse Monte Carlo refinement, J. Chem. Phys., 148 (2018) 094307.
84. M. Harada, R. Ikegami, L.S.R. Kumara, S. Kohara, O. Sakata, Reverse Monte Carlo modeling for local structures of noble metal nanoparticles using high-energy XRD and EXAFS, RSC Advances, 9 (2019) 29511-29521.
85. A. Anspoks, C. Marini, T. Miyanaga, B. Joseph, A. Kuzmin, J. Purans, J. Timoshenko, A. Bussmann-Holder, Local structure of A-atom in ABO3 perovskites studies by RMC-EXAFS, Radiat. Phys. Chem., 175 (2020) 108072.
86. A. Di Cicco, X-ray Absorption Spectroscopy investigations of disordered matter, Radiat. Phys. Chem., 175 (2020) 108077.
87. K. Fujikawa, H. Ariga, S. Takakusagi, H. Uehara, T. Ohba, K. Asakura, Micro Reverse Monte Carlo Approach to EXAFS Analysis, e-J. Surf. Sci. Nanotech., 12 (2014) 322-329.
88. W.C. Hamilton, Significance tests on the crystallographic R factor, Acta Crystallographica, 18 (1965) 502-510.
89. E. Crozier, A. Seary, Asymmetric effects in the extended X-ray absorption fine structure analysis of solid and liquid zinc, Canadian Journal of Physics, 58 (1980) 1388-1399.
90. T. Yokoyama, Path-integral effective-potential theory for EXAFS cumulants compared with the second-order perturbation, J. Synchrotron Rad., 6 (1999) 323-325.

Chapter 2. Conventional experimental and analytical method

2.1. Introduction

Methodology of XAFS measurement has been well established in these last few decades.[1-3] Synchrotron radiation is widely used as the X-ray source. Synchrotron radiation gives high intensity X-ray and contributes to the development of XAFS measurement. In this chapter, the general part in method of XAFS measurement is introduced. Thus, the methods of conventional XAFS measurement, or the overview of transmission mode and fluorescence mode measurement, are introduced. Methodology of XAFS data processing has also been established.[1,2,4-33] Background removal and normalization are carried out to extract EXAFS oscillation from observed data. EXAFS oscillation is Fourier transformed then analyzed. In addition, inverse Fourier transform is carried out in some cases. In the latter half of section, general procedure of data processing is introduced. In addition, the environment and packages for analysis or program in this thesis are introduced because I carried out new analytical method using home-made program. The details of the setup for measurement are described in each chapter.

2.2. Conventional XAFS measurement

General XAFS measurement is carried out in transmission mode. The arrangement of transmission mode is as shown in Figure 2-1(a), in case of the X-ray source is synchrotron radiation. A particular energy of X-ray is selected by monochromator. The X-ray comes from synchrotron radiation is white X-ray or consists of wide range of energy so that the aimed X-ray energy is need to extract. The monochromator is composed by single crystal and can diffract the certain energy of X-ray. X-ray is focused by mirror. There is no lens to focus the X-ray and the mirror using single crystal is generally applied. Incident X-ray goes through the ion chamber which is arranged before the sample to measure the intensity, I_0. Then, X-ray goes through or absorbed at the sample. Finally, the intensity I of transmitted X-ray is measured ion chamber. As mentioned chapter 1, absorption coefficient μ is described using absorbed distance t by the Beer-Lambert Law as following.

$$I = I_0 \mathrm{e}^{-\mu t} \tag{2-1}$$

The fluorescence mode is applied technique from transmission mode. The arrangement of fluorescence mode is as shown in Figure 2-1(b). The X-ray is transferred, monochromatized and focused by the same method as transmission mode from synchrotron radiation. Incident X-ray also goes through the ion chamber which is arranged before the sample to measure the intensity, I_0. Then, X-ray goes through or absorbed at the sample. Finally, intensity of fluorescence X-ray which comes from sample is measured as I_f. The absorption coefficient is approximated to

$$\mu t = \frac{I_f}{I_0} \ . \tag{2-2}$$

This approximation can be applied when the sample is diluted one such as nanoparticles on the substrate. Therefore, if the sample has enough concentration to measure the transmission mode, fluorescence mode shouldn't be applied. The intensity of fluorescence X-ray is detected by the scintillation counter or the semiconductor detector such as Solid State Detector (SSD) and Silicon Drift Detector (SDD). When the signals are weak and the back ground signals are high, the filter and solar slit to cut the low energy X-ray and scattered X-ray. In case of semiconductor detector, scattered X-rays can be cut by itself using ROI. X-ray which comes from synchrotron radiation is polarized. It means the inelastic scattered X-ray is suppressed at perpendicular position to the incident X-ray. Thus the position of detector is often placed perpendicular to the direction of incident X-ray.

2.3. Equipments

Here, the conventional equipment for XAFS measurement is introduced. Recently, synchrotron radiation is mostly used as the X-ray source. The X-ray is focused by mirror and a particular energy is selected by monochromator. An example of arrangement is shown in Figure 2-2.

2.3.1. Synchrotron radiation source

When the electron is accelerated by electromagnetic field, electromagnetic wave is generated. In case of synchrotron radiation, electrons are accelerated to near the velocity of light. This high energy electron is stored in the electron storage ring and X-ray is generated when the electron is bended by bending magnet. In the storage ring, insertion device is also applied to the straight part. In the undulator, for example,

electrons wiggle in sinusoidal manner by the periodic magnetic field. Thus the X-rays are generated with the same direction of electron in the ring. The X-rays interfere each other. As the result, short width of energy and high flux X-ray is generated. The important features of synchrotron radiation are as following.

- The pulsed X-ray is obtained.
- Brightness of X-ray is very high comparing with X-ray tube.
- High energy X-ray can be available.
- Polarized X-ray is obtained.

Representative synchrotron radiation source in Japan are Photon Factory (High Energy Accelerator Research Organization, Tsukuba) and SPring-8 (Harima).

2.3.2. X-ray optics

The X-ray has to be transported from the electron storage ring to the experimental station. During the transportation, X-ray is monochromatized and focused. The optics for X-ray is introduced here.

2.3.2.1. Monochromator

The X-ray which generated by synchrotron radiation is white X-ray which has wide distribution of energy. In conventional XAFS measurement, energy of incident X-ray has to be monochromatized. The selected energy X-ray is obtained by the X-ray diffraction by single crystal. According to the Bragg's low, the inclination angle θ_B is decided by

$$2d\sin\theta_B = n\lambda \ . \tag{2-3}$$

Here, d (Å) is the lattice spacing, λ(Å) is the wave length of X-ray. The wave length is written as following using Planck constant h, velocity of light c, and energy of X-ray E (eV).

$$\lambda = \frac{hc}{E} = \frac{12398.52}{E} \tag{2-4}$$

Finally, from Equation (2-3) and (2-4),

$$2d\sin\theta_B = \frac{12398.52}{E}$$

(2-5)

Silicon single crystal is often applied to the monochromator. In case of Si(111) and Si(311), the lattice spacing are d=3.1356 Å and d=1.6375 Å, respectively. The energy resolution is related with the characteristics of monochromator. Si(111) has enough energy resolution for usual measurement. If higher energy resolution is needed, higher order reflection such as Si(220) or Si(311) are applied. Though the energy resolution is improved by such monochromators, intensity of incident X-ray becomes low. In practical, double crystal monochromator which uses the two monochromators in parallel arrangement is widely applied. The advantages of double crystal monochromator are as following.

- The position of monochromatized X-ray becomes stable.
- The higher harmonic wave can be removed to detune the parallelism of crystals.

2.3.2.2. Mirror

The reflectance factor of X-ray is less than 1. X-ray is focused using mirror not the lens. The critical angle of total reflection is given by

$$\theta_C = \left(\frac{r_0 N_A Z \rho}{\pi A}\right)^{\frac{1}{2}} \lambda \ .$$

(2-6)

Here, r_0 is the radius of an electron, N_A is the Avogadro's constant, Z is the number of element of material on mirror, ρ is the density of material, and A is the molar mass. The critical angle is mrad order. As the result of total reflection on the mirror, high energy X-ray which cannot satisfy Equation (2-6) is removed. Thus the mirror also can remove the higher harmonic wave of X-ray.

2.3.3. Detectors

2.3.3.1. Ionization chamber

Ionization chamber is widely used to detect the intensity of incident X-ray, I_0. In the transmission mode measurement, intensity of transmitted X-ray, I, is also detected by ionization chamber. The principle of ionization chamber is as following. When an

X-rays goes through the ionization chamber, gases with which fill the ionization chamber are ionized. There is a strong electronic field in the ionization chamber between the electrodes by high voltage so that ionized gases and electrons are captured by the electrodes each other. Thus the X-rays are counted as the current at electrodes. The current is amplified by amplifier and outputted as voltage, then converted to pulses by Voltage-to-Frequency (V/F) converter, finally counted by counter. The component of gases is selected depending on the energy of X-ray. The detection efficiency should be adjusted 10-25% for I_0 detection and slightly lower than 100% for I detection, respectively. The feature of ionization chamber is its linearity. If high voltage is not enough, this linearity is lost. Thus the high voltage is important for ionization chamber. The noises of signal can be caused by leakage of current and transport line to the counter. The surface of insulator in the ionization chamber has to be kept clean to suppress the leakage of current. The transport line has to be designed short and grounded well to suppress the noise during the signal transportation.

2.3.3.2. Scintillation counter

Scintillation counter is used to detect the intensity of fluorescence X-ray, I_f, in the fluorescence mode measurement. Scintillator emits the sparks or scintillations when the ionizing radiation goes through the scintillator. These scintillations are very weak intensity. Thus the scintillations are amplified by the photomultiplier or the phototube and counted as pulses. The photomultiplier is the tube which is equipped the photocathode at inlet and dynodes inside under vacuumed condition. An electron is emitted when the scintillation hit the photocathode. This electron is goes to dynode by the electric field and hit the dynodes. When an electron hits the dynode, secondary electrons are emitted. These secondary electrons hit the dynode one by one and the electrons are increased, finally. Scintillation counter doesn’t have the energy resolution. It means that scintillation counter cannot remove the background from scattered X-ray in itself. Thus filter and solar slit is equipped between the sample and the scintillation counter. Filter is low energy X-ray pass filter. The X-ray which has higher energy than aimed fluorescence X-ray such as inelastic scattering X-ray is absorbed at filter. However, filter also emits the fluorescence X-ray. Thus solar slit is equipped between filter and detector. Solar slit cut only the fluorescence X-ray and scattered X-ray from the filter. Finally, background of signal is reduced.

2.4. Data processing

Generally, experimental data is treated as shown in Figure 2-3 before the analytical method is carried out.[5] Decide the absorption edge (E_0) from the spectrum and convert loaded data from energy (E) to wavenumber (k) using Equation (2-7).

$$k = \sqrt{\frac{2m}{\hbar^2}(E - E_0)} \tag{2-7}$$

At the same time, normalize the spectrum to consider the effect of only one X-ray absorbing atom. And remove the background to extract EXAFS oscillation $\chi(k)$ from the spectrum. Multiplying k^n (n=0, 1, 2, or 3) weight by $\chi(k)$ to consider the damping of EXAFS oscillation in the high wavenumber region. $k^n \cdot \chi(k)$ is Fourier transformed. This Fourier transformed spectrum looks like a radial distribution function. However, it includes phase shift so that different from real radial distribution function of sample. This phase shift is calculated theoretically or referred to the reference sample during analysis and then real parameters are searched. General curve fitting (CF) analysis is performed to Fourier transformed $k^n \cdot \chi(k)$ or inversly Fourier transformed one with selecting peak of EXAFS oscillation. The detail of each process is as following.

2.4.1. Background removal and Normalization

Background removal was performed using REX2000 (RIGAKU).[62,63] In REX2000, inflection point of second derivative is defined as absorption edge, E_0. Decide the pre-edge region (μ_{pre}) and post-edge region (μ_{post}) like Figure 2-4 for normalizing the spectrum. Spectrum was normalized and background was removed as following,

$$\chi(k) = \frac{\mu - \mu_s}{\mu_0} = \frac{(\mu - \mu_{pre}) - \mu_{post}}{\mu_0}$$
$$\mu_s = \mu_{pre} + \mu_{post} \tag{2-8}$$

Background of pre-edge region is calculated least-square approximation using Victoreen equation.

$$\mu_{pre}(\lambda) = A + C\lambda^3 - D\lambda^4 \tag{2-9}$$

Here, *A*, *C*, and *D* are constant. This equation includes the correction term. When the measurement is carried out using synchrotron radiation, the detectors for incident X-ray and transmitted one so that Equation (2-9) includes constant *A* as a correction term. This background is extrapolated to higher energy than absorption edge.

On the other hand, the center of oscillation is estimated using cubic spline smoothing method in the post-edge region. When sum of absolute value in differential coefficient of second derivative for μ_0 and EXAFS oscillation are described as *B"* and *D"*, respectively, μ_0 is searched to satisfy following equation.

$$B'' < 0.002D'' \tag{2-10}$$

This equation means spline function is almost linear function. However, this equation sometimes cannot estimate μ_0 because of noise effect to D''. Therefore Cook-Sayers evaluation is used.[10] They introduce three parameters from the Fourier transformation of experimental data as following,

H_R : the average value of transform magnitude between 0 and 0.25 Å

H_M : the maximum value in the transform magnitude between 1 and 5 Å

H_N : the average value of transform magnitude between 9 and 10 Å

and the termination conditions are

$$H_R - H_N \geq 0.05H_M$$
$$\text{or if } H_N > 0.1H_M \text{ then } H_R \geq 0.1H_M \tag{2-11}$$

The condition of $H_N > 0.1H_M$ indicates that the experimental data has much noise. These indicators are useful to check the background removal was appropriate or not. The spline smoothing can follow the experimental data well depending on the parameters. Most important point is not only to use these indicators but check one by one visually.

The spectrum which its background was removed is normalized by edge jump μ_0. This normalization is important to consider the EXAFS oscillation for the one X-ray absorbing atom. To consider only one atom's EXAFS oscillation, EXAFS spectrum can be analyzed.

2.4.2. Fourier transformation

After background removal, k^n weight is multiplied to $\chi(k)$. This treatment considers the damping effect in high wavenumber region caused by Debye Waller factor and so on.[11] This treatment makes peak separation clearly and emphasizes the heavy elements' signals. However, noise is also emphasized so that it is important to check the spectrum visually.

The peaks that related with bond lengths between X-ray absorbing atom and neighbor atoms are observed from Fourier transform of $\chi(k)$. Experimental EXAFS data is finite so that finite Fourier transformation as following is used.

$$\mathrm{FT} = \int_{k_{min}}^{k_{max}} k^n \cdot \chi(k) w(k) \mathrm{e}^{2ikr} dk \tag{2-12}$$

The minimum domain, k_{min}, is selected between 2.0-3.0 Å^{-1} to avoid the effect of multiple scattering around absorption edge. The maximum domain, k_{max}, should be selected as large as possible. However, k becomes higher the noise also becomes higher because the intensity of oscillation becomes smaller in high k region. k_{max} have to be selected with considering the S/N ratio in experimental spectrum.

Window function is used for finite Fourier transform to avoid the effect of truncation though the some peaks can become broad. In this thesis, Hunning function defined as following equation is used for all spectra.

$$\begin{aligned} \mathrm{w} &= \left[1 - \frac{\cos\{\pi(k - k_{min})\}}{2d}\right] && k_{min} < k < k_{min} + d \\ &= 1 && k_{min} + d < k < k_{max} - d \\ &= \left[1 - \frac{\cos\{\pi(k_{max} - k)\}}{2d}\right], && k_{max} - d < k < k_{max} \end{aligned} \tag{2-13}$$

where d is recommended about 5-10 % of Fourier transformation range. I choose 10 % of the range in this thesis. Note that though the Fourier transformed spectrum almost looks like a radial distribution function of the sample, this is not as mentioned. REX2000 was used to calculate the Fourier and inversely Fourier transformed data for CF analysis using REX2000. On the other hand, Larch package was used to calculate such transformation for CF analysis and constrained thorough search (CTS) analysis using the self-written codes.[12] Note that the definition of the window function is

different between REX2000 and Larch. Therefore, the scripts using Larch has correction part for parameters to the definition of REX2000.

In many analyses, the inversely Fourier transformed spectra are used to select the particular r range and transformed to k space. This can be filtering out the EXAFS signal of aimed peak and then represent as $\chi(k)$. It is helpful and carried out from early analyses. Though this approach is effective for simple system such as the foil sample, it becomes complicated for complex system. It is because the effect from another shell can be combined even though the r region is limited. The careful treatment is needed for complex system.

2.5. Environment for analysis

In this thesis, background removal and CF analysis were carried out using REX2000. CF analysis was also carried out using the hand-made program. Thorough search analysis was carried out using the hand-made program. For CF and TS analysis, backscattering amplitude and phase shift are calculated using FEFF code.[13,14] The scripts of hand-made program were written in “Python 3.7.3”. and operation system (OS) of computers were “Windows 10 pro”. The details of the environment for analysis are shown in Table 2-1. The packages of Python which were used mainly in this thesis were Anaconda 3 [15] and Larch package[12]. Python gives many useful packages. The packages which were mainly used in this thesis are shown in Table 2-2.

2.5.1. FEFF code

The backscattering amplitude and phase shift are calculated using FEFF code. FEFF code was developed by J. J. Rehr, et al.[13,14] In FEFF code, the ab initio multiple scattering calculations of XAFS are carried out and yields scattering amplitude and phases for each path. In this thesis, FEFF8.2 code was used. FEFF has the many modules corresponding to procedure of calculation. In this thesis, the scattering amplitude and phase shift for each path was calculated and the feff000N.dat (N=1,2, ⋯) files were generated for carrying out CF analysis and CTS analysis using the program which was made by myself. Equation of Motion (EM) method was also carried out to estimate the Debye Waller factor.[16]

Equation of Motion method for Debye Waller factor is proposed by A. V. Poiaarkova, and J. J. Rehr.[16] The Debye Waller factor is estimated from the vibration between X-ray absorbing atom and its neighbor using force constant of its bond in EM method.

Force constant of each bond can be obtained by Raman spectroscopy.

In FEFF code, EM method is controlled by “DEBYE” card. In addition to the input file for FEFF main calculation, “spring.inp” file is also needed to input the force constant of each bond. The result is outputted as “s2_em.dat” file. In FEFF calculation for $\chi(k)$, this Debye Waller factor is used in “ff2chi” process.

2.5.2. Larch

Larch is a package of Python for XAFS calculation developed by M Newville.[12] The functions of general analysis program, Athena and Artemis [17] are included in Larch. In this thesis, “ff2chi” function which calculates $\chi(k)$ using calculated scattering amplitude and phase shift refer to ‘feff000N.dat’ files which were calculated by FEFF code was used. In addition, Fourier transformation and inversely Fourier transformation was carried out using “xftf” and “xftr” function, respectively. Note that the definition of the range of window function is deferent from REX2000. Thus these parameters are adjusted to definition of REX2000 in self-written codes. The details of package and equipped functions are sited on the Web site.[18] In this thesis, Larch 9.43 was used.

Table 2-1. The details of environment for analysis.

Chapter 3	OS	Windows 10 Pro
	Processor	Intel(R) Core(TM) i7-2600 CPU @ 3.40GHz
	Memory	8.00 GB
	Storage	256 GB (SSD: Solid State Drive)
Chapter 4, 5	Processor	Intel(R) Xeon(R) Bronze 3204 CPU @1.90 GHz
	Memory	32.0GB
	Storage	256 GB (SSD: Solid State Drive)
FEFF		8.2
Python		3.7.3

Table 2-2. The Python libraries which used for EXAFS analysis program.

Package name	Purpose
Argparse	Receive the argument when the script starts running at command line.
glob	Search the pathnames which matched to a specific pattern.
xraylarch	Package which includes the function for XAFS analysis. The functions which used in this thesis are shown in Table 2-3.
multiprocessing	Enable to carry out calculation with multi threads at the same time.
natsort	Sort the files for feff calculation.
Numpy	Package which treat array and calculate faster.
os	Give paths to the files easily.
time	Measure the time how long takes for calculation.
yaml	Enable to treat YAML file. YAML file is used as input file in hand-made program.

Table 2-3. The functions which used for analysis program from larch library.

Function name	Description
group	Data (arrays) and parameters (scalars) are preserved in a set as group.
larch_plugins.io	
read_ascii	Read the experimental data as a group.
larch_plugins.feffdat	
feffpath	Read the "feff000N.dat" file and preserve the parameters for the path.
ff2chi	Calculate the EXAFS oscillation $\chi(k)$ using feffpath group.
larch_plugins.xafs	
xftf	Fourier transform the EXAFS oscillation $\chi(k)$.
xftr	Inversely Fourier transform the EXAFS oscillation $\chi(k)$.
feffit	Perform the curve fitting analysis.
larch_plugins.fiting	
param	Define a parameter for path and set some of its attribute
guess	Define a variable parameter for path and set some of its attribute.
larch_plugins.feffit	
feffit_transform	Preserve the parameters for Fourier and inversely Fourier transformation and range of comparison between the data and sum of paths as a Transform group.
feffit_dataset	Preserve the group of experimental data, a list of feff paths, and a Transform group.
feffit_report	Return a printable report from a feffit function.

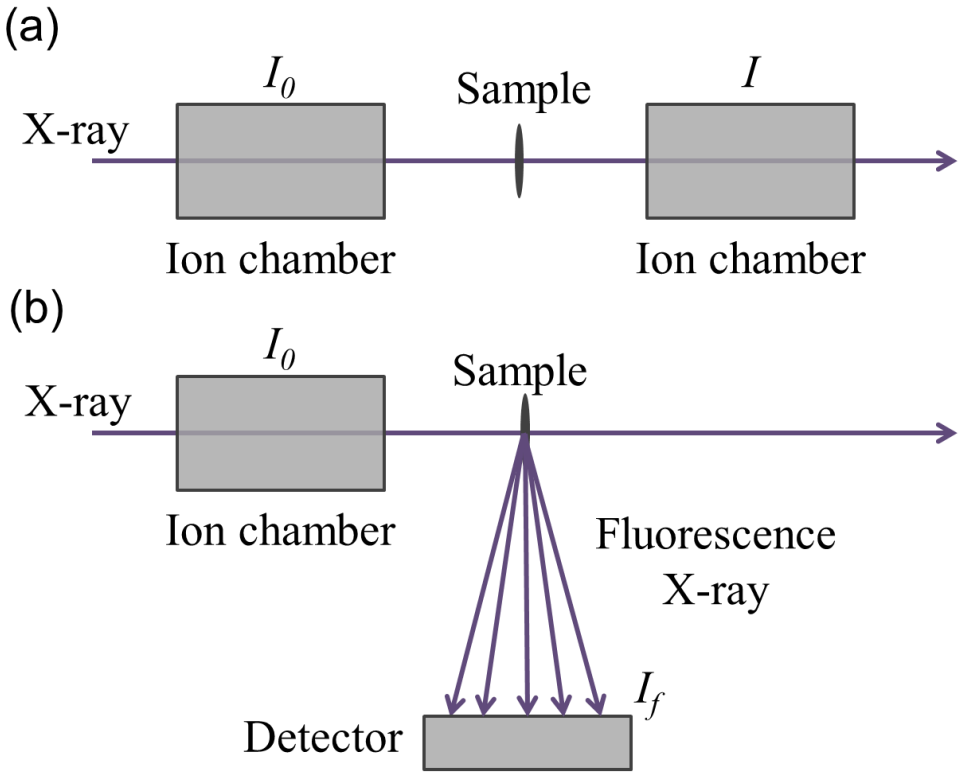

Figure 2-1. Arrangement of conventional XAFS measurement of (a) transmission mode and (b) fluorescence mode.

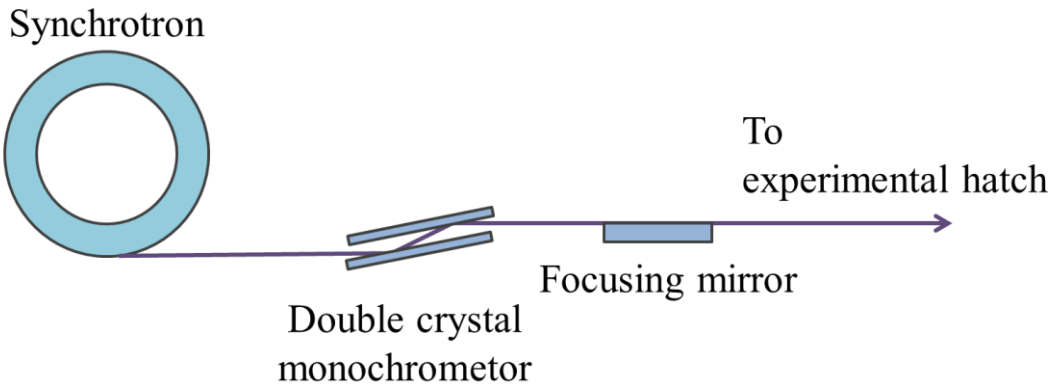

Figure 2-2 Arrangement of beamline.

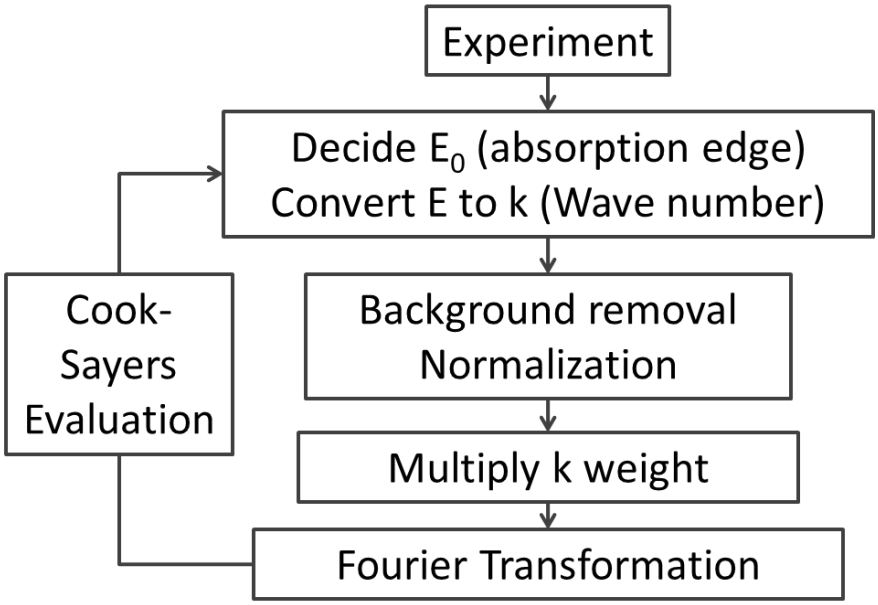

Figure 2-3. Flow diagram for analyzing the experimental EXAFS data using curve fitting method.

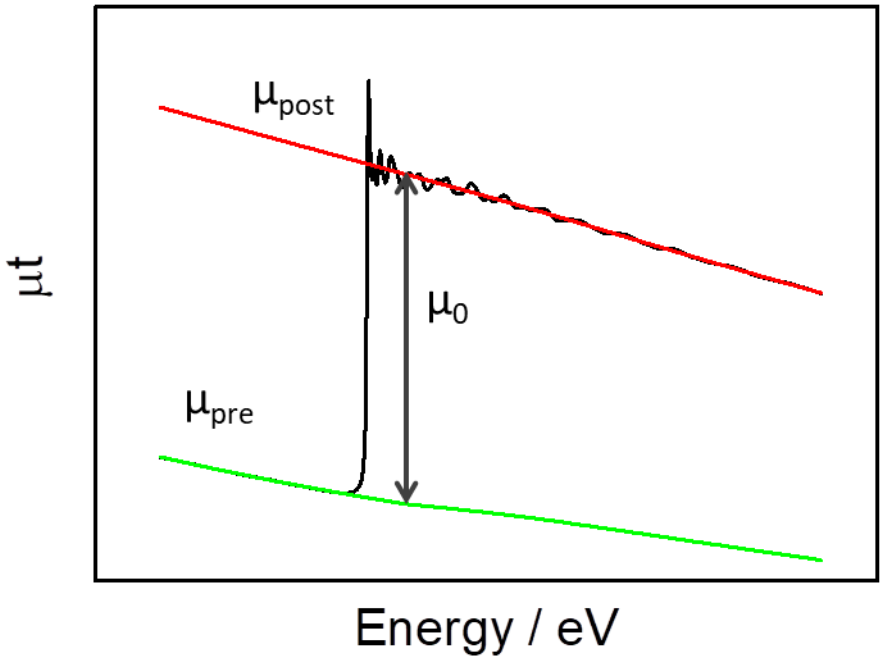

Figure 2-4. EXAFS spectrum and extrapolation or interpolation line for back ground removal. The Green line shows the pre-edge region (μ_{pre}) and the red line shows post-edge region (μ_{post}).

Reference

1. The Japanese XAFS Society, Foundations and Application of XAFS. Kodansha, 2017.
2. M. Newville, Fundamentals of XAFS, Reviews in Mineralogy and Geochemistry, 78 (2014) 33-74.
3. M. Nomura, in Y. Iwasawa, K. Asakura, M. Tada (Eds.), XAFS Techniques for Catalysts, Nanomaterials, and Surfaces, Springer, Cham, 2017. p.67-74.
4. D. E. Sayers, B. A. Bunker, in D. C. Koningsberger, R. Prins (Eds.), X-ray absorption: principles, applications, techniques of EXAFS, SEXAFS, and XANES, Wiley, New York, 1988, p. 211-253.
5. K. Asakura, in Y. Iwasawa (Eds.), X-ray Absorption Fine Structure for Catalysts and Surface, World Scientific, Singapore, 1996, p. 33-58.
6. J. J. Rehr, J. J. Kas, F. D. Vila, M. Newville, in Y. Iwasawa, K. Asakura, M. Tada (Eds.), XAFS Techniques for Catalysts, Nanomaterials, and Surfaces, Springer, Cham, 2017. p.13-52.
7. D.E. Sayers, E.A. Stern, F.W. Lytle, New Technique for Investigating Noncrystalline Structures: Fourier Analysis of the Extended X-Ray---Absorption Fine Structure, Phys. Rev. Lett., 27 (1971) 1204-1207.
8. T. Taguchi, T. Ozawa, H. Yashiro, REX2000 Yet Another XAFS Analysis Package, Phys. Scripta., T115 (2005) 205.
9. T. Taguchi, REX2000 Version 2.5: Improved DATA Handling and Enhanced User-Interface, in, AIP, 2007, pp. 162-164.
10. J.W.C. Jr., D.E. Sayers, Criteria for automatic x-ray absorption fine structure background removal, J. Appl. Phys., 52 (1981) 5024-5031.
11. G. Bunker, E.A. Stern, R.E. Blankenship, W.W. Parson, An x-ray absorption study of the iron site in bacterial photosynthetic reaction centers, Biophys. J., 37 (1982) 539-551.
12. M. Newville, Larch: An Analysis Package for XAFS and Related Spectroscopies, J. Phys. Conf. Ser., 430 (2013) 012007.
13. J.J. Rehr, R.C. Albers, Theoretical approaches to x-ray absorption fine structure, Rev. Mod. Phys., 72 (2000) 621-654.
14. J.J. Rehr, J.J. Kas, M.P. Prange, A.P. Sorini, Y. Takimoto, F. Vila, Ab initio theory and calculations of X-ray spectra, C. R. Physique, 10 (2009) 548-559.
15. Community of Anaconda3(https://www.anaconda.com/distribution/)
16. A.V. Poiarkova, J.J. Rehr, Multiple-scattering x-ray-absorption fine-structure Debye-Waller factor calculations, Phys. Rev. B, 59 (1999) 948-957.

17. B. Ravel, M. Newville, J. Synchrotron Rad., 2005, 12, 537-541.
18. Community of Larch package(http://xraypy.github.io/xraylarch/index.html)

Chapter 3. Development of constrained thorough search analysis for extended X-ray absorption fine structure

3.1. Introduction

Extended X-ray absorption fine structure (EXAFS) spectroscopy refers to the oscillation appearing from 50 to 1000 eV above an X-ray absorption edge. EXAFS is an element-specific spectroscopy and provides information about the local structure around the X-ray absorbing atoms of materials without long-range order such as surfaces, nanomaterials and catalysts [1]. EXAFS spectra are usually analyzed with background removal and Fourier transformation (FT) into *r*-space, followed by non-linear least square curve fitting (CF) analysis to search for the lowest *R*-factor (defined by Equation (3-3) shown below) in *k*- or *r*-space [2]. The CF analysis provides structural parameters such as the coordination number (*N*), correction of the zero kinetic energy (ΔE_0), the bond length (*r*), and the Debye Waller factor (σ^2) for each coordination shell.

When an EXAFS spectrum of a complex system where several shells are present in an inseparably small range is analyzed by the CF method, the following three problems arise.

1. The strong correlation between structural parameters makes the CF analysis unstable and prevents it from converging to give physically meaningful results [3, 4]. Even if the CF results give a reasonably low *R*-factor, it would be hard to exclude the other structural parameters.
2. The fitting results were dependent on the choice of the initial structural parameters.
3. The number of total parameters for CF analysis is limited by the finite degree of freedom determined by the Nyquist theory [5].

$$\frac{2\Delta k \cdot \Delta r}{\pi} + \alpha, \qquad \alpha = 0,1,2 \tag{3-1}$$

Here, Δk is the fitting *k*-range and Δr is the FT *r*-range. Because typical Δk and Δr are 12 $Å^{-1}$ and 1 Å, respectively, the degrees of freedom are eight to ten. Thus, the maximum number of coordination shells is two or three for every 1-Å interval.

The α-molybdenum oxide (α-MoO_3) has a distorted octahedral structure with five different bond lengths, as shown in Figure 3-1 [6]. Chun *et al.* [7] reported the CF analysis of EXAFS data for α-MoO_3 powder. It is still quite difficult to obtain the

bond lengths of MoO_3 correctly by the conventional CF method. In their chapter, they measured polarization dependent and temperature dependent XAFS of α-MoO_3 single crystal and carefully chose the initial parameters. They fixed several parameters using the relationships between the bond length and the Debye Waller factor to decrease the total number of fitting parameters. Finally, they obtained good results. However, the above mentioned careful and particular experiments and analyses were necessary.

To overcome the problems associated with the CF analysis, Fujikawa *et al.* [8] developed the micro reverse Monte Carlo (m-RMC) method and successfully determined the structure of α-MoO_3 without any assumptions of initial structural parameters. The m-RMC is a kind of reverse Monte Carlo approach [9−14]. The reverse Monte Carlo approach tries to find the structure with the random walk of atoms in a large ensemble to seek the low *R*-factor using the Metropolis method. The m-RMC method uses a large number of ensembles of clusters, for which the EXAFS oscillations are calculated and determines the local structure [8].

Here, I propose a new analysis procedure for EXAFS data, which is called constrained thorough search (CTS) analysis. In CTS analysis, EXAFS spectra and their *R*-factors are calculated thoroughly over a certain range of structural parameters. Although CTS analysis is a time-consuming and inefficient method, the appropriate choice of constraints for fitting parameters makes it feasible to determine the local structures of materials, even those with complex structures like α-MoO_3. In this chapter, the CTS analysis is applied to two systems. The first is platinum (Pt) foil as a simple example to illustrate details of CTS analysis. The second is α-MoO_3 as a more complex case. The advantages and disadvantages of the CTS analysis are discussed through comparison with the CF analysis [7] and the m-RMC method [8].

3.2. Experimental

3.2.1. XAFS measurement

A Pt L_3-edge EXAFS spectrum of the Pt foil was measured at the BL-12C beam line of the Photon Factory, Institute of Materials Structure Science, High Energy Accelerator Research Organization (KEK-IMSS-PF) using a Si(111) double-crystal monochromator. The higher harmonics were rejected by a bent cylindrical focusing mirror. The Mo K-edge EXAFS spectrum of the α-MoO_3 powder was accumulated in a transmission mode at the BL-10B beam line of the Photon Factory using a channel cut Si(311) monochromator [7]. Both data can be downloaded from the XAFS database of the Institute for Catalysis, Hokkaido University (https://www.cat.hokudai.ac.jp/catdb/index.

php?action=xafs_login_form&opnid=2), where the data for the Pt foil and α-MoO_3 have been uploaded as JXAFS- 1203210001 and JXAFS-1206270007, respectively.

3.2.2. Data processing

Background removals were carried out using REX2000 [2, 15]. EXAFS oscillations ($\chi(k)$) of the Pt foil and the α-MoO_3 powder were Fourier transformed in the range of 3.0−16.0 and 3.0−13.0 $Å^{-1}$, respectively, with a Hanning window function. The inverse FT data were analyzed by the CF and TS methods, independently. The inverse FT ranges were 2.0−3.0 and 1.0−2.0 Å for the Pt foil and the α-MoO_3 powder, respectively. Only the first neighboring atoms were considered for both cases. The CF analysis was carried out in the REX2000 and Larch programs using the following equation [1, 2, 15, 16],

$$\chi(k) = \sum_{i}^{M} \frac{{S_0}^2 N_i F_i(k)}{k{r_i}^2} \exp(-2r_i/\lambda)\exp(-2{\sigma_i}^2 k^2)\sin\left(2kr_i + \phi_i(k)\right)$$

$$k = \sqrt{\frac{2m}{\hbar^2}\left(h\upsilon - (E_0 + \Delta E_0)\right)}\ ,$$

(3-2)

where ${S_0}^2$, $F_i(k)$, $\phi_i(k)$, λ, m, $h\upsilon$ and E_0 are the inelastic energy loss, backscattering amplitude and phase shift functions, inelastic mean free path, mass of an electron, X-ray energy, and absorption edge energy, respectively. The subscript i indicates the shell number and M is the total number of shells to be analyzed. $F_i(k)$ and $\phi_i(k)$ for the ith shell in Equation (3-2) were calculated using FEFF8.2 program(Table 3-1).[17]

Goodness of fitting was evaluated using the R-factor for all results.

$$R - \text{factor} = \frac{\sum[k^n \cdot \chi_{data}(k) - k^n \cdot \chi_{calculated}(k)]^2}{\sum[k^n \cdot \chi_{data}(k)]^2}$$

(3-3)

Here, $\chi_{data}(k)$ and $\chi_{calculated}(k)$ were the observed EXAFS data and calculated values, respectively. The error for CF analysis was estimated by the Hamilton's method.[18] The degree of freedom was calculated using Equation (3-1) with the α=2.

3.3. Overview of constrained thorough search (CTS) analysis

I considered the structural parameter space in the Thorough search (TS) and CF analyses. This parameter space was a multidimensional metric space consisting of structural parameters such as N, ΔE_0, r, and σ^2, each of which corresponded to one axis in the parameter space. In other words, the dimensionality of the structural parameter space was equal to the number of structural parameters. A set of the structural parameters was represented by a point $\mathcal{P}$ with components of (N, ΔE_0, r, σ^2). The point $\mathcal{P}$ provided the EXAFS oscillation $\chi(k, \mathcal{P})$ and its R-factor. This parameter space had a function mapping from $\mathcal{P}$ onto the R-factor axis expressed as $R=f(\mathcal{P})$, as depicted in Figure 3-2 in two-dimensional (2D) parameter space as an example. In the CF method, the initial point $\mathcal{P}_0$ was provided first and then $\mathcal{P}$ moved in the parameter space to follow the steepest (highest gradient) direction to search for the point $\mathcal{P}'$ with the lowest R-factor as shown in Figure 3-2(a). The curve fitting routine in the Larch program and the REX2000 were equipped with the Levenberg-Marquardt algorithm to find $\mathcal{P}'$ effectively and efficiently [19]. The CF method might reach local minima such as $\mathcal{P}''$ and $\mathcal{P}'''$ shown in Figure 3-2(a) instead of the global minimum $\mathcal{P}'$. As the number of structural parameters increased, the shape of function f became broader with several dips that might trap point $\mathcal{P}$ at a local minimum. In this case, even though the CF analysis gave the converged value, it did not necessarily guarantee the obtained result was the unique and accurate solution.

In contrast, in TS analysis, all points $\mathcal{P}$ were thoroughly surveyed to produce the whole R-factor map, as shown in Figure 3-2(b). In other words, the overall picture of function f was obtained first. When the R-factor was less than a certain value (as shown by the black line in Figure 3-2(b), all $\mathcal{P}$ are accepted as candidate parameter points. Each candidate parameter point $\mathcal{P}$ was not an isolated point but instead formed an n-dimensional domain with other candidate points $\mathcal{P}$. Histograms of each parameter were obtained, as illustrated in Figure 3-2(b). The average of each parameter in the domain was the representative structural parameter of the domain of interest, as indicated by arrows in Figure 3-2(b). The width of the histogram corresponded to the error or precision of the corresponding structural parameter. In more complex systems, several domains were obtained that include points $\mathcal{P}$ that were below the R-factor threshold. The TS analysis gave all possible structures. The domains with the R-factor less than certain value were then explored more precisely or by other methods. The TS analysis was supposed to involve higher cost (time and machine power) than the CF analysis. However, the real costs were not so high as I

anticipated and the TS analysis provided more information than the CF analysis. In addition, I applied the constrained condition to avoid the calculation of meaningless parameter space. The physically meaningful parameter space can be limited by theoretical assumption. Therefore, the calculation time is also saved using constrained condition and it can be called as constrained thorough search (CTS) method.

3.4. Results

3.4.1. CTS analysis of EXAFS data for Pt foil

The strategy of the CTS analysis is to survey a selected area in the structural parameter space thoroughly and then calculate the EXAFS oscillation and the *R*-factor of each point $\mathcal{P}$. The CTS analysis was carried out using a customized Python program borrowing many functions from the Larch library [16]. Figure 3-3 shows a flow chart of the CTS analysis procedure including data processing. The survey range and step for EXAFS analysis of Pt foil are shown in Table 3-2. A total of 33,201 points $\mathcal{P}$ were calculated. A domain was created that consisted of $\mathcal{P}$ satisfying *R*-factor < 0.0052. The maximum *R*-factor (0.0052) was determined by the criterion that the null hypothesis "calculated spectrum is equivalent to that of the best fit one" could not be rejected at a significance level of 0.05. The domain was composed of eight points $\mathcal{P}$ of the structural parameters. Next, the fine CTS analysis was carried out for the confined survey area, as shown in Table 3-2. In this case, 1,814 points $\mathcal{P}$ satisfied *R*-factor < 0.0052. The average values of the structural parameters in the fine CTS analysis were S_0^2=0.99±0.09, ΔE_0=9.6±1.3eV, r=2.76±0.004Å, and σ^2=0.0052±0.0003 Å^2, respectively. Figure 3-4(a) shows the EXAFS oscillation provided by the average structural parameters together with the observed one. Both oscillations agreed well with an *R*-factor of 0.0018. These parameters determined by the CTS analysis corresponded well with those of the CF results within errors and those obtained from m-RMC results, as shown in Table 3-3[8]. Figure 3-4(b−e) presents histograms of the structural parameters S_0^2, ΔE_0, *r*, and σ^2. In Figure 3-4(b−e), the width of each histograms corresponded to the error assessed from the related Gaussian distribution fit (shown as dashed curves).

3.4.2. CTS analysis of EXAFS data for α-MoO_3

α-MoO_3 has an orthorhombic-type crystal structure with lattice constants *a*=3.96 Å, *b*=13.86 Å, and *c*=3.70 Å.[6] α-MoO_3 has six Mo-O bonds. Crystallographic data revealed the presence of five different bond lengths in α-MoO_3 (1.67, 1.73, 2×1.95, 2.25,

and 2.33 Å), as shown in Figure 3-1. The short bonds of 1.67 and 1.73 Å correspond to M=O double bonds, while the bond with a length of 1.95 Å are M-O single bonds. The question is "Six bond lengths can be determined by EXAFS?". Figure 3-5 shows the FT of the observed α-MoO_3 EXAFS oscillation. Peaks appeared around 1.5 and 3.2 Å. The strong peak at 3.2 Å was assigned to Mo-Mo bonds and not considered in this paper. The peak around 1.5 Å was assigned to Mo-O bonds. This peak was split into two because of the interference of the EXAFS oscillations of several Mo-O bonds with different lengths.

The CTS analysis of α-MoO_3 powder was carried out as follows. It was assumed that α-MoO_3 possessed an octahedral structure so that the surveyed parameter space had dimensionality of 24 (=6×4). The number of parameters was greater than the degrees of freedom. Therefore, it was necessary to decrease the number of survey parameters. Thus, S_0^2 and ΔE_0 were fixed to those of Na_2MoO_4 because these two parameters mainly depended on the bonding pair and valence state. Their transferability from the reference compound was often assumed and confirmed in the literature [7]. When S_0^2 and ΔE_0 were roughly adjusted, those were obtained from the reference compound provide the least *R*-factor as shown in Figure 3-6.

The σ^2 values were calculated from the spring constants derived from Raman spectroscopy [7, 20] using an Equation of Motion (EM) method[21]. Because spring constants are related to bond lengths, the Debye Waller factor can be estimated as a function of bond length. I assumed the linear relation described by Equation (3-4), as shown in Figure 3-7.

$$\sigma^2 = 0.0082r - 0.0124 \tag{3-4}$$

This process decreased the dimensionality from 24 to six. Next, the CTS analysis was carried out in this subspace. The analysis was performed under the condition of $r_1 \le r_2 \le r_3 \le r_4 \le r_5 \le r_6$ to avoid the calculation of duplicated structures. I carried out the CTS analysis in two steps. The first step was a rough CTS analysis with low resolution, which was followed by a fine CTS analysis limited to the candidate parameter domains derived from the rough analysis. The rough CTS analysis was performed with a survey step of 0.05 Å for each $\mathcal{P}$ in the range of 1.60–2.40 Å. Table 3-2 shows detail range of each parameter. The number of surveyed points $\mathcal{P}$ was 7×10^4 (74,614). From these, 40 $\mathcal{P}$ satisfied *R*-factor < 0.10. Figure 3-8 shows the distributions for the Mo-O bond lengths r_i (i=1–6). r_1, r_3, and r_6 were determined

independently of the other bond lengths. r_1 appeared around 1.70 Å as a single sharp peak. r_3 and r_6 also consisted of single peaks around 1.95 and 2.35 Å, respectively. The peak widths of r_3 and r_6 were larger than that of r_1. Thus, r_1 could be determined with less error than r_3 and r_6. This meant that the shortest bond (r_1) was the most influential structural parameter that determined the EXAFS oscillation. When the CF analysis was carried out with one shell, N, ΔE_0, r, and σ^2 as fitting parameters, r=1.68 Å was obtained, as shown in Table 3-4. The shortest bond was a leading factor in determining the EXAFS oscillation for following three reasons. 1) The EXAFS amplitude decreases with r according to $1/r^2$ and the inelastic mean free path term described as $\exp(-2r/\lambda)$ in Equation (3-2). 2) There is a positive correlation between the Debye Waller factor and bond length in Equation (3-4). 3) The rapidly rising part around the shortest bond in a radial distribution function affects the EXAFS oscillation more strongly than the gently decreasing part on the longer side because of the low k-region cut-off effect.[22, 23]

The histograms of r_2, r_4, and r_5 had two split peaks because of the effect of the large correlations between the parameters. Figure 3-9(a) shows the three-dimensional (3D) color mapping for the frequency of the points with an R-factor of less than 0.10. The size and color of each plot indicate the frequency of each point $\mathcal{P}$. Three domains were easily identified. Table 3-5 gives the bond lengths for each structure by averaging over the domains. The first domain was composed of r_2≈1.75 Å, r_4≈1.97 Å, and r_5≈2.30 Å. The second domain appeared around r_2≈1.96 Å, r_4≈2.25 Å, and r_5≈2.30 Å and the third around r_2≈1.70 Å, r_4≈1.95 Å, and r_5≈1.98 Å. In other words, two or three bonds always appeared around 2.00 Å.

Figure 3-9(b) shows the positive correlation between r_2 and r_4. When r_2 was shorter than 1.80 Å, r_4 appeared at 2.00 Å, while when r_2 was around 1.95 Å, r_4 became longer than 2.25 Å. Weak positive correlations were also found between r_2 and r_5 or r_4 and r_5. These domains corresponded to the three candidate structures named Structure 1, Structure 2, and Structure 3. Structure 1 was composed of r_1 and r_2 with a range of 1.60 to 1.75 Å, which corresponded to Mo=O double bonds, while r_3 and r_4 appeared around 1.95 Å, corresponding to Mo-O single bonds. Meanwhile, r_5 and r_6 were located around 2.20–2.40 Å. Similarly, Structure 2 had one Mo=O double bond and two M-O single bonds. Structure 3 had two Mo=O double bonds and three Mo-O single bonds.

Next, the fine CTS analysis was carried out in each domain using smaller survey ranges and finer steps, as shown in Table 3-6. The numbers of accepted $\mathcal{P}$ that

satisfied *R*-factor < 0.10 were 5089, 2013, and 4114 out of about 3.5×10^5, 1.4×10^5, and 2.0×10^5 searching processes, respectively, in domains 1, 2, and 3, respectively. Figure 3-10 shows the histograms of bond lengths obtained from the fine CTS analysis of the three domains. Figure 3-11 displays the 3D frequency plots for r_2, r_4, and r_5. The colors of the dots corresponded to the frequencies. Table 3-7 lists the averaged bond lengths over each domain. The error of each parameter was estimated from the width of each histogram. Figure 3-12 compares the EXAFS oscillations obtained experimentally with the results of the CTS analysis results shown in Table 3-7. The bond lengths of Structure 1 had the structure corresponding to crystallographic data within the error bars, although the differences in the *R*-factors between the three structures were not large enough to claim the superiority of Structure 1 over the other structures based on the *R*-factor.

I then performed the CF analysis with six Mo-O bonds as fitting parameters. As expected, the results strongly depended on the initial structural parameters. When the CF analysis started with all bond lengths at 1.95 Å, it converged to 1.69, 1.98, 1.98, 2.27, 2.27, and 2.32 Å, corresponding to Structure 2. When the CF analysis started with six bond lengths of 1.69 Å, it converged to 1.16, 1.23, 1.34, 1.64, 1.99, and 2.27 Å with an *R*-factor of 0.13. Only when the CF analysis was started with bond lengths of 2×1.70 Å, 2×2.00 Å, and 2×2.20 Å it converged as reported in the literature.[6] Therefore, the appropriate choice of the initial value was crucial to obtain accurate parameters using the CF analysis. For reference, two-shell fitting was carried out and it provided two different bond lengths of 1.71 and 1.98 Å, as shown in Table 3-4.

3.5. Discussion

3.5.1. Features of CTS analysis

I could find the methods similar to the CTS analysis in the paper, which were called as brute force approach [24−28] or grid search method [29]. These methods were adjunctive estimation or the refinement of fitted parameters after curve fitting analyses. I used the CTS analysis from the first without the CF analysis. Namely, I carried out the rough survey in the wide range and the fine survey in the limited range. In my CTS analysis the structural parameters were surveyed thoroughly throughout a certain region in the *n*-dimensional space, as shown in Figure 3-2(b), where the sets of structural parameters were denoted as points $\mathcal{P}$. The dimensions of parameters in the CTS analysis are limited by the degrees of freedom. In the analysis of the Pt foil, each

$\mathcal{P}$ consisted of four parameters (S_0^2, ΔE_0, r, and σ^2). The average values of the structural parameters were reported. These parameters obtained from the CTS analysis corresponded well with those determined from the CF analysis. The number of structural parameters in the CF analysis of the Pt foil was much lower than the degrees of freedom. To evaluate the correlation of the degrees of freedom and reliability of the CTS analysis, the CTS analysis of Pt foil was carried out using the EXAFS data in the limited k-range of 3.0–6.0 $Å^{-1}$ with the four structural parameters, as shown in Table 3-8. There were three degrees of freedom, which was less than the number of fitting parameters (4). The CTS analysis determined the three parameters S_0^2, ΔE_0, and r with large errors, as illustrated in Figure 3-13 and Table 3-9, and I found that the frequency of σ^2 increased with σ^2, as shown in Figure 3-13. The function $R=f(\mathcal{P})$ appeared to be a flat function around the minimum for these parameters. When the survey region was increased to that summarized in Table 3-10, the two parameters N and σ^2 could not be determined by the CTS method, as shown in Figure 3-14. Consequently, I concluded that the number of degree of freedom was also important in the CTS analysis. In other words, I cannot obtain the candidates parameters domain when the number of survey parameters are more than degrees of freedom. The CTS automatically prevents the excess of survey parameters over the degrees of freedom.

In the analysis of α-MoO_3, the values of S_0^2 and ΔE_0 were estimated using those of the reference compound Na_2MoO_4. In addition, the relationship between the Debye Waller factor and the bond length was used to decrease the number of structural parameters to six. I now consider the results if the Debye Waller factor are varied as free parameters. It cannot be evaluated directly based on the six independent bond length models because of the limitation of degree of freedom. However, the three-shell CTS analysis with coordination numbers 2+ 2+ 2 for each shell was carried out with three bond lengths and three Debye Waller factors as survey parameters. As the results, the structure corresponding to the Structure 1 was obtained as shown in Table 3-11 and Figure 3-15. Other coordination number combination of three-shell analysis provided the Structures 2 (1+2+3) and 3 (2+3+1). The survey range was limited to 1.60−2.40 Å, which corresponded to the Mo−O bond lengths usually found in Mo oxide compounds [30]. As a result of parameter estimation, the CTS analysis revealed three possible domains. It is an important feature of the CTS that the domains were visualized in the 3D graph such as Figure 3-9. The structural parameters were surveyed more precisely by limiting the survey ranges for the candidate domains (the fine survey process), as shown in Figure 3-10. In α-MoO_3, it was difficult to conclude which structure was superior to the others only from the

EXAFS results or *R*-factor because these structures could not be distinguished only by the *R*-factor. Therefore, the combination of the CTS analysis results with other experimental evidence or theoretical calculations is necessary. In the theoretical approach, molecular dynamics (MD) and density functional theory (DFT) calculations would be good choices to help select the appropriate candidate [31−42]. But, here, I applied the bond valence theory [43] to the three structure candidates identified by the CTS analysis. The bond valence sums obtained for Structures 1, 2, and 3 were 6.00, 4.48, and 6.62, respectively. Because the Mo valence in α-MoO_3 is 6+, Structure 1 was the most relevant structure. Structure 1 was the same structure as that of the crystallographic data for α-MoO_3. Thus, the CTS analysis can provide the several possible structure candidates with the determined six different bonds.

Next the maximum value of *R*-factor for acceptance/rejection conditions is discussed. The maximum value of the *R*-factor was 0.10 in the case of α-MoO_3. This value corresponded to the Hamilton test criterion with the null hypothesis that "the candidate calculated spectrum is equivalent to that of the best fit one" could not be rejected at a significance level of 0.05.[18] In this study, all the parameter points $\mathcal{P}$ that satisfied the condition *R*-factor < 0.10 were treated equally. If χ^2 -test could be used, where χ^2 is defined as

$$\chi^2 = \frac{N_{dof}}{\left(N_{dof} - N_{tsp}\right)} \frac{1}{N} \sum_k \frac{[\chi_{data}(k) - \chi_{calculated}(k, \boldsymbol{\mathcal{P}})]^2}{[\epsilon(k)]^2} \quad , \tag{3-5}$$

the occurrence probability of each point $\mathcal{P}$ can be decided exactly by the χ^2-distribution. In Equation (3-5), N_{dof}, N_{tsp}, N, $\chi_{data}(k)$, $\chi_{calculated}(k, \mathcal{P})$, and $\epsilon(k)$ are the degrees of freedom, number of CTS analysis parameters, number of data points, observed and calculated EXAFS oscillations, and error, respectively. The calculation of χ^2 requires errors $\epsilon(k)$, but it was difficult to determine the systematic error exactly. Thus, in this study, *R*-factor was used instead of χ^2 value. Although this assumption decreased the precision of the determined structural parameters, it decreased the risk of reporting the wrong values.

Finally, I should discuss the meaning of the histograms. Each histogram is proportional to the occurrence frequency of each structural parameter. Consequently, the average is the most probable value of the structural parameter and the width of the histogram corresponds to the error or reliability of the structural parameter. In the present study, the structural parameters were six bond lengths. The histograms looked

like the radial distribution curve, as shown in Figure 3-8(g). The peak areas were 1.65, 2.15, and 2.25, which corresponded well to the coordination numbers of 1.60, 2.20, and 2.24 determined from the three-shell CF analysis, as shown in Table 3-12. However, the histograms of the CTS analysis are not the same as the radial distribution curve. That is, the histogram of the CTS analysis is just the frequency of the structural parameter and not the real radial distribution curve.

3.5.2. Comparison of CTS analysis with CF and m-RMC analyses

Because α-MoO_3 has already been analyzed by the CF analysis [7] and the m-RMC method [8], the three analysis methods can be compared directly in the case of MoO_3. It is difficult to obtain meaningful results using the CF analysis for materials with complex local structures like α-MoO_3 if the initial structural parameters are not appropriate. As mentioned in Section 3.4.2., when the CF analysis started with all bond lengths at 1.95 Å, it converged to the Structure 2. In addition, when the CF analysis started with the results of rough CTS, each initial structure converges to the structures which correspond to the results of fine CTS as shown in Table 3-13 and Figure 3-16. Only when the CF analysis starts with the correct structural parameters, does it give an answer that corresponds well to the crystallographic data. This means that the results derived from the CF analysis are not necessarily accurate structures even if rather good *R*-factors are obtained in the case of complex structures. If the number of the fitting shells is decreased, the most influential structural parameters are obtained in the CF analysis as shown in Tables 3-4 and Table 3-12. Note that the value is not equal to the average of all Mo−O bonds but the most influential shortest one. In the two-shell fitting, the CF analysis provided values of 1.72 and 2.09 Å with coordination numbers of 1.5 and 2.1, respectively. The result corresponded to two bond lengths, which mostly explained the EXAFS oscillation. Two-shell fitting was carried out in the analysis of Mo oxide catalysts, which thus corresponded to the shells with the largest and second largest contributions [44].

Unlike CF analysis, the CTS and m-RMC methods do not require the exact initial structures, although the CTS analysis requires the number of survey parameters or the dimensionality of the parameter space to be less than the degrees of freedom. What I assumed are the following three items: 1) The Mo oxide in 6+ has mainly distorted octahedral and sometimes tetrahedral. 2) The Mo−O bond lengths are present in the range of 1.6−2.4 Å. 3) The Mo−O bond length and spring constants have relations. The CTS analysis provides several possible candidates structural parameters that reproduce the observed spectra well. This seems to be a disadvantage of the CTS

analysis because the CF analysis gives a unique solution with a low *R*-factor. However, the unique solution of the CF analysis is not always reliable for complex systems. In this chapter, three possible structure candidates were identified by the CTS analysis. This is beneficial to those who are not so familiar with the EXAFS analysis and may consider the obtained CF result as a unique solution. In addition, these candidates are visually shown like Figure 3-9. Of course, such visualization is allowed only when the correlation of parameters is less than 3 because it is impossible to show the six-dimensional graph. Even though there is a limitation in visualization, I can definitively say that there is no other possibility based on the EXAFS data. The final structure can be selected from the candidates by other experimental or theoretical methods. In this study, bond valence analysis of the three candidate structures allowed us to select the correct one consistent with crystallographic data. As mentioned above the histograms of the CTS analysis provides the error of each parameter though the m-RMC method gives the radial distribution of bond lengths as shown in Figure 3-17.

A disadvantage of the CTS analysis compared to the CF analysis is that it requires more costs. Therefore, the CF analysis should be carried out for simple systems. The increased cost of the CTS analysis compared to that of the CF analysis is within a tolerable range. The m-RMC method requires more resources than the CF and CTS analyses because the longer calculation time increases the reliability of the m-RMC approach.

I compare the precision of the three types of analyses. The precision of the CF and CTS analyses are at the same level if the system is simple. In a complex system, the CF analysis may converge to an inaccurate local minimum. Generally, m-RMC analysis gives a worse *R*-factor than those obtained from the CF and CTS analyses because the EXAFS oscillation is calculated based on the ensemble of a large number of model structures, which may happen to include inappropriate model structures [8].

Finally, the advantages and disadvantages of the CTS analysis compared with the CF analysis are summarized. The important advantages are 1) to search the whole parameter space, or independent of the selection of initial parameters, 2) to visualize the distribution of the parameter space and their correlation, 3) to pick up the local minima to confirm that the obtained structure is unique or not in the parameter space, and 4) to automatically consider the limitation of degree of freedom. These advantages overcome the problems of the CF analysis, or parameter correlation and dependence of initial parameter, as mentioned in Section 3.1. On the other hand, disadvantages are 1) to take much time to search the whole parameter space, and 2) to treat huge data.

However, a recent development of computer hardware has lessened these disadvantages and may not be the practical problems. Although the CF analysis is useful for the simple system, the CTS analysis especially shows its large ability for analyzing complex systems on surface and in nanomaterials.

3.5.3. Possibility of the practical application of CTS analysis

The CTS analysis can be effectively applied to nanoparticle structure analysis during reaction processes because the structure change occurs continuously during the reaction so that the survey range can be effectively narrowed. I am now analyzing WO_3 nanoparticle, which has also a complex structure, during the photoexcitation process.[45−47] Some of the parameters can be estimated from the structure in the ground state. Consequently, the excited-state structure can be revealed by the CTS analysis. Alloy nanoparticle system is another application direction of the CTS analysis. Nano-particles of a binary alloy (MM') have two bonds (M−M and M−M') at similar positions. The eight parameters for two different bonds should be optimized for each edge at the same time. The correlation between M−M and M−M' deteriorates the accuracy of the fitting results.[48−56] The CTS analysis will provide possible candidate domains for the MM' alloys. The final application is metal species deposited on the single crystal surfaces where I can study the polarization dependent EXAFS.[57−59] The 3D surface structures of single atom site or nanoparticles can be exactly determined with definite error bars.[60−63]

I anticipate that the CTS analysis will become a standard analysis method for complex systems. The CTS analysis is still under development and I hope that this paper will invoke discussion about the scope of the CTS analysis and spur the EXAFS investigation of complex systems using the CTS analysis.

3.6. Conclusion

In this chapter, I proposed the CTS method for analysis of EXAFS spectral data. The CTS analyses of the Pt L_3-edge EXAFS data for the Pt foil and the Mo K-edge EXAFS data for the α-MoO_3 powder were presented as a simple case and an example of a complex structure, respectively. The CTS analysis provided possible structural candidates that reproduced the experimental data well without the selection of accurate initial parameters. Two step CTS analyses save the time and provide enough precisions in the results. In the case of α-MoO3, three candidate structures were

obtained and visualized in the 3D figure. My results reveal that the CTS analysis is a powerful tool to analyze EXAFS data obtained for complex systems on surfaces and in nanomaterials.

Table 3-1. The result of FEFF calculation, “feff0001.dat”. Since the backscattering amplitude $F_i(k)$ and the phase shift $\phi_i(k)$ were not so strongly dependent on the bond distance, they were calculated by FEFF 8.2 code with Mo-O distance =0.195 nm.[17]

MoO3 Feff 8.20
POT Non-SCF, core-hole, AFOLP (folp(0)= 1.150)
Abs Z=42 Rmt= 1.222 Rnm= 1.422 K shell
Pot 1 Z= 8 Rmt= 1.020 Rnm= 1.187
Gam_ch=5.613E+00 H-L exch
Mu= 3.115E+00 kf=2.024E+00 Vint=-1.249E+01 Rs_int= 1.792
PATH Rmax= 1.969, Keep_limit= 0.00, Heap_limit 0.00 Pwcrit= 2.50%
Path 1 icalc 2

---

2 6.000 1.9500 2.3175 3.11508 nleg, deg, reff, rnrmav(bohr), edge
x y z pot at#
0.0000 0.0000 0.0000 0 42 Mo absorbing atom
0.0000 0.0000 1.9500 1 8 O

k	real[2*phc]	mag[feff]	phase[feff]	red factor	lambda	real[p]@#
0.000	8.8834E+00	8.1927E-05	-9.9949E+00	1.086E+00	5.5156E+00	2.0316E+00
0.100	8.8823E+00	5.5998E-02	-1.0379E+01	1.086E+00	5.5220E+00	2.0340E+00
0.200	8.8791E+00	1.1123E-01	-1.0748E+01	1.086E+00	5.5408E+00	2.0410E+00
0.300	8.8738E+00	1.6500E-01	-1.1103E+01	1.085E+00	5.5716E+00	2.0526E+00
0.400	8.8664E+00	2.1665E-01	-1.1445E+01	1.085E+00	5.6135E+00	2.0688E+00
0.500	8.8569E+00	2.6570E-01	-1.1773E+01	1.085E+00	5.6652E+00	2.0894E+00
0.600	8.8452E+00	3.1175E-01	-1.2087E+01	1.085E+00	5.7252E+00	2.1144E+00
0.700	8.8315E+00	3.5459E-01	-1.2388E+01	1.085E+00	5.7918E+00	2.1436E+00
0.800	8.8157E+00	3.9405E-01	-1.2676E+01	1.085E+00	5.8630E+00	2.1769E+00
0.900	8.7977E+00	4.3016E-01	-1.2951E+01	1.086E+00	5.9365E+00	2.2141E+00
1.000	8.7775E+00	4.6299E-01	-1.3212E+01	1.087E+00	6.0103E+00	2.2551E+00
1.100	8.7550E+00	4.9270E-01	-1.3460E+01	1.088E+00	6.0822E+00	2.2999E+00
1.200	8.7299E+00	5.1946E-01	-1.3695E+01	1.090E+00	6.1501E+00	2.3482E+00
1.300	8.7021E+00	5.4348E-01	-1.3917E+01	1.093E+00	6.2122E+00	2.4000E+00
1.400	8.6714E+00	5.6496E-01	-1.4126E+01	1.097E+00	6.2671E+00	2.4552E+00
1.500	8.6375E+00	5.8410E-01	-1.4322E+01	1.101E+00	6.3138E+00	2.5137E+00
1.600	8.5999E+00	6.0105E-01	-1.4505E+01	1.105E+00	6.3521E+00	2.5755E+00
1.700	8.5582E+00	6.1593E-01	-1.4674E+01	1.111E+00	6.3822E+00	2.6406E+00
1.800	8.5121E+00	6.2881E-01	-1.4829E+01	1.116E+00	6.4056E+00	2.7089E+00
1.900	8.4609E+00	6.3969E-01	-1.4972E+01	1.122E+00	6.4243E+00	2.7806E+00
2.000	8.4040E+00	6.4852E-01	-1.5100E+01	1.129E+00	6.4417E+00	2.8556E+00
2.200	8.2707E+00	6.5947E-01	-1.5315E+01	1.140E+00	6.4907E+00	3.0164E+00
2.400	8.0745E+00	6.4983E-01	-1.5447E+01	1.146E+00	6.6137E+00	3.2048E+00
2.600	7.9285E+00	7.2131E-01	-1.5645E+01	1.340E+00	4.8315E+00	3.3779E+00
2.800	7.9030E+00	7.5395E-01	-1.5880E+01	1.418E+00	4.3852E+00	3.5105E+00
3.000	7.8535E+00	7.6700E-01	-1.6095E+01	1.438E+00	4.1741E+00	3.6482E+00
3.200	7.7665E+00	7.6116E-01	-1.6280E+01	1.437E+00	4.0921E+00	3.7943E+00
3.400	7.6606E+00	7.4018E-01	-1.6452E+01	1.419E+00	4.0837E+00	3.9460E+00
3.600	7.5406E+00	7.0860E-01	-1.6609E+01	1.397E+00	4.1232E+00	4.1027E+00
3.800	7.4112E+00	6.7047E-01	-1.6761E+01	1.371E+00	4.1964E+00	4.2641E+00
4.000	7.2744E+00	6.2941E-01	-1.6903E+01	1.342E+00	4.2950E+00	4.4295E+00
4.200	7.1338E+00	5.8568E-01	-1.7044E+01	1.314E+00	4.4136E+00	4.5985E+00

4.400	6.9911E+00	5.4313E-01	-1.7178E+01	1.283E+00	4.5485E+00	4.7707E+00
4.600	6.8489E+00	5.0253E-01	-1.7308E+01	1.256E+00	4.6970E+00	4.9457E+00
4.800	6.7087E+00	4.6410E-01	-1.7433E+01	1.228E+00	4.8572E+00	5.1232E+00
5.000	6.5720E+00	4.2833E-01	-1.7553E+01	1.203E+00	5.0275E+00	5.3030E+00
5.200	6.4400E+00	3.9535E-01	-1.7666E+01	1.179E+00	5.2068E+00	5.4846E+00
5.400	6.3132E+00	3.6483E-01	-1.7774E+01	1.157E+00	5.3942E+00	5.6680E+00
5.600	6.1921E+00	3.3661E-01	-1.7877E+01	1.137E+00	5.5888E+00	5.8529E+00
5.800	6.0761E+00	3.1065E-01	-1.7977E+01	1.119E+00	5.7901E+00	6.0392E+00
6.000	5.9641E+00	2.8710E-01	-1.8074E+01	1.102E+00	5.9975E+00	6.2266E+00
6.500	5.6907E+00	2.3797E-01	-1.8306E+01	1.065E+00	6.5399E+00	6.6996E+00
7.000	5.4123E+00	2.0134E-01	-1.8526E+01	1.039E+00	7.1124E+00	7.1776E+00
7.500	5.1257E+00	1.7404E-01	-1.8734E+01	1.021E+00	7.7112E+00	7.6595E+00
8.000	4.8388E+00	1.5234E-01	-1.8927E+01	1.005E+00	8.3332E+00	8.1444E+00
8.500	4.5639E+00	1.3335E-01	-1.9097E+01	9.887E-01	8.9762E+00	8.6317E+00
9.000	4.3108E+00	1.1633E-01	-1.9251E+01	9.738E-01	9.6383E+00	9.1208E+00
9.500	4.0789E+00	1.0212E-01	-1.9398E+01	9.622E-01	1.0318E+01	9.6114E+00
10.000	3.8591E+00	9.1239E-02	-1.9544E+01	9.553E-01	1.1015E+01	1.0103E+01
11.000	3.4249E+00	7.5683E-02	-1.9816E+01	9.495E-01	1.2453E+01	1.1090E+01
12.000	3.0142E+00	6.0921E-02	-2.0045E+01	9.424E-01	1.3946E+01	1.2079E+01
13.000	2.6559E+00	5.0571E-02	-2.0265E+01	9.371E-01	1.5488E+01	1.3071E+01
14.000	2.3141E+00	4.4143E-02	-2.0488E+01	9.371E-01	1.7075E+01	1.4064E+01
15.000	1.9897E+00	3.4942E-02	-2.0726E+01	9.350E-01	1.8704E+01	1.5058E+01
16.000	1.7002E+00	2.5537E-02	-2.0934E+01	9.319E-01	2.0370E+01	1.6054E+01
17.000	1.4201E+00	1.7631E-02	-2.1000E+01	9.310E-01	2.2072E+01	1.7049E+01
18.000	1.1530E+00	1.1289E-02	-2.0835E+01	9.293E-01	2.3807E+01	1.8046E+01
19.000	9.0982E-01	1.0198E-02	-2.0456E+01	9.286E-01	2.5572E+01	1.9043E+01
20.000	6.7283E-01	1.2838E-02	-2.0227E+01	9.296E-01	2.7367E+01	2.0040E+01

Table 3-2. Searching range and step for parameters when CTS analysis was performed for each spectrum of Pt foil (coarse search and fine search) and α-MoO_3.

	Parameter	Survey range	Survey step
Pt (Coarse)	S_0^2	0.60–1.40	0.02
	ΔE_0 / eV	0–30	1
	r / Å	2.50–3.00	0.01
	σ^2 / Å^2	0.004–0.007	0.0001
Pt (Fine)	S_0^2	0.60–1.40	0.02
	ΔE_0 / eV	5.0–15.0	0.5
	r / Å	2.75–2.79	0.001
	σ^2 / Å^2	0.0040–0.0070	0.0001
α-MoO_3	S_0^2	1.00	-
	ΔE_0 / eV	0	-
	r_1–r_6 / Å	1.60–2.40	0.05
		$r_1 \le r_2 \le r_3 \le r_4 \le r_5 \le r_6$	
	σ^2 / Å^2	0.0082r–0.0124	

Table 3-3. Results of CTS analysis for Pt L_3-edge EXAFS data for Pt foil. Results of CF analysis gave more digits, but they were neglected to take the error into account.

Parameter	CTS	Curve fitting	m-RMC [8]
S_0^2	0.99 ± 0.09	0.99 ± 0.09	(1.0)
ΔE_0 / eV	9.6 ± 1.3	9.6 ± 1.3	(10.0)
r / Å	2.76 ± 0.01	2.76 ± 0.01	2.77 ± 0.01
σ^2 /Å^2	0.0052 ± 0.0003	0.0052 ± 0.0003	0.0048 ± 0.001
C_3 / Å^3	-	-	0.0001 ± 0.0001

Table 3-4. Results of one- and two-shell CF analyses for α-MoO_3 using REX2000.

Parameter	One shell	Two shells
N_1	0.77	1.36
N_2	-	1.09
$\Delta E_{0\,1}$ / eV	19.9	28.8
$\Delta E_{0\,2}$ / eV	-	30.0
r_1 / Å	1.68	1.71
r_2 / Å	-	1.98
σ^2_1 / Å^2	0.0040	0.0035
σ^2_2 / Å^2	-	0.0016
R-factor	0.3215	0.0127

Table 3-5. Results of CTS analysis for Mo K-edge EXAFS data for α-MoO_3. The average of the structural parameters satisfied *R*-factor < 0.10 under the condition of $r_1 \leq r_2 \leq r_3 \leq r_4 \leq r_5 \leq r_6$.

Parameter	Structure 1	Structure 2	Structure 3
r_1 / Å	1.65	1.70	1.70
r_2 / Å	1.75	1.96	1.70
r_3 / Å	1.94	2.00	1.91
r_4 / Å	1.97	2.25	1.95
r_5 / Å	2.30	2.30	1.98
r_6 / Å	2.34	2.34	2.23

Table 3-6. Parameters of the fine CTS analysis for α-MoO_3. Each domain is shown in Table 3-5. All bond lengths were searched in the searched range and searched steps.

Parameter	Structure 1	Structure 2	Structure 3
S_0^2	1.00	1.00	1.00
ΔE_0 / eV	0	0	0
r_1 / Å	1.60–1.70 / 0.01	1.65–1.75 / 0.01	1.65–1.75 / 0.01
r_2 / Å	1.70–1.80 / 0.01	1.90–2.04 / 0.02	1.65–1.75 / 0.01
r_3 / Å	1.90–2.06 / 0.02	1.90–2.04 / 0.02	1.85–2.05 / 0.02
r_4 / Å	1.90–2.06 / 0.02	2.15–2.45 / 0.03	1.85–2.05 / 0.02
r_5 / Å	2.15–2.45 / 0.03	2.15–2.45 / 0.03	1.85–2.05 / 0.02
r_6 / Å	2.15–2.45 / 0.03	2.15–2.45 / 0.03	2.15–2.45 / 0.03
σ^2 / Å^2		0.0082r–0.0124	

Table 3-7. Results of the CTS analysis of α-MoO_3. The average of each bond from the models that satisfied R-factor < 0.10 under the condition $r_1 \leq r_2 \leq r_3 \leq r_4 \leq r_5 \leq r_6$ are shown. The result of curve fitting analysis [7] and m-RMC analysis [8] are also shown for comparison.

Parameter	Structure 1	Structure 2	Structure 3	CF analysis [7]	m-RMC [8]
r_1 / Å	1.66 ± 0.01	1.69 ± 0.01	1.67 ± 0.01	1.65± 0.02	1.70
r_2 / Å	1.73 ± 0.02	1.96 ± 0.02	1.72 ± 0.02	1.75± 0.02	
r_3 / Å	1.94 ± 0.02	2.00 ± 0.02	1.90 ± 0.03	1.95± 0.02	1.97
r_4 / Å	1.97 ± 0.02	2.25 ± 0.03	1.95 ± 0.02		
r_5 / Å	2.28 ± 0.04	2.30 ± 0.03	2.00 ± 0.03	2.26± 0.02	2.37
r_6 / Å	2.36 ± 0.06	2.36 ± 0.04	2.27 ± 0.04	2.35± 0.02	
R-factor	0.0292	0.0369	0.0401	-	-

Table 3-8. Searching range and step for parameters for Pt foil in the *k*-range of 3.0–6.0 Å^{-1}

Parameter	Searching range	Searching step
S_0^2	0.60–1.20	0.10
ΔE_0 / eV	0–15.0	0.5
r / Å	2.62–2.92	0.01
σ^2 / Å^2	0.001–0.010	0.001

Table 3-9. Results of CTS analysis using the parameters shown in Table 3-8. The averages of parameters were calculated from the points that satisfied *R*-factor < 0.0053.

Parameter	Criterion R <0.0053
Accepted number of points	144
S_0^2	0.76
ΔE_0 / eV	7.4
r / Å	2.74
σ^2 / Å^2	0.0061

Table 3-10. Survey range and step for parameters for Pt foil in the *k*-range of 3.0–6.0 Å^{-1} with a larger survey region.

Parameter	Searching range	Searching step
S_0^2	0.30–3.90	0.10
ΔE_0 / eV	0–15.0	0.5
r / Å	2.62–2.92	0.01
σ^2 / Å^2	0.001–0.0800	0.001

Table 3-11. The results of three shells CTS analysis for Mo K-edge EXAFS of α-MoO_3. Coordination number was fixed at 2+2+2. Six parameters, or three bond lengths and three Debye Waller factors were searched.

Shell	r / Å	σ^2 / Å^2
r_1	1.70	0.0044
r_2	1.96	0.0030
r_3	2.29	0.0088

**R*-factor:0.0110

Table 3-12. Results of CF analysis with three parameter shells for α-MoO_3.

	N	r / Å	σ^2 / Å^2
r_1	1.60	1.70	0.0024
r_2	2.20	1.96	0.0037
r_3	2.44	2.28	0.0079

**R*-factor= 0.0004

Table 3-13. Results of 6 shells CF analyses for α-MoO_3 with different initial parameters.

Parameter	Structure 2		Structure 3	
	Initial	Result	Initial	Result
r_1 / Å	1.70	1.69	1.70	1.67
r_2 / Å	1.96	1.98	1.70	1.72
r_3 / Å	2.00	1.98	1.91	1.88
r_4 / Å	2.25	2.27	1.96	1.98
r_5 / Å	2.30	2.27	1.98	1.98
r_6 / Å	2.34	2.32	2.23	2.27
R-factor		0.0278		0.0330

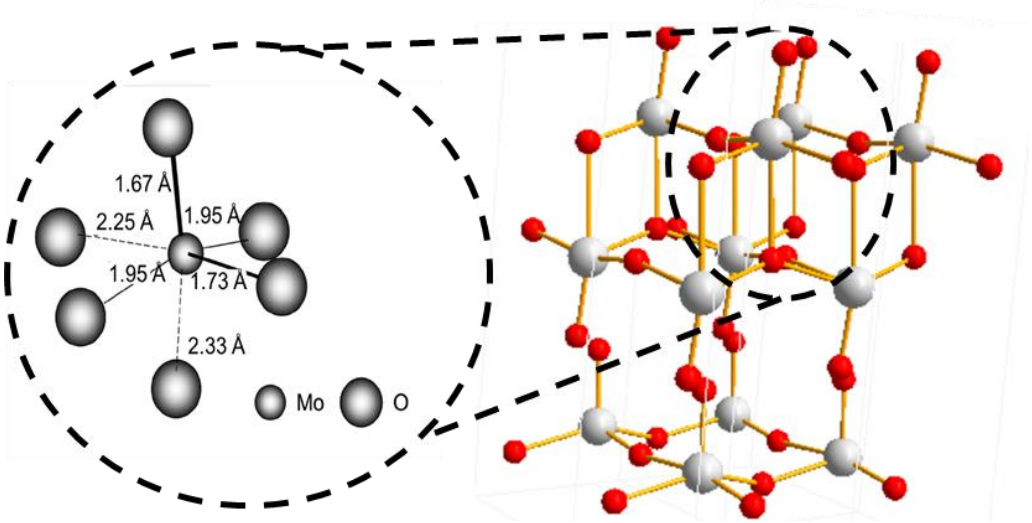

Figure 3-1. Structure of α-MoO_3.[6]

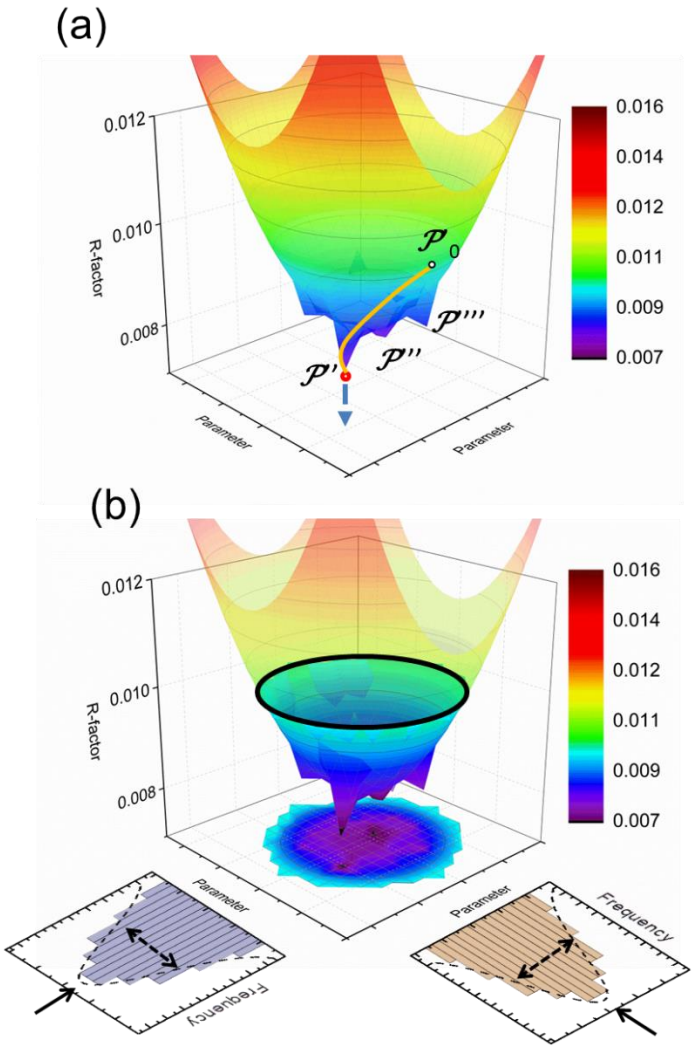

Figure 3-2. Schematic of $R=f(\boldsymbol{\mathcal{P}})$ in (a) CF and (b) TS analyses in 2D parameter space. The *xy* plane is the parameter space and *R* is the *R*-factor. In (a), the black dot represents the initial or searching parameter point and the red dot represents the converged parameter point. In (b), the projected area is the group of points that satisfied a certain *R*-factor. The distributions show the frequency of each parameter in the projected area.

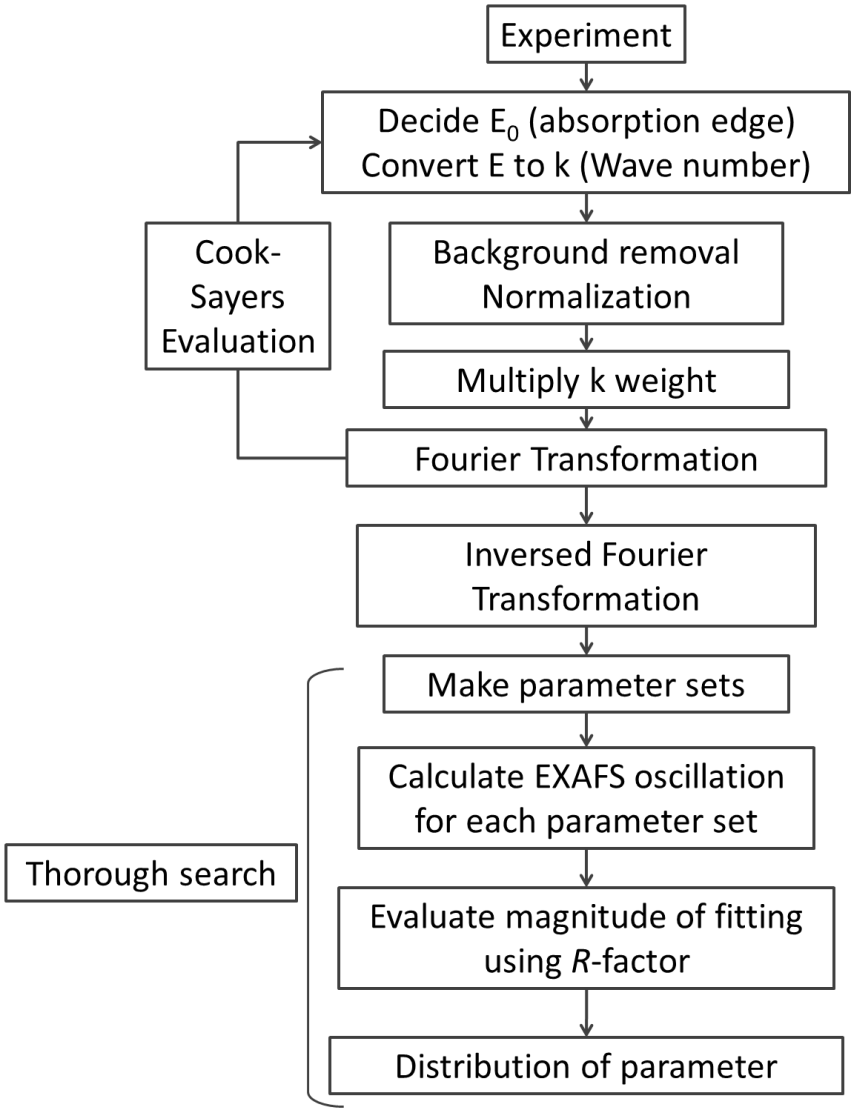

Figure 3-3. Flow chart of CTS analysis.

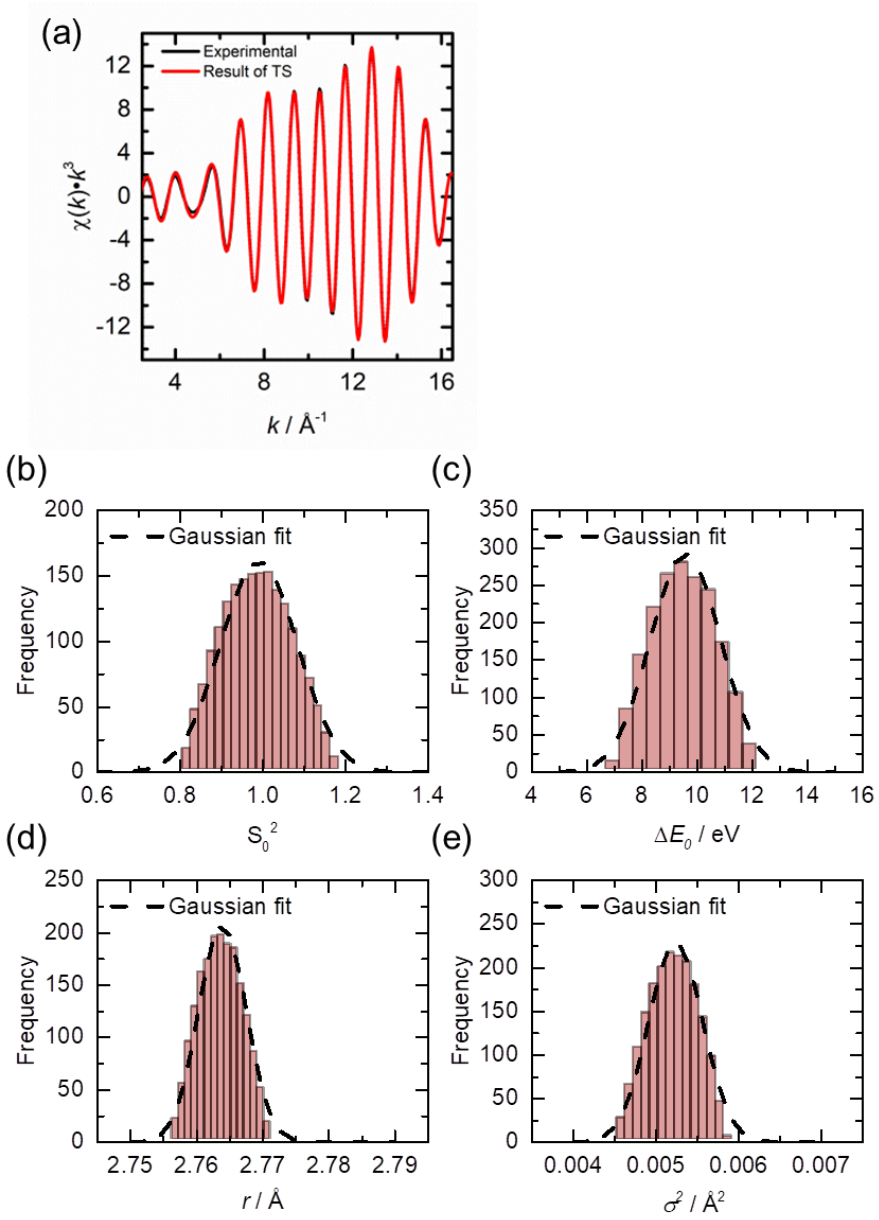

Figure 3-4. (a) Pt L_3-edge inverse Fourier-transformed EXAFS data (black line) and the calculated spectrum based on the CTS analysis result (red line). Frequency distributions for (b) S_0^2, (c) ΔE_0, (d) r, and (e) σ^2. Dashed lines is the Gaussian fits of the distributions.

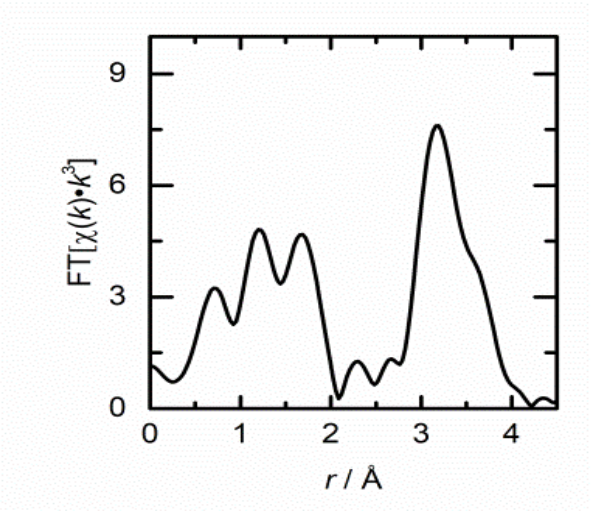

Figure 3-5. Experimental Mo K-edge EXAFS data for α-MoO_3 after Fourier transformation.

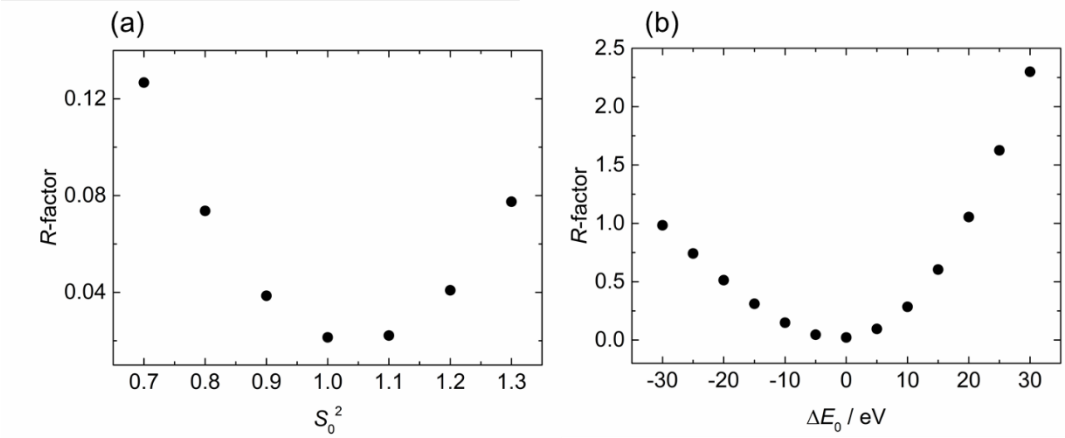

Figure 3-6. The *R*–factor dependence on S_0^2 and ΔE_0 values. (The other structure parameters were fixed at the optimized ones in the CTS analysis.)

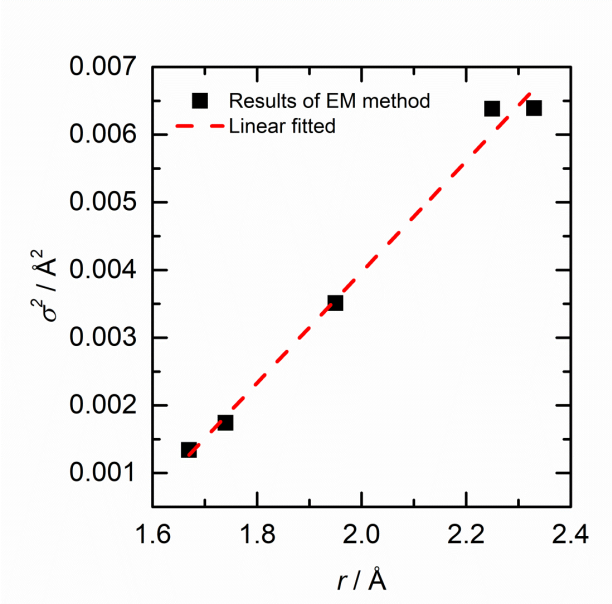

Figure 3-7. Results of the EM method for the Mo-O bonds of α-MoO_3. The dashed line shows the linear fitted result of Debye Waller factor (σ^2) versus bond distance (r).

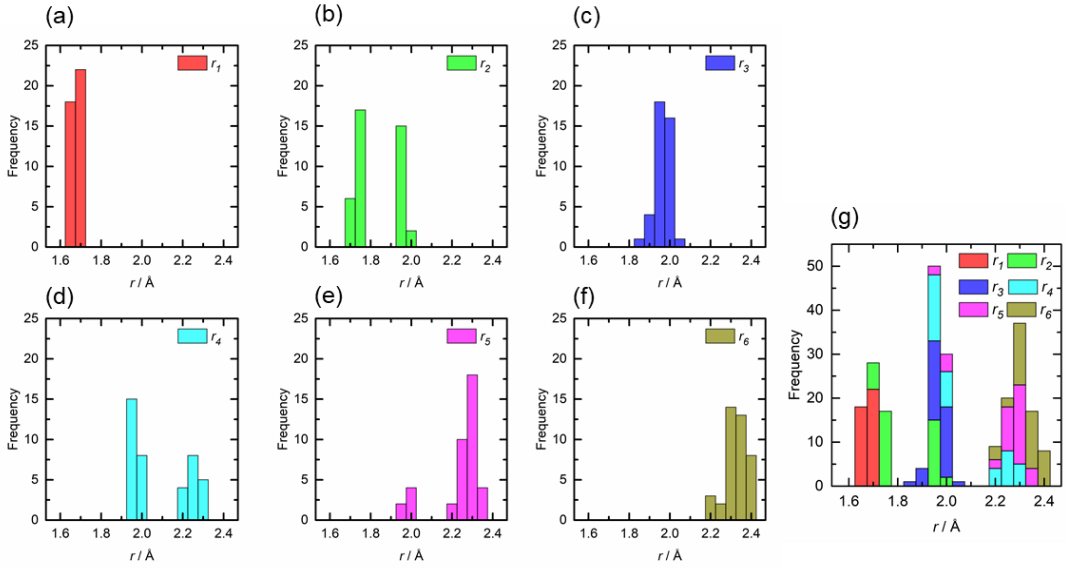

Figure 3-8. (a)–(f) Distribution of each bond from models that satisfied R-factor < 0.10. (g) Compiled distributions. Searched parameters had a step of 0.05 Å and range of 1.60–2.40 Å under $r_1 \leq r_2 \leq r_3 \leq r_4 \leq r_5 \leq r_6$ conditions.

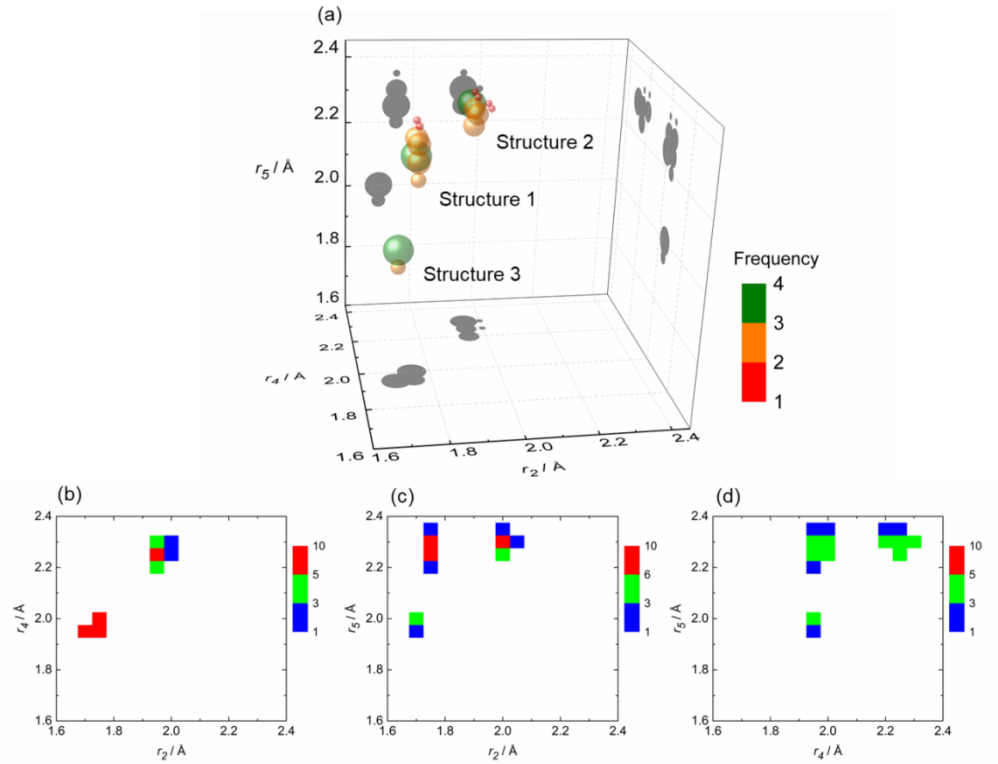

Figure 3-9. (a) 3D mapping of *R*-factor distribution. Size and color indicate the frequency of the points (r_2, r_4, and r_5) including different parameters (r_1, r_3, and r_6). Three domains projected to three planes were found (shown in gray). Projections of the three planes for (b) r_2-r_4, (c) r_2-r_5, and (d) r_4-r_5. Color indicates frequency.

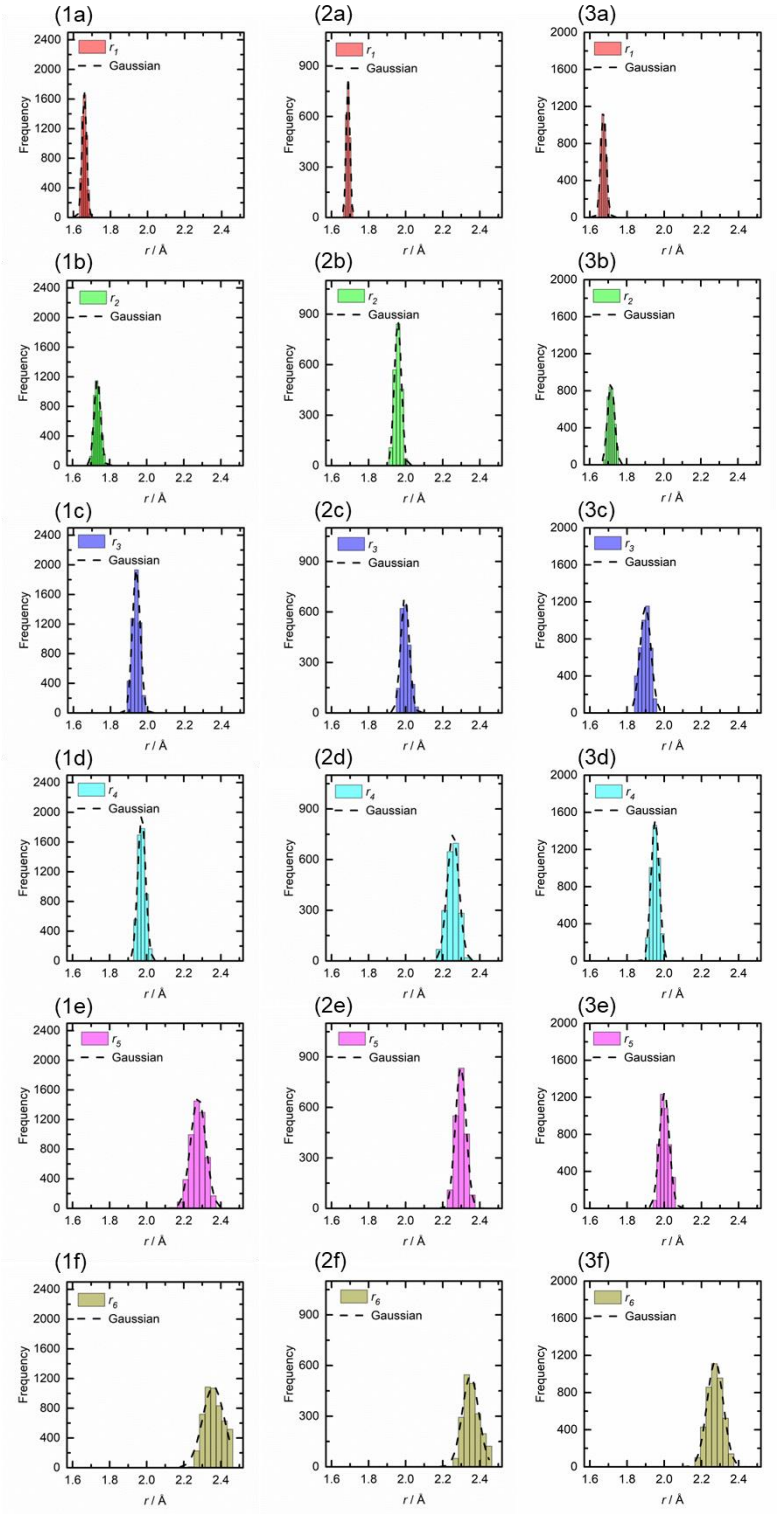

Figure 3-10. Distribution of bond lengths from significance models that satisfied *R*-factor < 0.10 for around Structures1, 2, and 3. Numbers indicate structures and letters indicate r_1 to r_6. Dashed lines show the fitting results using a Gaussian function.

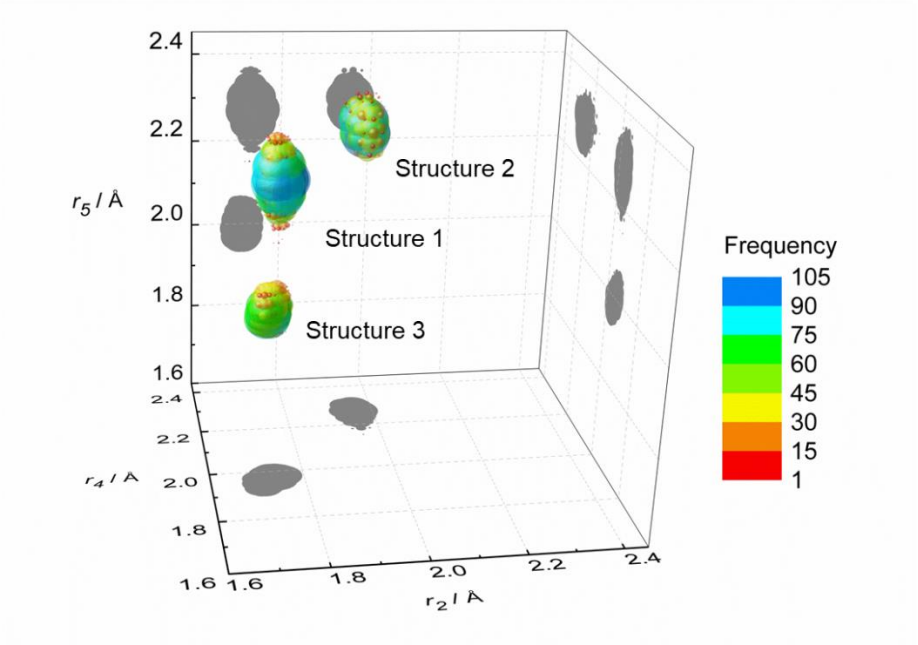

Figure 3-11. 3D distributions of r_2, r_4, and r_5 obtained from models that satisfied R-factor<0.10. Dots at r_2-r_4, r_2-r_5, and r_4-r_5 surfaces show the projection of each bubble.

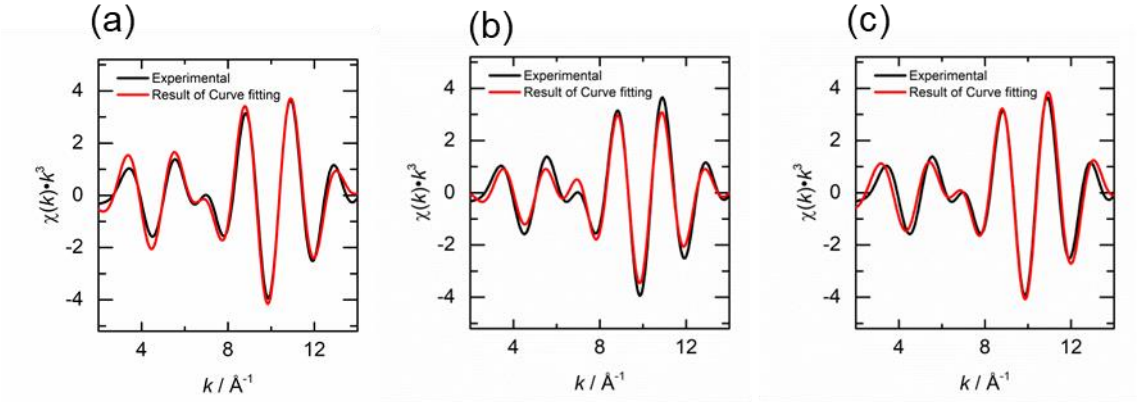

Figure 3-12. Comparison of experimental data with fine CTS analysis results for Mo K-edge EXAFS data shown in Table 3-7. Results for Structure 1, 2, and 3 are shown in (a), (b) and (c), respectively.

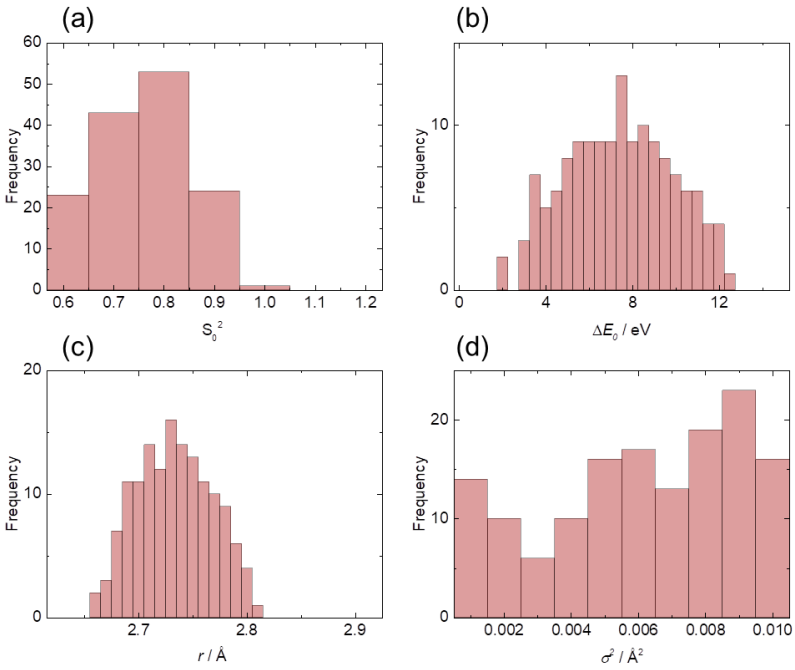

Figure 3-13. Histograms of (a) S_0^2, (b) ΔE_0, (c) r, and (d) σ^2.

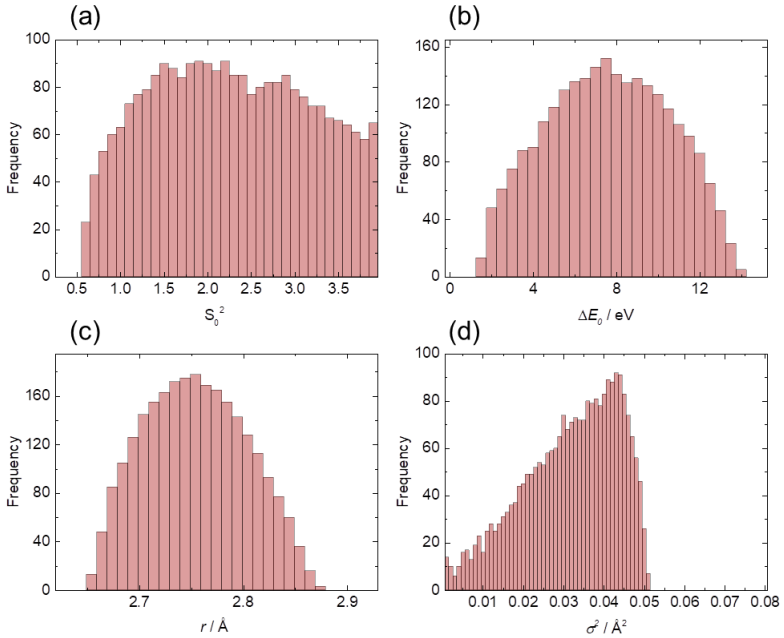

Figure 3-14. Histograms of (a) S_0^2, (b) ΔE_0, (c) r, and (d) σ^2 determined using the larger survey region.

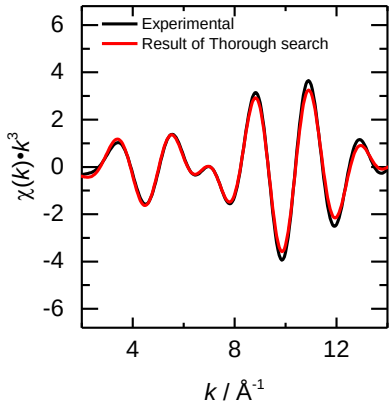

Figure 3-15. Comparison of experimental data with CTS analysis results with three shells for Mo K-edge EXAFS data shown in Table 3-11.

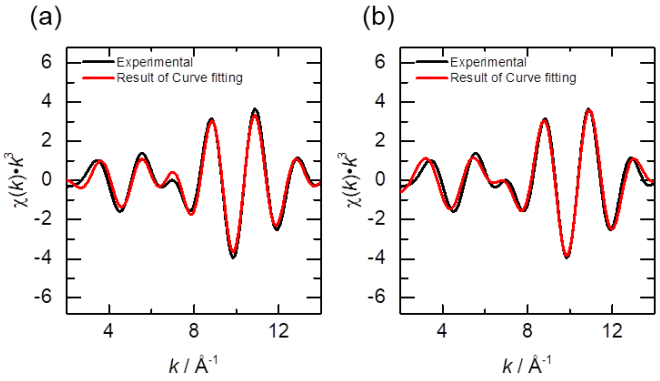

Figure 3-16. Comparison of experimental data with CF analysis results for Mo K-edge EXAFS of α-MoO_3 as shown in Table 3-13. Results for Structure 2 and 3 are shown in (a) and (b), respectively.

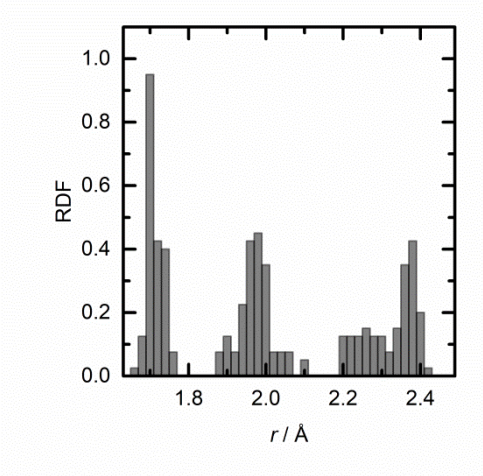

Figure 3-17. Results of m-RMC analysis of Mo K-edge EXAFS data of α-MoO_3.[8]

Reference

1. Y. Iwasawa, K. Asakura, M. Tada (Eds.), XAFS Techniques for Catalysts, Nanomaterials, and Surfaces, Springer, Cham, 2017.
2. K. Asakura, in Y. Iwasawa, (Eds.) X-ray absorption fine structure for catalysts and surfaces. Editor, World Scientific, Singapore, 1996, vol. 2, p 34-58.
3. H. Maeda, Accurate Bond Length Determination by EXAFS Method, J Phys Soc Jpn, 56 (1987) 2777-2787.
4. S.J. Gurman, Interpretation of EXAFS Data, J. Synchrotron Rad., 2 (1995) 56-63.
5. E.A. Stern, Number of relevant independent points in x-ray-absorption fine-structure spectra, Phys. Rev. B, 48 (1993) 9825.
6. L. Kihlborg, Least squares refinement of crystal structure of molybdenum trioxide, Ark. Kemi, 21 (1963) 357-364.
7. W.-J. Chun, K. Ijima, Y. Ohminami, S. Suzuki, K. Asakura, Theoretical Debye–Waller factors of α-MoO3 estimated by an equation-of-motion method, J. Synchrotron Rad., 11 (2004) 291-294.
8. K. Fujikawa, H. Ariga, S. Takakusagi, H. Uehara, T. Ohba, K. Asakura, Micro Reverse Monte Carlo Approach to EXAFS Analysis, e-J. Surf. Sci. Nanotech., 12 (2014) 322-329.
9. R.L. McGreevy, L. Pusztai, Reverse Monte Carlo Simulation: A New Technique for the Determination of Disordered Structures, Molecular Simulation, 1 (1988) 359-367.
10. S.J. Gurman, R.L. McGreevy, Reverse Monte Carlo simulation for the analysis of EXAFS data, J. Phys.: Condens. Matter, 2 (1990) 9463-9473.
11. J. Timoshenko, A. Kuzmin, J. Purans, Reverse Monte Carlo modeling of thermal disorder in crystalline materials from EXAFS spectra, Comput. Phys. Commun., 183 (2012) 1237-1245.
12. M. Harada, R. Ikegami, L.S.R. Kumara, S. Kohara, O. Sakata, Reverse Monte Carlo modeling for local structures of noble metal nanoparticles using high-energy XRD and EXAFS, RSC Advances, 9 (2019) 29511-29521.H. Maeda, Accurate Bond Length Determination by EXAFS Method, J. Phys. Soc. Jpn, 56 (1987) 2777-2787.
13. A. Kompch, A. Sahu, C. Notthoff, F. Ott, D.J. Norris, M. Winterer, Localization of Ag Dopant Atoms in CdSe Nanocrystals by Reverse Monte Carlo Analysis of EXAFS Spectra, J. Phys. Chem. C, 119 (2015) 18762-18772.

14. A.D. Cicco, F. Iesari, A. Trapananti, P. D'Angelo, A. Filipponi, Structure and atomic correlations in molecular systems probed by XAS reverse Monte Carlo refinement, The Journal of Chemical Physics, 148 (2018) 094307.
15. T. Taguchi, T. Ozawa, H. Yashiro, REX2000 Yet Another XAFS Analysis Package, Phys Scr., T115 (2005) 205.
16. M. Newville, Larch: An Analysis Package for XAFS and Related Spectroscopies, J. Phys. Conf. Ser., 430 (2013) 012007.
17. J.J. Rehr, J.J. Kas, M.P. Prange, A.P. Sorini, Y. Takimoto, F. Vila, Ab initio theory and calculations of X-ray spectra, C. R. Physique, 10 (2009) 548-559.
18. W.C. Hamilton, Significance tests on the crystallographic R factor, Acta Crystallogr., 18 (1965) 502-510.
19. W.H. Press, Numerical recipes in C : the art of scientific computing, 2nd ed., Cambridge University Press, Cambridge [England] ; New York, NY, USA, 1992.
20. F. Cotton, R. Wing, Properties of metal-to-oxygen multiple bonds, especially molybdenum-to-oxygen bonds, Inorg. Chem., 4 (1965) 867-873.
21. A. V. Poiarkova, X-ray Absorption Fine Structure Debye- Waller Factors, Ph. D. thesis, University of Washington, 1999.
22. E. D. Crozier, A. Seary, Asymmetric effects in the extended X-ray absorption fine structure analysis of solid and liquid zinc, Canadian Journal of Physics, 58 (1980) 1388-1399.
23. E. D. Croizer, J.J. Rehr, R. Ingalls, in D.C. Koningsberger, R. Prins, (Eds.) X-ray absorption : principles, applications, techniques of EXAFS, SEXAFS, and XANES, Wiley, New York, 1988, p 373-442.
24. M. Newville, Fundamentals of XAFS, Reviews in Mineralogy and Geochemistry, 78 (2014) 33-74.
25. G. Smolentsev, A.V. Soldatov, M.C. Feiters, Three-dimensional local structure refinement using a full-potential XANES analysis, Phys. Rev. B, 75 (2007) 144106.
26. G. Veronesi, C. Degli Esposti Boschi, L. Ferrari, G. Venturoli, F. Boscherini, F.D. Vila, J.J. Rehr, Ab initio analysis of the x-ray absorption spectrum of the myoglobin--carbon monoxide complex: Structure and vibrations, Phys. Rev. B, 82 (2010) 020101.
27. W. Calmano, S. Mangold, E. Welter, An XAFS investigation of the artefacts caused by sequential extraction analyses of Pb-contaminated soils, Fresenius' J. Anal. Chem., 371 (2001) 823-830.

28. E. Curis, S. Benazeth, About estimation of fitted parameters' statistical uncertainties in EXAFS. Critical approach on usual and Monte Carlo methods, J. Synchrotron Rad., 12 (2005) 361-373.
29. M. J. Schalken, C.T. Chantler, Propagation of uncertainty in experiment: structures of Ni (II) coordination complexes, J. Synchrotron Rad., 25 (2018) 920-934.
30. F.A. Schröder, Contributions to the chemistry of Mo and W. XIV. The Mo–O bond length/bond order relationship. A systematical treatment, Acta Cryst., 31 (1975) 2294-2309.
31. B.J. Palmer, D.M. Pfund, J.L. Fulton, Direct Modeling of EXAFS Spectra from Molecular Dynamics Simulations, The Journal of Physical Chemistry, 100 (1996) 13393-13398.
32. P.E. Sinclair, G. Sankar, C.R.A. Catlow, J.M. Thomas, T. Maschmeyer, Computational and EXAFS Study of the Nature of the Ti(IV) Active Sites in Mesoporous Titanosilicate Catalysts, J. Phys. Chem. B, 101 (1997) 4232-4237.
33. D.M. Sherman, C.L. Peacock, C.G. Hubbard, Surface complexation of U(VI) on goethite (α-FeOOH), Geochimica et Cosmochimica Acta, 72 (2008) 298-310.
34. Y. Tang, H.F. Chappell, M.T. Dove, R.J. Reeder, Y.J. Lee, Zinc incorporation into hydroxylapatite, Biomaterials, 30 (2009) 2864-2872.
35. O.M. Roscioni, N. Zonias, S.W.T. Price, A.E. Russell, T. Comaschi, C.-K. Skylaris, Computational prediction of L_3 EXAFS spectra of gold nanoparticles from classical molecular dynamics simulations, Phys. Rev. B, 83 (2011) 115409.
36. L. Valenzano, J.G. Vitillo, S. Chavan, B. Civalleri, F. Bonino, S. Bordiga, C. Lamberti, Structure–activity relationships of simple molecules adsorbed on CPO-27-Ni metal–organic framework: In situ experiments vs. theory, Catal. Today, 182 (2012) 67-79.
37. D. Bocharov, M. Krack, A. Kalinko, J. Purans, F. Rocca, S.E. Ali, A. Kuzmin, Ab initio molecular dynamics simulations of the Sc K-edge EXAFS of scandium trifluoride, J. Phys. Conf. Ser., 712 (2016) 012009.
38. A. Kéri, R. Dähn, M. Krack, S.V. Churakov, Combined XAFS Spectroscopy and Ab Initio Study on the Characterization of Iron Incorporation by Montmorillonite, Environ. Sci. Technol., 51 (2017) 10585-10594.
39. E. Piskorska-Hommel, M. J. Winiarski, G. Kunert, D. Hommel, Polarization-dependent XAFS and density functional theory investigations of the quality of the epitaxial GaMnN structure, J Alloy Compd, 725 (2017) 632-638.

40. G. K. Schenter and J. L. Fulton, in Y. Iwasawa, K. Asakura, and M. Tada, (Eds.) XAFS Techniques for Catalysts, Nanomaterials, and Surfaces. Springer, Cham, 2017, p. 251.
41. K. Tokuda, J. Iihara, Y. Saito, A. Masuno, H. Inoue, Structural analysis of sulfuric acid solutions containing Ti and Mn using x-ray diffraction, x-ray absorption fine structure, and molecular dynamics simulation, J. Chem. Phys., 149 (2018) 014503.
42. P. Dziegielewski, O. Mathon, I. Kantor, S. Pascarelli, T. Shinmei, T. Irifune, J. Antonowicz, High pressure atomic structure of Zr–Cu metallic glass via EXAFS spectroscopy and molecular dynamics simulations, High Press. Res., (2019) 1-11.
43. I.D. Brown, Bond valences—a simple structural model for inorganic chemistry, Chem. Soc. Rev., 7 (1978) 359-376.
44. Y. Iwasawa, K. Asakura, H. Ishii, H. Kuroda, DYNAMIC BEHAVIOR OF ACTIVE-SITES OF A SIO2-ATTACHED MO(VI)-DIMER CATALYST DURING ETHANOL OXIDATION OBSERVED BY MEANS OF EXAFS, Z. Phys. Chem. N. F., 144 (1985) 105-115.
45. Y. Uemura, H. Uehara, Y. Niwa, S. Nozawa, T. Sato, S. Adachi, B. Ohtani, S. Takakusagi, K. Asakura, In Situ Picosecond XAFS Study of an Excited State of Tungsten Oxide, Chem. Lett., 43 (2014) 977-979.
46. Y. Uemura, D. Kido, Y. Wakisaka, H. Uehara, T. Ohba, Y. Niwa, S. Nozawa, T. Sato, K. Ichiyanagi, R. Fukaya, S. Adachi, T. Katayama, T. Togashi, S. Owada, K. Ogawa, M. Yabashi, K. Hatada, S. Takakusagi, T. Yokoyama, B. Ohtani, K. Asakura, Dynamics of Photoelectrons and Structural Changes of Tungsten Trioxide Observed by Femtosecond Transient XAFS, Angew. Chem. Int. Edit., 55 (2016) 1364-1367.
47. A. Koide, Y. Uemura, D. Kido, Y. Wakisaka, S. Takakusagi, B. Ohtani, Y. Niwa, S. Nozawa, K. Ichiyanagi, R. Fukaya, S.I. Adachi, T. Katayama, T. Togashi, S. Owada, M. Yabashi, Y. Yamamoto, M. Katayama, K. Hatada, T. Yokoyama, K. Asakura, Photoinduced anisotropic distortion as the electron trapping site of tungsten trioxide by ultrafast W L1-edge X-ray absorption spectroscopy with full potential multiple scattering calculations, Phys. Chem. Chem. Phys., (2019).
48. G.H. Via, K.F. Drake, G. Meitzner, F.W. Lytle, J.H. Sinfelt, Analysis of EXAFS data on bimetallic clusters, Catal. Lett., 5 (1990) 25-33.
49. C.-R. Bian, S. Suzuki, K. Asakura, L. Ping, N. Toshima, Extended X-ray Absorption Fine Structure Studies on the Structure of the Poly(vinylpyrrolidone)-Stabilized Cu/Pd Nanoclusters Colloidally Dispersed in Solution, J. Phys. Chem. B, 106 (2002) 8587-8598.

50. T. Takeguchi, T. Yamanaka, K. Asakura, E.N. Muhamad, K. Uosaki, W. Ueda, Evidence of Nonelectrochemical Shift Reaction on a CO-Tolerant High-Entropy State Pt–Ru Anode Catalyst for Reliable and Efficient Residential Fuel Cell Systems, J. Am. Chem. Soc., 134 (2012) 14508-14512.
51. S.D. House, C.S. Bonifacio, J. Timoshenko, P. Kunal, H. Wan, Z. Duan, H. Li, J.C. Yang, A.I. Frenkel, S.M. Humphrey, R.M. Crooks, G.A. Henkelman, Computationally Assisted STEM and EXAFS Characterization of Tunable Rh/Au and Rh/Ag Bimetallic Nanoparticle Catalysts, Microsc. Microanal., 23 (2017) 2030-2031.
52. C. Evangelisti, A. Balerna, R. Psaro, G. Fusini, A. Carpita, M. Benfatto, Characterization of a Poly-4-Vinylpyridine-Supported CuPd Bimetallic Catalyst for Sonogashira Coupling Reactions, Chem.Phys Chem, 18 (2017) 1921-1928.
53. M. Sankar, Q. He, S. Dawson, E. Nowicka, L. Lu, P.C.A. Bruijnincx, A.M. Beale, C.J. Kiely, B.M. Weckhuysen, Supported bimetallic nano-alloys as highly active catalysts for the one-pot tandem synthesis of imines and secondary amines from nitrobenzene and alcohols, Catal. Sci. Technol., 6 (2016) 5473-5482.
54. N.M. Bedford, A.R. Showalter, T.J. Woehl, Z.E. Hughes, S. Lee, B. Reinhart, S.P. Ertem, E.B. Coughlin, Y. Ren, T.R. Walsh, B.A. Bunker, Peptide-Directed PdAu Nanoscale Surface Segregation: Toward Controlled Bimetallic Architecture for Catalytic Materials, ACS Nano, 10 (2016) 8645-8659.
55. Z. Duan, Y. Li, J. Timoshenko, S.T. Chill, R.M. Anderson, D.F. Yancey, A.I. Frenkel, R.M. Crooks, G. Henkelman, A combined theoretical and experimental EXAFS study of the structure and dynamics of Au147 nanoparticles, Catal. Sci. Technol., 6 (2016) 6879-6885.
56. D. Liu, Y. Li, M. Kottwitz, B. Yan, S. Yao, A. Gamalski, D. Grolimund, O.V. Safonova, M. Nachtegaal, J.G. Chen, E.A. Stach, R.G. Nuzzo, A.I. Frenkel, Identifying Dynamic Structural Changes of Active Sites in Pt–Ni Bimetallic Catalysts Using Multimodal Approaches, Acs Catal., 8 (2018) 4120-4131.
57. S. Takakusagi, W.-J. Chun, H. Uehara, K. Asakura, Y. Iwasawa, Polarization-Dependent Total-Reflection Fluorescence X-ray Absorption Fine Structure for 3D Structural Determination and Surface Fine Tuning, Top. Catal., 56 (2013) 1477-1487.
58. H. Uehara, Y. Uemura, T. Ogawa, K. Kono, R. Ueno, Y. Niwa, H. Nitani, H. Abe, S. Takakusagi, M. Nomura, Y. Iwasawa, K. Asakura, In situ back-side illumination fluorescence XAFS (BI-FXAFS) studies on platinum nanoparticles deposited on a

HOPG surface as a model fuel cell: a new approach to the Pt-HOPG electrode/electrolyte interface, Phys. Chem. Chem. Phys., 16 (2014) 13748-13754.

59. K. Asakura, Y. Iwasawa, K. Asakura, and M. Tada, (Eds.) XAFS Techniques for Catalysts, Nanomaterials, and Surfaces. Springer, Cham, 2017, p. 527.
60. K. Asakura, S. Takakusagi, H. Ariga, W.-J. Chun, S. Suzuki, Y. Koike, H. Uehara, K. Miyazaki, Y. Iwasawa, Preparation and structure of a single Au atom on the TiO2(110) surface: control of the Au–metal oxide surface interaction, Faraday Discuss., 162 (2013) 165-177.
61. S. Takakusagi, H. Nojima, H. Ariga, H. Uehara, K. Miyazaki, W.-J. Chun, Y. Iwasawa, K. Asakura, Fine tuning and orientation control of surface Cu complexes on TiO2(110) premodified with mercapto compounds: the effect of different mercapto group positions, Phys. Chem. Chem. Phys., 15 (2013) 14080-14088.
62. Q. Yuan, S. Takakusagi, Y. Wakisaka, Y. Uemura, T. Wada, H. Ariga, K. Asakura, Polarization-dependent Total Reflection Fluorescence X-ray Absorption Fine Structure (PTRF-XAFS) Studies on the Structure of a Pt Monolayer on Au(111) Prepared by the Surface-limited Redox Replacement Reaction, Chem. Lett., 46 (2017) 1250-1253.
63. Q. Yuan, Y. Wakisaka, Y. Uemura, T. Wada, H. Ariga-Miwa, S. Takakusagi, K. Asakura, S.R. Brankovic, Reaction Stoichiometry and Mechanism of Pt Deposition via Surface Limited Redox Replacement of Copper UPD Layer on Au(111), J. Phys. Chem. C, 122 (2018) 16664-16673.

Chapter 4. Application of constrained thorough search method for structural change of tungsten trioxide using ultrafast EXAFS

4.1. Introduction

X-ray absorption spectroscopy (XAS) is one of the essential analytical methods for characterizing materials. XAS can be applied to various kinds of conditions such as liquids or solids. XAS can address the electronic states and structures of a specific element in a material under investigation. In particular, extended X-ray absorption fine structure (EXAFS), which is small oscillation features in XAS and appears from 50 eV to 1000 eV above an X-ray absorption edge, have been widely accepted as an analytical tool to determine the local structure of a specific element.[1] EXAFS is useful in order to know the local structures of materials composed by several elements or lacking a long-range order. It is known that EXAFS oscillations can be reproduced by using an equation,

$$\chi(k) = \sum_i \frac{{S_0}^2 N_i F_i(k)}{k{r_i}^2} \exp\left(-\frac{2r_i}{\lambda}\right) \exp(-2{\sigma_i}^2 k^2) \sin\left(2kr_i + \phi_i(k)\right)$$

$$k = \sqrt{\frac{2m}{\hbar^2}\left(h\upsilon - (E_0 + \Delta E_0)\right)}$$

(4-1)

where ${S_0}^2$, $F_i(k)$, $\phi_i(k)$, λ, m, $h\upsilon$, and E_0 are the inelastic energy loss, backscattering amplitude and phase shift functions, inelastic mean free path, mass of an electron, X-ray energy, and absorption edge energy, respectively. And N, ΔE_0, r, and σ^2 are parameters such as coordination number, correction of the origin of kinetic energy zero, bond length, and Debye Waller factor, respectively. Although EXAFS oscillations can be calculated and analyzed by the conventional analysis method i.e. curve fitting (CF) method, there is a problem when CF method is applied to a complex system such as MoO_3.[2] If the bond length between a target atom and each surrounding atom is different from each other, the number of parameters to be examined should become large. In case of MoO_3, a Mo ion is bonded to 6 oxygen ions and Mo-O bonds are 5 different length. If we tried to elucidate the local structure of MoO_3 by reproducing the EXAFS oscillations without any boundary conditions or constraints for the parameters, 24 different parameters have to be optimized. When the number of parameters increases, it should be difficult to find out an optimal parameter set. The

solutions proposed by the CF method easily converge to local minima because of the dependence of initial guess for the parameter set and the correlations of parameters. In order to overcome this classical problems in the CF analysis, I have proposed constrained thorough search (CTS) EXAFS analysis method.[2] In the CTS method, each parameter in EXAFS equation mentioned above (N, ΔE_0, r, and σ^2) is searched step by step in a parameter space. It is possible to pick up all candidates which reproduce the experimental data well. In addition, the other structures are rejected because they cannot reproduce the experimental data. Although it takes longer time to explore all the optimal parameter sets than the CF method, the local minima and initial guess problems can be avoided. By employing the CTS method, the local structure of MoO_3 was successfully determined and there were 3 candidates which can reproduce the EXAFS oscillations of MoO_3.

There are advantages of the CTS method including mentioned above.

1. It is possible to pick up all candidate structures which reproduce the experimental data well and to reject the other structures.
2. The dependence of the initial parameter for analysis is removed.
3. Structural constraints are easily combined with searching parameters.
4. Error estimations are performed based on the distributions of parameters.
5. The parallel computing can be employed to explore the whole parameter space in shorter time.
6. It is expected that the CTS method is applicable to analyzing the change of EXAFS during a chemical reaction, photoexcitation, and so on because the search of structural parameters can start from the initial state.
7. A combination of rough and fine search can be employed if a large parameter space should be searched, which makes it possible to walk through the entire parameter space quickly.
8. Visualizing the correlation of parameters helps to set proper boundary conditions or constraints.

Therefore, the CTS method is an alternative approach to analyze EXAFS data which is hardly analyzed by the conventional CF framework.

One of the most challenging issues in EXAFS analysis is to elucidate photoexcited state of materials measured by a time-resolved XAFS method. Since EXAFS oscillations are weak signals and the ratio of the photoexcited state of a material is usually not large, it is difficult to obtain a good EXAFS signal over a wide energy range. Therefore, the number of available parameters is limited because of the low degrees of

freedom. In general, it is hard to determine a local structure of the photoexcited state of materials only from the conventional EXAFS analysis approach. Despite such difficulties, there are some examples to determine the structures of the photoexcited state of materials using pump-probe EXAFS[3-10]. For example, organometallic compounds with a high symmetrical structure around the central metal ions were investigated or supplemental information was provided by DFT calculations. To the best of my knowledge, there have been no studies on investigating ultrafast structural change of complex materials such as oxides only based on EXAFS analysis.

In this chapter, I demonstrate that the W L_3-edge EXAFS of photoexcited WO_3 measured by the time-resolved XAFS was analyzed by the CTS method. The photoexcitation processes of WO_3 have been studied using ultrafast time-resolved XAFS measurement.[11-13] Picosecond and femtosecond time-resolved W L_3-edge X-ray absorption near edge structure (XANES) studies elucidated a fast photoexcitation process and following relaxation steps. The photoexcitation induced the electron transfer from oxygen ion to W^{6+} to create the W^{5+} (< 1ps) followed by geometrical structural change within 200 ps after the photoexcitation keeping the valence state to attain the metastable state. The W L_1-edge XANES study was also conducted and from the result of the W L_1–edge XANES analysis, it was suggested that the anisotropic structural change should occur in the metastable state. However, I have not yet figured out the details of the structural change in the metastable state, i.e., the structural parameters of the metastable WO_3 have been not determined precisely. Since the CTS method can collect as many candidates as possible which can reproduce the experimental data well and visualize the correlation of parameters, it is possible to determine the details of the structural changes of the photoexcited WO_3. I will propose the detailed structure of the metastable WO_3 at a delay time of 150 ps after photoexcitation.

4.2. Experimental

4.2.1. Material

WO_3 was purchased from Wako Chemicals. WO_3 nanoparticles (diameter was 50-200 nm) were prepared according to Ref. 14 and the concentration of WO_3 was about 2.5 $mmolL^{-1}$ in the W base. The WO_3 suspension was pumped up to nozzle (diameter of the nozzle was 500 μm) using magnetic gear pump.

4.2.2. Experimental method

The pump-probe XAFS measurement was carried out at beamline NW14A in Photon

Factory Advanced Ring (PF-AR) of Institute of Materials Structure Science (IMSS), High Energy Accelerator Organization (KEK-IMSS), Tsukuba, Japan.[15] The pulse width and the repetition rate of X-ray from the PF-AR were 100 ps and 794 kHz, respectively. X-ray was monochromatized by a Si(111) double crystal monochrometer. The intensity of the incident X-ray was measured by an ion chamber filled with nitrogen. The XAFS was measured by a fluorescence mode using a photomultiplier tube equipped with a plastic scintillator. The elastic X-ray was attenuated by a Cu filter and a solar slit. A Ti:sapphire laser was used for photoexcitation. The fundamental wave (~800 nm) was doubled to 400 nm by a barium borate crystal (BBO). The pulse width and the repetition rate of the laser were 1 ps and 945 Hz, respectively. The XAFS signal was separated into before and after the laser irradiation using two boxcar integrators. In this study, the delay was 150 ps after the laser irradiation.

4.2.3. EXAFS analysis

Data processing of EXAFS was carried out using REX2000 (RIGAKU)[16]. The background removal and normalization of EXAFS spectra were conducted by spline smoothing method and the EXAFS oscillations were extracted according to Cook and Sayer's criteria[17]. FEFF8.2 code[18] was used computing the backscattering amplitude and the phase shift of the bonds between X-ray absorbing atom (tungsten ion) and surrounding oxygen ions theoretically. In CTS method, the calculation of EXAFS oscillations for each model structure was carried out using "Larch" package. Larch package is an analytical framework based on Python designed for analyzing various kinds of X-ray measurements techniques in synchrotrons.[19] I utilized the functions of EXAFS analysis in Larch.

The degrees of freedom were 5 in the analysis for the change of W L_3-edge EXAFS. Thus the number of searching parameters was limited. Some parameters were estimated empirically and theoretically to search the parameters more effectively in CTS method. The S_0^2 and ΔE_0 were referred to Na_2WO_4, 0.75±0.05 and 17±1 eV, respectively since Na_2WO_4 has W^{6+} and well-defined local structure. The Debye Waller factor was estimated using Equation of Motion (EM) Method.[20] The force constant of W-O bond was gotten from Ref. 21. The Debye Waller factor obtained from EM method in the ground state WO_3 strongly dependent on the W-O distances that was approximated as because the force constant was related to the bond distance.[22] In the metastable state, the Debye Waller factor was not only bond distance but also the temperature. I roughly estimated the temperature as 765 K and the Debye Waller factor was estimated as the function of bond length between W and O; $\sigma^2=(6.4\times10^{-6})\exp(3.33r)$ Å^2 as shown in Figure 4-1. The range of Fourier

transformation was 3.0-8.0 $Å^{-1}$ and *k* weight was 0. The range of inversely Fourier transformation was 1.0-2.0 Å. The degrees of freedom (2×5×1/π+2) was 5.[23] The window function of both Fourier transformations was Hanning function. As the ground state of WO_3, W L_3-edge EXAFS which measured by a transmission mode was used for analysis. EXAFS spectra were analyzed by CTS method. The surveyed range and steps for the analysis of ground state is shown in Table 4-1. As the results, the ground state of WO_3 was successfully reproduced as shown in Table 4-2. The surveyed range and steps for the analysis of the metastable of WO_3 are shown in Table 4-3.

4.3. Results

4.3.1. Results of time-resolved XANES and EXAFS measurement

Figure 4-2 shows the differences in the W L_3-edge EXAFS spectra between the optical ground state and the photoexcited state at a delay time of 150 ps. It was reported that the metastable state was formed at a delay time of 150 ps after photoexcitation.[12,13] The differences in the EXAFS shown in Figure 4-2 comes from the structural difference between the optical ground state and the metastable state of WO_3. The differences in the EXAFS, $\Delta\chi(k)$, can be described as

$$\Delta\chi(k) = \chi(k)_{After\ laser\ irradiation} - \chi(k)_{Before\ laser\ irradiation} \quad (4\text{-}2)$$

where, $\chi(k)_{After\ laser\ irradiation}$ and $\chi(k)_{Before\ laser\ irradiation}$ denote the observed EXAFS after and before photoexcitation, respectively. These observed data consist of the EXAFS of the photoexcited state ($\chi(k)_{Photoexcited\ state}$) and that of the optical ground state ($\chi(k)_{Ground\ state}$).

$$\chi(k)_{After\ laser\ irradiation} = \alpha\chi(k)_{Photoexcited\ state} + (1-\alpha)\chi(k)_{Ground\ state} \quad (4\text{-}3)$$

and

$$\chi(k)_{Before\ laser\ irradiation} = \chi(k)_{Ground\ state} \ . \quad (4\text{-}4)$$

Here, α is the ratio of the photoexcited state to the ground state after laser irradiation. The ratio of photoexcited state was estimated from the change of W L_3-edge XANES. The valence band and the conduction band of WO_3 mainly consist of O 2p orbital and W 5d orbital, respectively. Thus an electron is photoexcited from O 2p to W 5d orbital in photoexcitation process of WO_3. In W L_3-edge XANES, an electron which is in W $2p_{3/2}$ orbital is excited to W 5d orbital. Therefore, the differences of absorption

coefficient in the XANES region as shown in Figure 4-3(a) show the occupancy of W 5d orbital.[12] The area ratio of the XANES spectrum after laser irradiation was 0.95 and the ratio of photoexcitation was estimated as 45±5 % from the relation of Figure 4-3(b). Consequently, the Equation (4-2) can be written as

$$\Delta\chi(k) = \alpha\{\chi(k)_{Photoexcited\ state} - \chi(k)_{Ground\ state}\} \ . \tag{4-5}$$

The calculated differences of EXAFS as shown in Equation (4-5) were used to evaluate if a model structure can reproduce the observed EXAFS. *R*-factor which is commonly used to evaluate the goodness of fitting was employed in order to figure out how a model structure reproduced the observed EXAFS. For the differences of EXAFS, *R*-factor was defined as Equation (4-6).

$$R - \text{factor} = \frac{\sum\{\Delta\chi_{data}(k) - \Delta\chi_{calculated}(k)\}^2}{\sum\{\Delta\chi_{data}(k)\}^2} \tag{4-6}$$

Here, $\Delta\chi_{data}(k)$ and $\Delta\chi_{calculated}(k)$ were differences of experimental spectra as shown in Equation (4-2) and differences of calculated spectra as shown in Equation (4-5), respectively. In this chapter, the limitation of *R*-factor to decide the calculated spectrum is accepted or not was 0.10. I would like to discuss why I used 0.10 later.

Since it would take longer time to explore a whole parameter space, it is useful to test parameter sets which have smaller number of parameters. Therefore, first, I carried out 3 shells analysis where the 6 W-O bonds were treated as 3 kinds of bonds. Then, I did 4 shells analysis where the shortest bond in 3 shells analysis was treated separately. Thus 3 shells' analysis gave the appropriate parameter range for 4 shells' analysis. Since the structural distortion suggested by W L_1–edge XANES analysis is that the shortest bond became shorter and symmetry around W ion became worse, I paid attention to the shortest bond in 4 shells analysis. 4 shells analysis was limitation of analysis because the degrees of freedom were 5 for the differences of EXAFS. In order to check the feasibility of the procedures which 3 shells and 4 shells analysis, I carried out it on the EXAFS spectrum of a standard WO_3 compound. I started the 3 shells analysis and proceeded to the 4 shells analysis. The surveyed range and steps for the analysis of ground state and metastable state of WO3 are shown in Table 4-1 and 4-3, respectively.

4.3.2. Results of constrained thorough search analysis

Figure 4-4 shows the 3D plot of parameters which satisfied *R*-factor<0.10 in 3 shells CTS analysis for the change in time-resolved W L_3-edge EXAFS. Accepted parameter

sets which satisfied *R*-factor<0.10 was 229 out of about 3.6×10^5 searched parameter sets. As shown in Figure 4-4, only one structure's domain was obtained from surveyed region. The bond lengths obtained from 3 shells CTS analysis were 1.75 ± 0.02, 1.99 ± 0.04 and 2.20 ± 0.08 as shown in Table 4-4. The results of 3 shells analysis for the metastable state were not so different from the results of the ground state as shown Table 4-2. However, 4 shells analysis was carried out. The survey conditions were decided based on result of 3 shells analysis as shown in Table 4-3. Figure 4-5 shows the histograms of parameters which satisfied *R*-factor<0.10 in the CTS analysis. Table 4-4 shows the results of 4 shells CTS analysis. Accepted parameter sets which satisfied *R*-factor<0.10 were 7,451 out of about 6.3×10^5 searched parameter sets. Figure 4-6 shows the cross sections which cut the global minimum in parameter space and 3D plots for the results of CTS analysis in the ground state and the metastable state of WO_3, respectively. When the $r_1 \leq r_2$ condition was introduced, the half of cross section divided by Equation $r_1=r_2$ was ignored. Thus the average of each bond moved from global minimum in case of the ground state. In CTS method, it is expected that the histogram reflects the distribution of *R*-factor even though the surveyed space is multi-dimensional parameter space. When the area of significant parameters exists on the border of constrained condition, averages can move a little from minimum of selected region. However, the parameters of global minimum showed the same features of the crystallographic data for the ground state as shown in Table 4-2, or the acceptable parameters are spread from global minimum as shown in Figure 4-6. In addition, the distribution of parameters in the parameter space is significantly different between the ground state and the metastable state. As the result of CTS analysis, it can be suggested that r_1 became 1.67 ± 0.06 Å in the photoexcited state. The result of CTS analysis as shown in Table 4-4 reproduced experimental data well as shown in Figure 4-7.

4.4. Discussion

The measurement of W L_3-edge EXAFS of WO_3 in the metastable state was carried out in picosecond time resolution. It was enough time resolution to observe the structural change in the metastable state which already reported from the time dependent change of W L_1- and L_3- edge XANES.[12,13] The change of EXAFS was obtained successfully. CTS method was carried out for analyzing the change of W L_3-edge EXAFS of WO_3 in the metastable state. The candidate of structure in the metastable state was obtained which reproduces the experimental data well. Here, I would like to discuss 2 points. 1. The significance of the structural change obtained

from the CTS analysis, and 2. The comparison with previous reports.

4.4.1. The significance of the structural change obtained from the CTS analysis

CTS analysis was carried out to reveal the structural change of WO_3 in the metastable state. The degrees of freedom were 5 and it was very low. The advantage of CTS analysis is that it can survey the whole parameter subspace and pick up the local minima if they exist. Therefore, the CTS analysis insures that the obtained structure was unique in the searched parameter space. In other words, it is insured that the other structures which cannot be picked up were less reproduced observed data in this parameter subspace. In case of WO_3, the monoclinic phase[24] and orthorhombic phase[25] are representative crystal structure. However, the CTS analysis didn't pick up such structures in 3 shells analysis and it didn't reproduce the change of EXAFS as shown in Figure 4-8. It is consistent with the results of W L_1-edge XANES.[13] The $r_1 \leq r_2$ condition introduced separation of r_1 and r_2 in the results of the ground state. Molybdenum oxide (MoO_3) also has the pair of the almost same bond length and analyzed by CTS method.[2] However, it didn't show large differences such as 0.10 Å in case of the WO_3 ground state as shown in Table 4-2. Two reasons can be considered. One is the number of shells for the analysis. This can be make differences in constraint condition among the parameters. In the analysis of MoO_3, the number of shells was 6. In this study, 4 shells analysis was carried out and 2 bonds are treated as 1 shell in r_3 and r_4 with treating their coordination number as 2, respectively. When the 2 bonds are treated in 1 shell, the distribution of r_4 can be larger than the case to treat two bonds separately. As the result of spreading of distribution, the other parameters also affected because these parameters have correlation. Second is the level of acceptance, or limitation of *R*-factor. It is because the shape of distribution should be changed when the cross section of acceptable region is changed. Ideally, significance test or probability evaluations should be introduced. However, the degrees of freedom were too small to perform significance tests or probability evaluations. Therefore, *R*-factor<0.10 was introduced as the temporal standards for judging in this analysis. The global minimum on the analysis of WO_3 showed very small *R*-factor and less than 0.01 for the results of CTS analysis of WO_3 in the ground state and metastable state. If the criterion of *R*-factor is changed from 0.10 to 0.01, distributions obtained from CTS analysis became sharp and average of distribution shifted close to the global minimum as shown in Figure 4-9 and Figure 4-10. Thus there is a possibility that accepted parameter sets were too much and more strictly *R*-factor limitation can be accepted. To improve this problem, EXAFS spectra measured in a larger k region (k > 10 Å) with higher quality should be required.

Nevertheless, the obtained result for the ground state seems to be acceptable because the parameters of global minimum showed the same features of the crystallographic data for the ground state and the acceptable parameters are spread from global minimum. In addition, the shape of distributions and cross sections were obviously different between the results for the ground state and the metastable state. Therefore, even though the errors can be estimated larger, the structure model elucidated from the CTS analysis is unique in the surveyed parameter space and the detailed structure of the metastable state is reliable.

4.4.2. The comparison with previous reports

From the CTS analysis, the structural change of the photoexcited WO_3 in the metastable state should be that one of the shortest bonds among W-O around 1.76 Å in the ground state shrink by 0.09 Å (1.67 ± 0.06 Å). At the same time, the W-O bond in the opposite side which has one of the longest bonds among the W-O bonds should become longer because the WO6 unit in the bulk is assumed. The symmetry of WO6 unit is known as a distorted octahedral in the ground state.[24] As the result of the CTS analysis, the symmetry of the WO6 unit should become worse symmetry from its optical ground state. This result is consistent with the structural model suggested in W L_1-edge XANES analysis.[13] To reveal more details including longer bonds, higher quality measurement is desirable.

4.5. Conclusion

I applied the CTS method to analyze the differences of EXAFS derived from the metastable state of the photoexcited WO_3. Even though the range of EXAFS was short and the degrees of freedom were too low to conduct the conventional CF analysis, the differences of EXAFS of the metastable state was successfully reproduced. In the metastable state, one of the shortest bonds should shrink by 0.09 Å (1.67 ± 0.06 Å) from its original bond length. This structural change in the metastable state makes the symmetry of WO6 unit worse. In addition, the structural change should occur along the crystal axis of a unit cell of WO_3 suggested by the W L_1–edge XANES analysis. I successfully determined this anisotropic structural change quantitatively. In this study, I focused on shrinking of one of the shortest. It is possible to extend the CTS analysis including the elongation of one of the longest W-O bonds if the difference EXAFS is obtained with better quality.

Table 4-1. Survey ranges and steps of parameters for CTS analysis.

Parameter	Constrained thorough search	
	3 shells	4 shells
S_0^2	0.75	
ΔE_0 / eV	17.0	
N_1	2	1
N_2	2	1
N_3	2	2
N_4	-	2
r_1 / Å	1.60-2.30 / 0.01	1.60-1.85 / 0.01
r_2 / Å	1.60-2.30 / 0.01	1.60-1.95 / 0.01
r_3 / Å	1.60-2.30 / 0.01	1.85-2.10 / 0.01
r_4 / Å	-	2.00-2.30 / 0.01
σ^2 /Å^2	$(1.6\times10^{-5})\exp(2.58r_i)$	
condition	$r_1 \le r_2 \le r_3$	$r_1 \le r_2 \le r_3 \le r_4$

Table 4-2. Results of CTS analysis for W L_3-edge EXAFS of WO_3 which measured by transmission mode.

Parameter	Constrained thorough search			Curve fitting	Reference[24]
	3 shells	4 shells (best point)	4 shells	4 shells	
S_0^2	0.75				-
ΔE_0 / eV	17.0				-
N_1	2	1		1	-
N_2	2	1		1	-
N_3	2	2		2	-
N_4	-	2		2	-
r_1 / Å	1.77 ± 0.03	1.77	1.72 ± 0.04	1.75	1.76
r_2 / Å	1.94 ± 0.03	1.77	1.82 ± 0.05	1.75	1.77
r_3 / Å	2.17 ± 0.11	1.93	1.92 ± 0.07	1.91	1.90, 1.91
r_4 / Å	-	2.16	2.17± 0.11	2.16	2.11, 2.17
σ^2 /Å^2	$(1.6\times10^{-5})\exp(2.58r)$				-
R-factor	0.0081	0.0034	0.0097	0.0007*	-

*Digits of parameters for analysis were different.

Table 4-3. Survey ranges and steps of parameters for CTS analysis.

Parameter	Constrained thorough search	
	3 shells	4 shells
S_0^2	0.75	
ΔE_0 / eV	17.0	
N_1	2	1
N_2	2	1
N_3	2	2
N_4	-	2
r_1 / Å	1.60-2.30 / 0.01	1.50-1.90 / 0.01
r_2 / Å	1.60-2.30 / 0.01	1.50-1.90 / 0.01
r_3 / Å	1.60-2.30 / 0.01	1.85-2.10 / 0.01
r_4 / Å	-	2.00-2.30 / 0.01
σ^2 /Å^2	$(6.4\times10^{-6})\exp(3.33r_i)$	
condition	$r_1 \leq r_2 \leq r_3$	$r_1 \leq r_2 \leq r_3 \leq r_4$

Table 4-4. Results of CTS analysis for W L_3-edge EXAFS of WO_3 in the metastable state.

Parameter	Results of CTS analysis		
	3 shells	4 shells (best point)	4 shells
r_1 / Å	1.75 ± 0.02	1.67	1.67 ± 0.06
r_2 / Å	1.99 ± 0.04	1.80	1.80 ± 0.04
r_3 / Å	2.20 ± 0.08	1.95	1.95 ± 0.05
r_4 / Å	-	2.19	2.20 ± 0.08
R-factor	0.0200	0.0009	0.00511

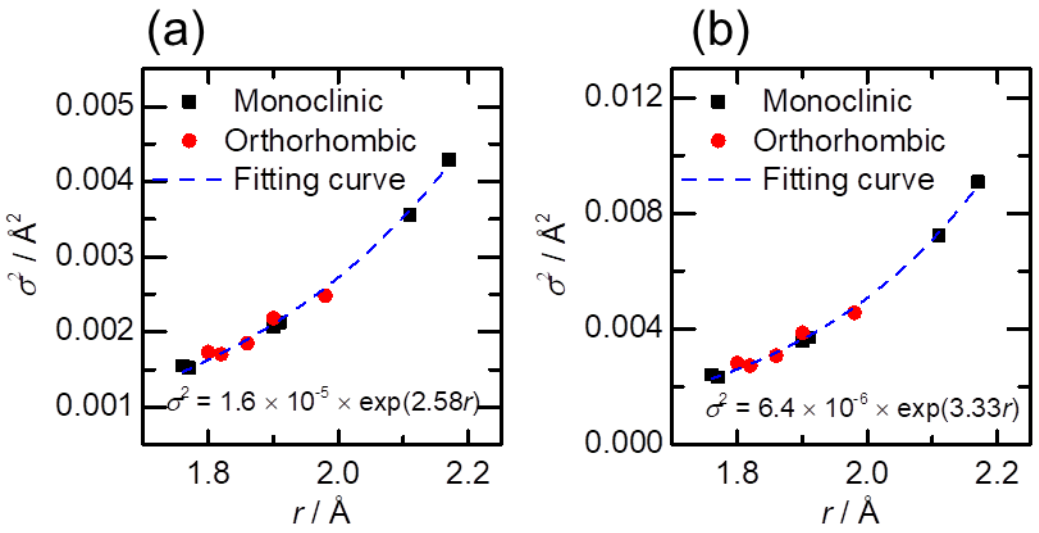

Figure 4-1. Results of the EM method for the W-O bonds of WO_3 for 300K(a) as the ground state and 765 K(b) as the photoexcited state. The dashed line shows the fitted result of Debye Waller factor (σ^2) versus bond distance (r).

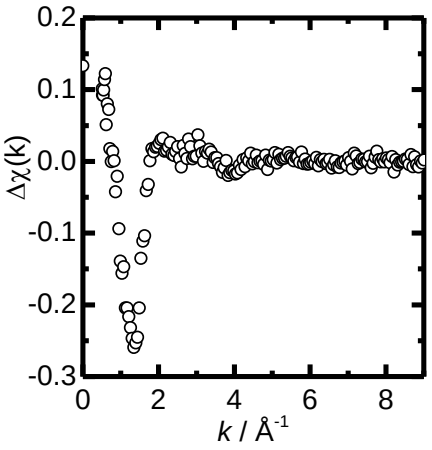

Figure 4-2. Differences of W L_3-edge EXAFS spectra between before and after 150 ps laser irradiation.

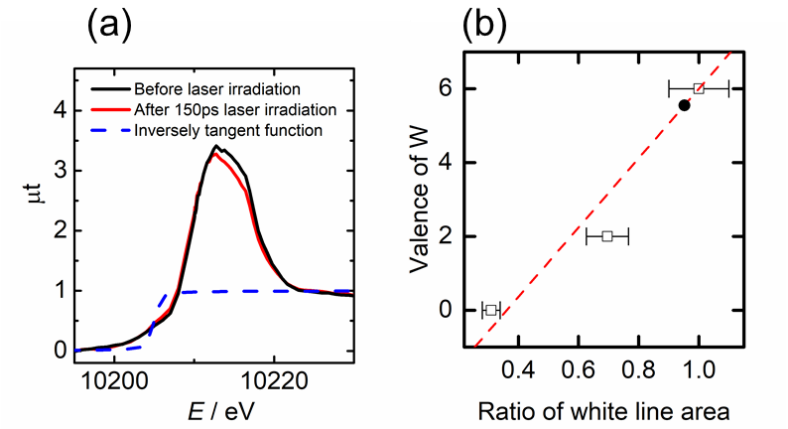

Figure 4-3. (a) W L_3-edge XANES of WO_3 before (black line) and after 150 ps (red line) laser irradiation. Blue dashed line shows the inversely tangent function for the base line. (b) The relationship between the ratio of white line area and valence of W. Black dot shows the result of area ratio calculation for XANES spectra after laser irradiation.

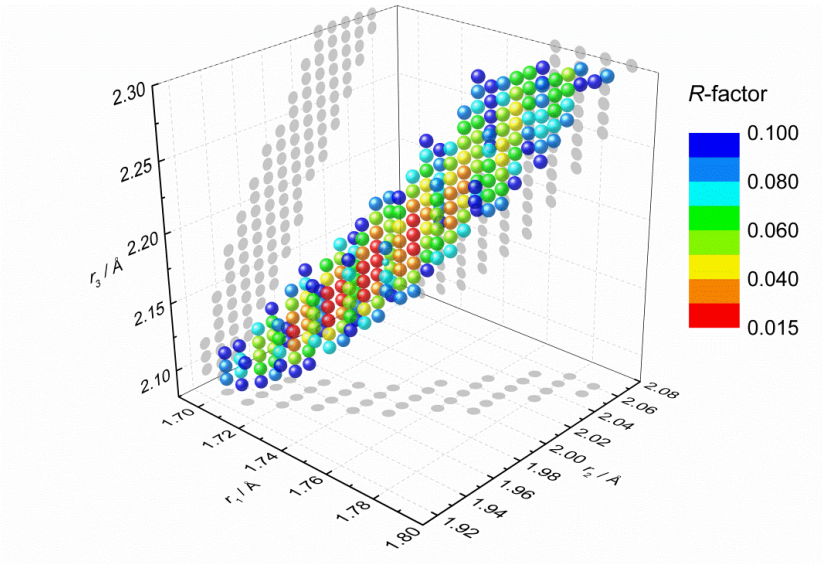

Figure 4-4. 3D mapping of *R*-factor distribution for 3 shells analysis of WO_3 in the metastable state. Color indicates the *R*-factor of the points (r_1, r_2, and r_3). Gray dots are projection of color dots.

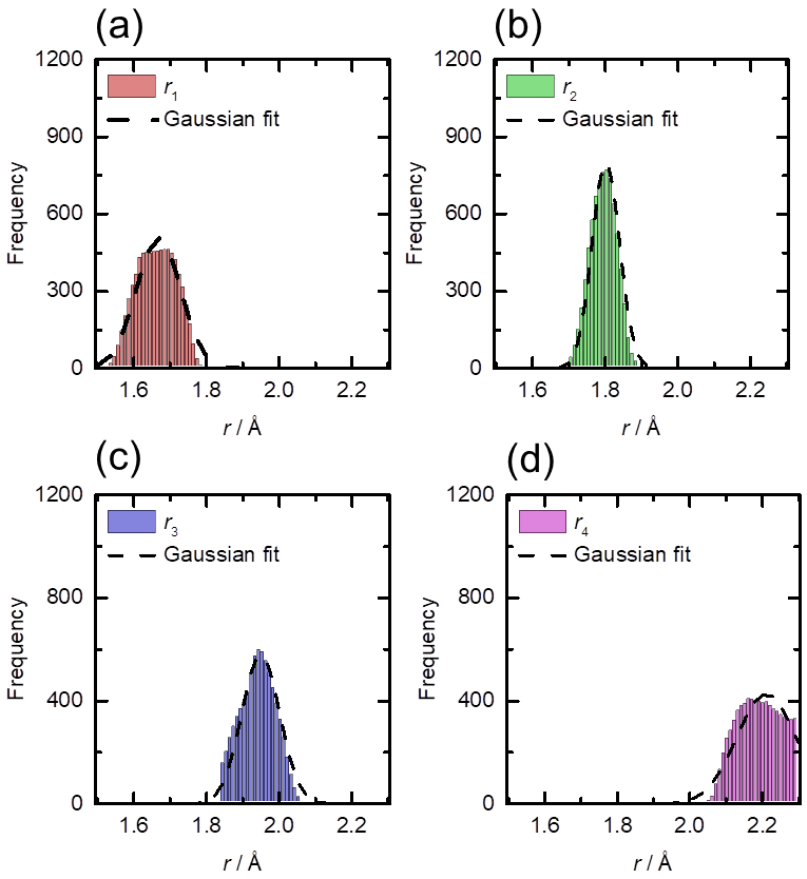

Figure 4-5. Distribution of bond lengths from significance models that satisfied *R*-factor < 0.10. Dashed lines show the fitting results using a Gaussian function.

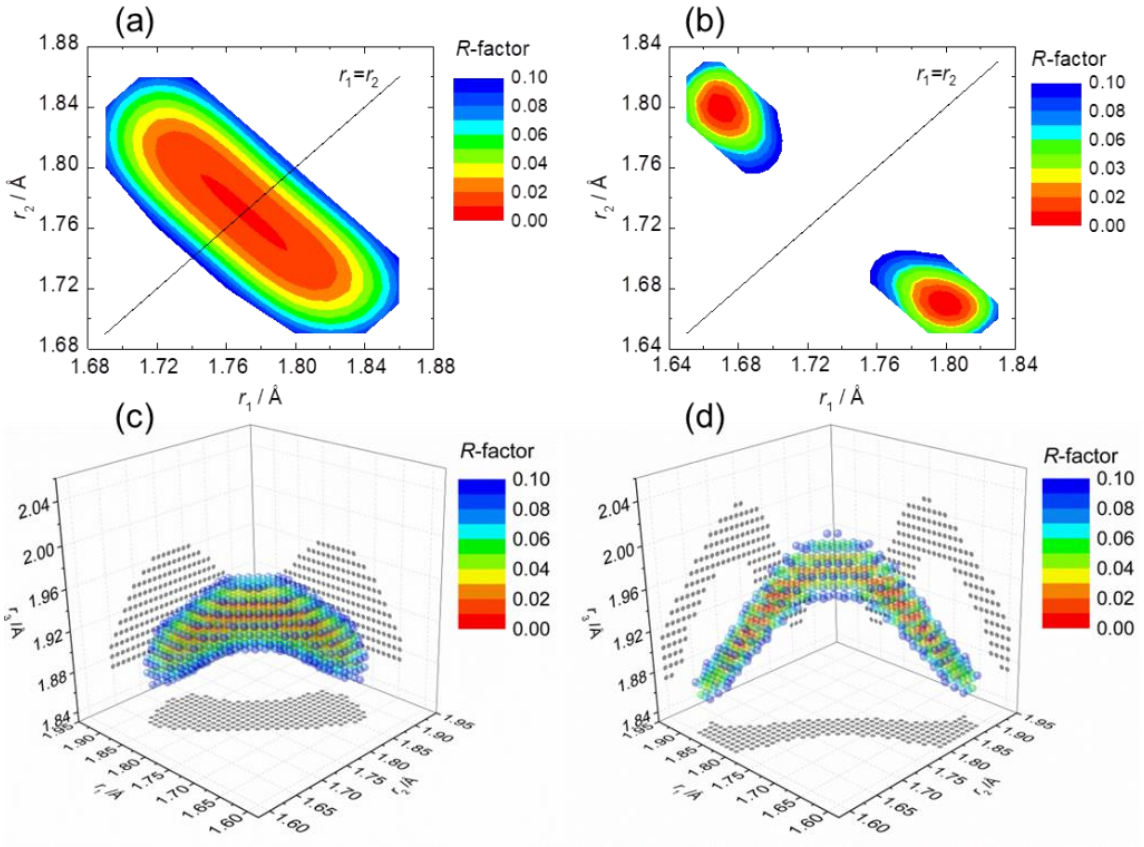

Figure 4-6. (a) and (b) show cross sections of parameter space which cut the global minimum for the ground state and the metastable state of WO_3, respectively. For the ground state, r_3 and r_4 were 1.93 Å and 2.16 Å. For the metastable state, r_3 and r_4 were 1.95 Å and 2.19 Å. (c) and (d) show 3D plot of parameter space for the ground state (r_4=2.16 Å) and the metastable state (r_4=2.19 Å) of WO_3, respectively. Color indicates the *R*-factor of the points. The gray dots are projection of color dots.

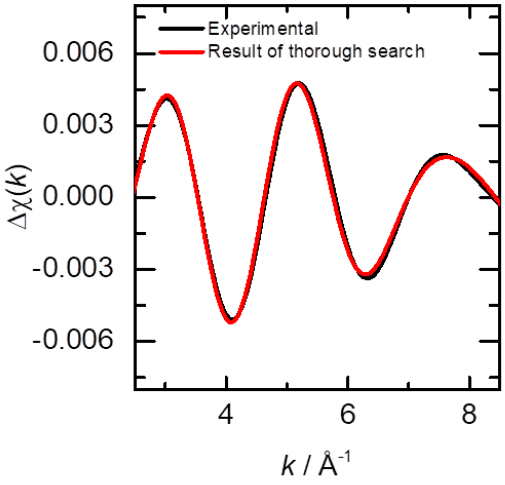

Figure 4-7. The differences of Fourier filtered EXAFS oscillation of experimental data (black line) and calculated from the model of CTS result (red line) for 4 shells' analysis.

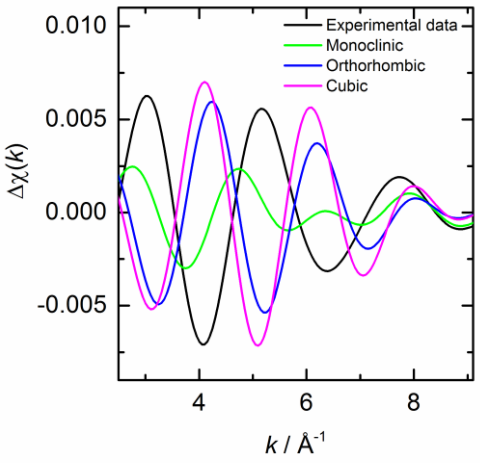

Figure 4-8. Comparison the experimental data and representative structure of WO_3 such as Monoclinic (on high Debye Waller factor), Orthorhombic, and Cubic phase.

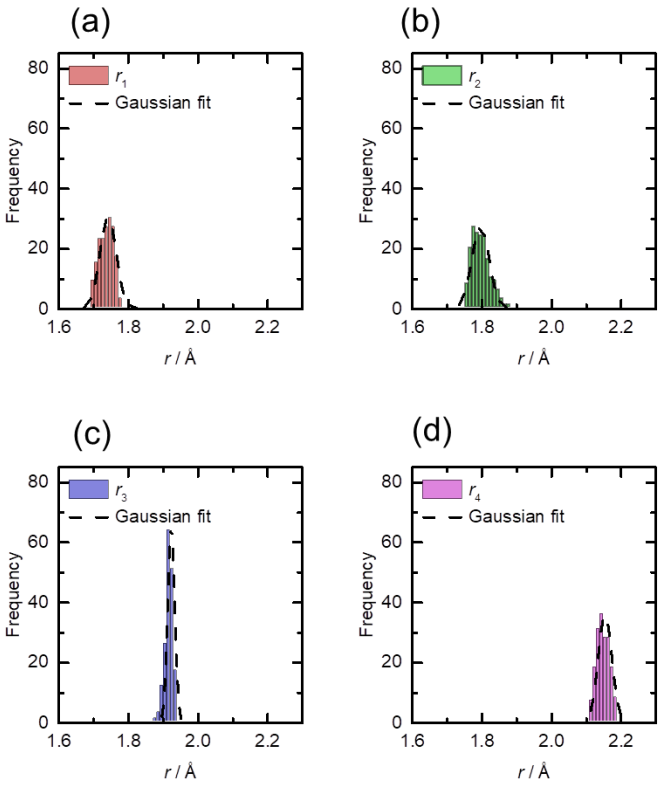

Figure 4-9. Distribution of bond lengths from significance models that satisfied *R*-factor < 0.01 in the CTS analysis for the ground state of WO_3. Dashed lines show the fitting results using a Gaussian function

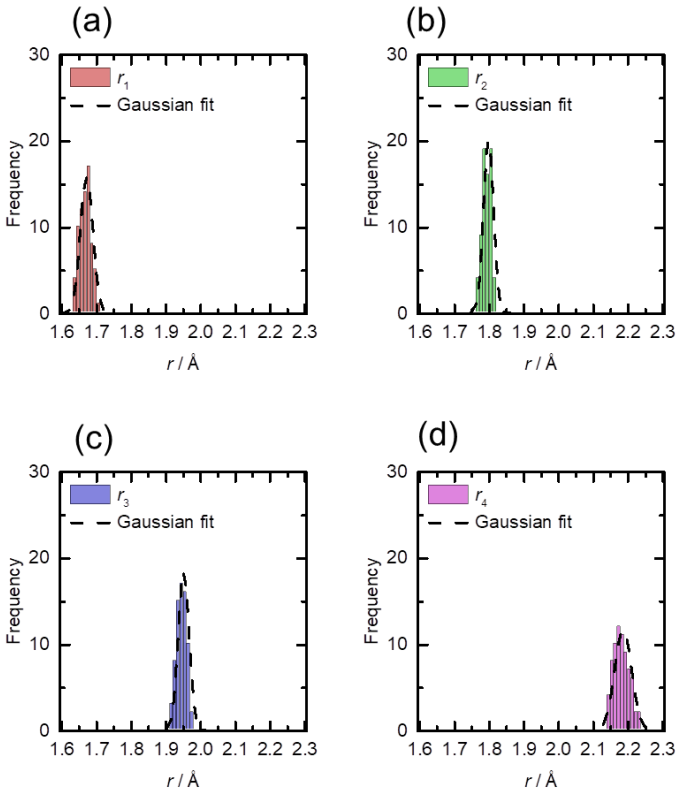

Figure 4-10. Distribution of bond lengths from significance models that satisfied *R*-factor < 0.01 in the thorough search analysis for the photoexcited state of WO_3. Dashed lines show the fitting results using a Gaussian function

Reference

1. Y. Iwasawa, K. Asakura, M. Tada (Eds.), XAFS Techniques for Catalysts, Nanomaterials, and Surfaces, Springer, Cham, 2017.
2. D. Kido, Y. Uemura, Y. Wakisaka, H. Ariga-Miwa, S. Takakuasgi, K. Asakura, Thorough Search Analysis of Extended X-ray Absorption Fine Structure Data for Complex Molecules and Nanomaterials Applications, e-J. Surf. Sci. Nanotech., 18 (2020) 249-261.
3. L.X. Chen, G.B. Shaw, T. Liu, G. Jennings, K. Attenkofer, Exciplex formation of copper(II) octaethylporphyrin revealed by pulsed X-rays, Chem. Phys., 299 (2004) 215-223.
4. R.M. van der Veen, C.J. Milne, A. El Nahhas, F.A. Lima, V.T. Pham, J. Best, J.A. Weinstein, C.N. Borca, R. Abela, C. Bressler, M. Chergui, Structural Determination of a Photochemically Active Diplatinum Molecule by Time-Resolved EXAFS Spectroscopy, Angew. Chem. Int. Edit., 48 (2009) 2711-2714.
5. T. Sato, S. Nozawa, A. Tomita, M. Hoshino, S.Y. Koshihara, H. Fujii, S. Adachi, Coordination and Electronic Structure of Ruthenium(II)-tris-2,2 '-bipyridine in the Triplet Metal-to-Ligand Charge-Transfer Excited State Observed by Picosecond Time-Resolved Ru K-Edge XAFS, J. Phys. Chem. C, 116 (2012) 14232-14236.
6. A. El Nahhas, R.M. van der Veen, T.J. Penfold, V.T. Pham, F.A. Lima, R. Abela, A.M. Blanco-Rodriguez, S. Záliš, A. Vlček, I. Tavernelli, U. Rothlisberger, C.J. Milne, M. Chergui, X-ray Absorption Spectroscopy of Ground and Excited Rhenium–Carbonyl–Diimine Complexes: Evidence for a Two-Center Electron Transfer, J. Phys. Chem. A, 117 (2013) 361-369.
7. X.Y. Zhang, M. Papai, K.B. Moller, J.X. Zhang, S.E. Canton, Characterizing the Solvated Structure of Photoexcited $[Os(terpy)_2]^{2+}$ with X-ray Transient Absorption Spectroscopy and DFT Calculations, Molecules, 21 (2016) 235.
8. T.J. Penfold, J. Szlachetko, F.G. Santomauro, A. Britz, W. Gawelda, G. Doumy, A.M. March, S.H. Southworth, J. Rittmann, R. Abela, M. Chergui, C.J. Milne, Revealing hole trapping in zinc oxide nanoparticles by time-resolved X-ray spectroscopy, Nat. Commun., 9 (2018) 478.
9. J. Hong, T.J. Fauvell, W. Helweh, X. Zhang, L.X. Chen, Investigation of the photoinduced axial ligation process in the excited state of nickel(II) phthalocyanine, J. Photochem. Photobiol. A, Chem., 372 (2019) 270-278.
10. J. Zhang, X. Zhang, K. Suarez-Alcantara, G. Jennings, C.A. Kurtz, L.M. Lawson Daku, S.E. Canton, Resolving the Ultrafast Changes of Chemically Inequivalent Metal–Ligand Bonds in Photoexcited Molecular Complexes with Transient X-ray Absorption Spectroscopy, ACS Omega, 4 (2019) 6375-6381.
11. Y. Uemura, H. Uehara, Y. Niwa, S. Nozawa, T. Sato, S. Adachi, B. Ohtani, S. Takakusagi, K. Asakura, In Situ Picosecond XAFS Study of an Excited State of Tungsten Oxide, Chem. Lett., 43 (2014) 977-979.
12. Y. Uemura, D. Kido, Y. Wakisaka, H. Uehara, T. Ohba, Y. Niwa, S. Nozawa, T. Sato, K. Ichiyanagi, R. Fukaya, S. Adachi, T. Katayama, T. Togashi, S. Owada, K. Ogawa, M. Yabashi, K. Hatada, S. Takakusagi, T. Yokoyama, B. Ohtani, K. Asakura, Dynamics of Photoelectrons and Structural Changes of Tungsten Trioxide Observed

by Femtosecond Transient XAFS, Angew. Chem. Int. Edit., 55 (2016) 1364-1367.
13. A. Koide, Y. Uemura, D. Kido, Y. Wakisaka, S. Takakusagi, B. Ohtani, Y. Niwa, S. Nozawa, K. Ichiyanagi, R. Fukaya, S.I. Adachi, T. Katayama, T. Togashi, S. Owada, M. Yabashi, Y. Yamamoto, M. Katayama, K. Hatada, T. Yokoyama, K. Asakura, Photoinduced anisotropic distortion as the electron trapping site of tungsten trioxide by ultrafast W L1-edge X-ray absorption spectroscopy with full potential multiple scattering calculations, Physical chemistry chemical physics : Phys. Chem. Chem. Phys., 22 (2020) 2615-2621.
14. R. Abe, H. Takami, N. Murakami, B. Ohtani, Pristine simple oxides as visible light driven photocatalysts: highly efficient decomposition of organic compounds over platinum-loaded tungsten oxide, J. Am. Chem. Soc., 130 (2008) 7780-7781.
15. T. Sato, S. Nozawa, K. Ichiyanagi, A. Tomita, M. Chollet, H. Ichikawa, H. Fujii, S.I. Adachi, S.Y. Koshihara, Capturing molecular structural dynamics by 100 ps time-resolved X-ray absorption spectroscopy, J. Synchrotron Rad., 16 (2009) 110-115.
16. T. Taguchi, T. Ozawa, H. Yashiro, REX2000 Yet Another XAFS Analysis Package, Phys. Scr., T115 (2005) 205.
17. J.W.C. Jr., D.E. Sayers, Criteria for automatic x‐ray absorption fine structure background removal, J. Appl. Phys., 52 (1981) 5024-5031.
18. J.J. Rehr, R.C. Albers, Theoretical approaches to x-ray absorption fine structure, Rev. Mod. Phys., 72 (2000) 621-654.
19. M. Newville, Larch: An Analysis Package for XAFS and Related Spectroscopies, J. Phys. Conf. Ser., 430 (2013) 012007.
20. A.V. Poiarkova, J.J. Rehr, Multiple-scattering x-ray-absorption fine-structure Debye-Waller factor calculations, Phys. Rev. B, 59 (1999) 948-957..
21. M. Daniel, B. Desbat, J. Lassegues, B. Gerand, M. Figlarz, Infrared and Raman study of WO3 tungsten trioxides and WO3, xH2O tungsten trioxide tydrates, J. Solid State Chem., 67 (1987) 235-247.
22. I.D. Brown, Recent Developments in the Methods and Applications of the Bond Valence Model, Chem. Rev., 109 (2009) 6858-6919.
23. E.A. Stern, Number of relevant independent points in x-ray-absorption fine-structure spectra, Phys. Rev. B, 48 (1993) 9825.
24. B.O. Loopstra, H.M. Rietveld, Further refinement of the structure of WO3, Acta Crystallographica Section B, 25 (1969) 1420-1421.
25. E. Salje, The orthorhombic phase of WO3, Acta Crystallographica Section B: Structural Crystallography and Crystal Chemistry, 33 (1977) 574-577.

Chapter 5. Application of constrained thorough search method for bimetallic nanoparticles

5.1. Introduction

XAFS is powerful for the characterization of nanoparticles.[1] It is because the crystallinity is not necessary for the sample like XRD. The electronic state of X-ray absorbing atom and structure around it is obtained at the same time. In addition, *in situ* or *operando* measurement can be carried out.[2-4] Not only the single-element nanoparticles, but bimetallic nanoparticles have been investigated.[5-11]

There are constrained conditions in the analysis of EXAFS for bimetallic materials.

1. EXAFS measurement and analysis should be carried out for both elements.

2. Some parameters are constrained each other in two elements' analysis. When the atoms *a* and *b* are the elements of a bimetallic material,

i) Bond length r_{ab} (bond length from atom *a* to atom *b*) and r_{ba} (bond length from atom *b* to atom *a*) satisfy

$$r_{ab} = r_{ba} \tag{5-1}$$

ii) Coordination number N_{ab} (coordination number of *b* from *a*) and N_{ba} (coordination number of *a* from *b*) satisfy

$$N_{ab} = \frac{X_b}{X_a} N_{ba} \quad . \tag{5-2}$$

Here, X_a and X_b are atomic fractions of *a* and *b* in bimetallic material, respectively.

It is very difficult to satisfy these constrained conditions in curve fitting (CF) analysis. The appropriate selections of parameters and well convergence of analysis are necessary at the same time. In addition, the correlations of parameters become more complex. Therefore, it is difficult to obtain the meaningful parameters or many local minima can exist in the parameter space. To analyze EXAFS of bimetallic materials, other analysis methods such as Reverse Monte Calro (RMC) method or combination of *ab initio* and Molecular Dynamics (MD) calculation were carried out.[12,13] In these methods, the

constrained conditions as mentioned above is automatically satisfied because the structural models themselves are treated as parameter. However, these methods are advanced method. The appropriate initial structure is demanded and/or it takes long time for analysis.

Constrained thorough search (CTS) method is a new analysis method for EXAFS of complex materials.[14] In CTS method, parameters are searched step by step in the whole parameter space which estimated theoretically. It seems time consuming but CTS method dose not takes longer time than RMC method. CTS analysis is appropriate method for the EXAFS spectra of bimetallic material. It is because that CTS method can search almost whole parameter space and pick up the candidates which reproduce the experimental data under the constrained condition for the analysis of bimetallic material. In this chapter, I introduced CTS method for analyzing the EXAFS of PtRu nanoparticles and showed the possibility of analyzing the bimetallic materials more simply.

5.2. Experimental

5.2.1. Materials

Two kinds of PtRu/C bimetallic nanoparticles were measured. $PtRu_{1.3}$/KB1600 was purchased from JUKES. The molar ratio of Pt and Ru was Pt:Ru=1:1.3. The size of nanoparticles was 2.8±0.8 nm. Another sample, Pt_2Ru_3/KB800 was purchased from TANAKA Kikinzoku Kogyo (TEC61E54). The molar ratio of Pt and Ru was Pt:Ru=2:3. The size of nanoparticles was 3.5±1.2 nm. EXAFS measurement was carried out under the electrochemical condition. Anodes were PtRu/C catalyst and cathode was Pd/C for both measurements. The measurements were carried out without impressing the currents under the H_2 gas flow condition.

5.2.2. Experimental method

Pt L_3-edge and Ru K-edge EXAFS was measured at beamline BL36XU at SPring-8, Harima, Japan. EXAFS measurement was carried out using Quick XAFS mode. X-ray was monochromatized by Si(111) double crystal monochrometer. Incident X-ray and transmitted X-ray were measured by ionization chambers.

5.2.3. EXAFS analysis

Smoothing the spectra and background removal was carried out using REX2000

(RIGAKU)[15]. Savitzky-Golay method was used for smoothing. Theoretical calculation of the backscattering amplitude and the phase shift were carried out using FEFF8.2 code.[16] CTS analysis was carried out for the Pt L_3-edge EXAFS and Ru K-edge EXAFS, respectively. To reduce the parameter, inelastic loss factor (S_0^2) and the correction of kinetic energy zero (ΔE_0) was obtained from the reference sample. For Pt L_3-edge analysis, S_0^2=1.10 and ΔE_0=6.4 were obtained from Pt L_3-edge EXAFS of Pt foil. For Ru K-edge analysis, S_0^2=1.05 and ΔE_0=-4.6 were obtained from Ru K-edge EXAFS of Ru metal powder. The survey regions and steps were shown in Table 5-1. In the EXAFS analysis of bimetallic material, there are some constrained conditions as mentioned above. To achieve these restrictions two step analysis was carried out. The CTS EXAFS analysis was carried out for each element. Then, the results were combined under the additional constrained conditions. The range of Fourier transformation was 3.0-12.0 $Å^{-1}$ and *k* weight was 3 for both Pt L_3-edge EXAFS and Ru K-edge EXAFS analysis. The range of inversely Fourier transformation was 1.75-3.15 Å and 1.60-2.70 Å for Pt L_3-edge EXAFS and Ru K-edge EXAFS analysis, respectively. The window function of both Fourier transformations was Hanning function.

5.3. Results

Figure 5-1 shows the EXAFS spectra of Pt L_3-edge and Ru K-edge for $PtRu_{1.3}$/KB1600 and Pt_2Ru_3/KB800 samples. The differences between the two samples were obvious around 10-12 $Å^{-1}$ in Pt L_3-edge EXAFS. These spectra were analyzed by CTS method with *R*-factor<0.10 condition. Figure 5-2 and 5-3 show the result of CTS analysis without any additional constrained condition for $PtRu_{1.3}$/KB1600 and Pt_2Ru_3/KB800, respectively. As shown in Figure 5-2 and 5-3, coordination number and Debye Waller factor between Ru and Pt in the Ru K-edge EXAFS cannot be decided in both samples. In addition, the peak position of distribution in the bond length between Pt and Ru in the result of Pt L_3-edge EXAFS analysis ($r_{Pt\text{-}Ru}$) was different from the result of Ru K-edge EXAFS analysis ($r_{Ru\text{-}Pt}$). The constrained conditions for bimetallic sample's EXAFS analysis in the bond length looks satisfied within the error, however, coordination number seems not satisfied the condition. These results means that the separated analysis using the CF method can converge to the meaningless structure which cannot satisfy the constrained conditions for bimetallic material.

To consider the constrained conditions for bimetallic sample's EXAFS analysis, the results of CTS analysis for two edges were combined using the general *R*-factor as following.

$$R\text{-factor}_{PtRu} = a\cdot R\text{-factor}_{Pt} + b\cdot R\text{-factor}_{Ru} + c\cdot\{r_{Pt\text{-}Ru} - r_{Ru\text{-}Pt}\}^2 + d\cdot\{N_{Pt\text{-}Ru} - \frac{X_{Ru}}{X_{Pt}} N_{Ru\text{-}Pt}\}^2 + e\cdot\{\bar{N} - (X_{Pt}N_{Pt} + X_{Ru}N_{Ru})\}^2$$

subject to $N_{Pt} \leq 12$ and $N_{Ru} \leq 12$. (5-3)

Here, *R*-factor $_{Pt}$ and *R*-factor $_{Ru}$ were *R*-factor which obtained from the CTS analysis for Pt L_3-edge EXAFS and Ru-edge EXAFS, respectively. $r_{Pt\text{-}Ru}$ and $r_{Ru\text{-}Pt}$ were bond lengths between Pt and Ru in Pt L_3-edge EXAFS and Ru K-edge EXAFS, respectively. $N_{Pt\text{-}Ru}$ and $N_{Ru\text{-}Pt}$ were coordination numbers between Pt and Ru in Pt L_3-edge EXAFS and Ru K-edge EXAFS, respectively. X_{Pt} and X_{Ru} were ratio of composition in each sample. $\bar{N}$ was the total coordination number between metal and metal neighbors per absorbing atom. $\bar{N}$ was estimated from size of nanoparticles. I estimated $\bar{N}$=10.2 and 10.6 for $PtRu_{1.3}$/KB1600 and Pt_2Ru_3/KB800 samples, respectively. N_{Pt} and N_{Ru} were sum of coordination number ($N_{Pt\text{-}Pt} + N_{Pt\text{-}Ru}$ and $N_{Ru\text{-}Ru} + N_{Ru\text{-}Pt}$) from Pt and Ru, respectively. Constants *a*, *b*, *c*, *d*, and *e* as weight were applied in this analysis. In this chapter, I applied 1, 1, 100, 0.1, and 0.1 for constants *a, b, c, d,* and *e,* respectively. It is expected that the error of each term affects the second decimal of *R*-factor$_{PtRu}$. The limitation of *R*-factor$_{PtRu}$ was 0.10.

Figure 5-4 and Table 5-2 show the result of CTS analysis under the additional constrained condition for $PtRu_{1.3}$/KB1600 sample. As shown in Figure 5-4(c1) and (c2), the shape of distribution became sharper because of the additional constrained condition. The results of CTS analysis satisfied two constrained conditions, or $r_{Pt\text{-}Ru} - r_{Ru\text{-}Pt}$ and $N_{Pt\text{-}Ru} - \frac{X_{Ru}}{X_{Pt}} N_{Ru\text{-}Pt}$, though the results of CTS analysis was introduced from average of picked up distributions. Figure 5-5 and Table 5-3 show the result of CTS analysis with additional constrained condition for Pt_2Ru_3/KB800 sample. The same tendency like $PtRu_{1.3}$/KB1600 sample was obtained. As shown in Figure 5-5(c1) and (c2), the shape of distribution became sharper and the results of CTS analysis satisfied two constrained conditions for bimetallic material.

The distribution of Debye Waller factor between Ru and Pt in the result of Ru K-edge EXAFS was large and cannot fitted Gaussian function well. Theoretically, Debye

Waller factors between the Pt and Ru have an equation. Therefore, I visualized the correlation of Debye Waller factors. Figure 5-6 shows 2D mapping of Debye Waller factors for both PtRu/C samples. $\sigma_{\text{Pt-Ru}}{}^2=\sigma_{\text{Ru-Pt}}{}^2+0.002$ was estimated from these results. Therefore, new term was added to the *R*-factor $_{\text{PtRu}}$ as the constrained condition for Debye Waller factors.

$$R\text{-factor}_{\text{PtRu}} = a\cdot R\text{-factor}_{\text{Pt}} + b\cdot R\text{-factor}_{\text{Ru}} + c\cdot\{r_{\text{Pt-Ru}}-r_{\text{Ru-Pt}}\}^2 + d\cdot\{N_{\text{Pt-Ru}}-\frac{X_{Ru}}{X_{Pt}}N_{\text{Ru-Pt}}\}^2$$
$$+e\cdot\{\bar{N}-(X_{\text{Pt}}N_{\text{Pt}}+X_{\text{Ru}}N_{\text{Ru}})\}^2 + f\cdot\{\sigma_{\text{Pt-Ru}}{}^2-(\sigma_{\text{Ru-Pt}}{}^2+0.002)\}^2$$
$$\text{subject to } N_{\text{Pt}}\leq 12 \text{ and } N_{\text{Ru}}\leq 12. \quad (5\text{-}4)$$

Constants *a*, *b*, *c*, *d*, *e*, and *f* as weight were applied in this analysis. I applied 1, 1, 100, 0.1, 0.1, and 10000 for constants *a*, *b*, *c*, *d*, *e*, and *f*, respectively. The limitation of *R*-factor $_{\text{PtRu}}$ was 0.10.

Figure 5-7 and Table 5-4 show the results of CTS analysis for $PtRu_{1.3}$/KB1600 sample under the constrained condition which was shown in Equation (5-4). As shown in Figure 5-7(c3), the distribution of Debye Waller factor between Ru and Pt in Ru K-edge EXAFS became sharper. Other parameters didn't change largely. As shown in Table 5-4, the *R*-factor $_{\text{Ru}}$ became better. It means the Debye Waller factor was obtained more precisely. Figure 5-8 and Table 5-5 show the results of CTS analysis for Ru_2Pt_3/KB800 sample under the constrained condition as shown in Equation (5-4). As shown in Figure 5-8(c3), the distribution of $\sigma_{\text{Ru-Pt}}{}^2$ in Ru K-edge EXAFS also became sharper. And the *R*-factor $_{\text{Ru}}$ became better without changing other parameters. Therefore, the Debye Waller factor was obtained more precisely, too. As the results of CTS analysis for bimetallic nanoparticles, experimental data were reproduced well as shown in Figure 5-9.

5.4. Discussion

The coordination number is important to obtain the property of bimetallic nanoparticles.[8] In this thesis, three kinds of models, perfect randomly dispersed model, core shell model, and cluster in cluster model, were considered. If the two kinds of atoms are perfect randomly dispersed in a nanoparticle, the average coordination numbers are the same proportion as the bulk concentration. In $PtRu_{1.3}$/KB1600 sample, the ratios of coordination numbers were $N_{\text{Pt-Ru}}/(N_{\text{Pt-Pt}} + N_{\text{Pt-Ru}})$

= 0.40±0.08 and $N_{Pt\text{-}Ru}/(N_{Pt\text{-}Pt} + N_{Pt\text{-}Ru})$ = 0.32±0.08. The molar ratios were $M_{Ru}/(M_{Pt} + M_{Ru})$ = 0.56 and $M_{Pt}/(M_{Pt} + M_{Ru})$ = 0.43. When the ratios were compared, $N_{Pt\text{-}Ru}/(N_{Pt\text{-}Pt} + N_{Pt\text{-}Ru}) \neq M_{Ru}/(M_{Pt} + M_{Ru})$ and $N_{Pt\text{-}Ru}/(N_{Pt\text{-}Pt} + N_{Pt\text{-}Ru}) \neq M_{Pt}/(M_{Pt} + M_{Ru})$. Therefore, the Pt and Ru atoms were not combined randomly in the nanoparticles. The sums of coordination number for each atoms were $N_{Pt} = N_{Pt\text{-}Pt} + N_{Pt\text{-}Ru}$ = 10.4±1.5 and $N_{Ru} = N_{Ru\text{-}Ru} + N_{Ru\text{-}Pt}$ = 10.0±1.4. When the nanoparticles were core shell structure, N_{Pt} or N_{Ru} become 12 or 11.9, respectively. It can be estimated from the size of nanoparticles and the molar ratio. It can be said that $PtRu_{1.3}$/KB1600 sample was not core shell structure. From the results, $N_{Pt\text{-}Pt}$ and $N_{Ru\text{-}Ru}$ were higher than $N_{Pt\text{-}Ru}$ and $N_{Ru\text{-}Pt}$. The cluster in cluster model can be adopted. Therefore, the distributions of Pt and Ru atoms were not the perfect random and the core shell models but the cluster in cluster model. The total of coordination number was 10.2 and the ratio of $N_{Pt\text{-}Ru}$ to $N_{Ru\text{-}Pt}$ was 1.31±0.31. These values were satisfied constrained conditions for bimetallic sample well. In Pt_2Ru_3/KB800 sample, the ratios of coordination numbers were $N_{Pt\text{-}Ru}/(N_{Pt\text{-}Pt} + N_{Pt\text{-}Ru})$ =0.36±0.07 and $N_{Pt\text{-}Ru}/(N_{Pt\text{-}Pt} + N_{Pt\text{-}Ru})$ = 0.24±0.05. The molar ratios were $M_{Ru}/(M_{Pt} + M_{Ru})$ = 0.60 and $M_{Pt}/(M_{Pt} + M_{Ru})$ = 0.40. When the ratios were compared, $N_{Pt\text{-}Ru}/(N_{Pt\text{-}Pt} + N_{Pt\text{-}Ru}) \neq M_{Ru}/(M_{Pt} + M_{Ru})$ and $N_{Pt\text{-}Ru}/(N_{Pt\text{-}Pt} + N_{Pt\text{-}Ru}) \neq M_{Pt}/(M_{Pt} + M_{Ru})$, too. Therefore, it was also estimated that the Pt and Ru atoms were not combined randomly in the nanoparticles in Pt_2Ru_3/KB800 sample. The sums of coordination number for each atoms were $N_{Pt} = N_{Pt\text{-}Pt} + N_{Pt\text{-}Ru}$ = 10.4±1.8 and $N_{Ru} = N_{Ru\text{-}Ru} + N_{Ru\text{-}Pt}$ = 10.7±0.8. In Pt_2Ru_3/KB800 sample, N_{Pt} or N_{Ru} become 12 or 11.7, respectively, when the nanoparticles were core shell structure. From the results of Pt_2Ru_3/KB800, $N_{Pt\text{-}Pt}$ and $N_{Ru\text{-}Ru}$ were higher than $N_{Pt\text{-}Ru}$ and $N_{Ru\text{-}Pt}$. The cluster in cluster model can be adopted. Therefore, the distributions of Pt and Ru atoms were not the perfect random and the core shell models but the cluster in cluster model, too. The total of coordination number was 10.6 and the ratio of $N_{Pt\text{-}Ru}$ to $N_{Ru\text{-}Pt}$ was 1.50±0.38. These values were also satisfied constrained conditions for bimetallic sample. The distribution of Pt and Ru atoms in $PtRu_{1.3}$/KB1600 and Pt_2Ru_3/KB800 were not perfect random or core shell. It is difficult to reveal the detail of distribution. RMC method can be applied to calculate the distribution of Pt and Ru atoms using obtained parameters as the constrained conditions.

As shown in Figure 5-2 and 5-3 which are the results of CTS analysis without any additional constrained condition cannot satisfy the conditions for coordination numbers and bond lengths. Therefore, Equation (5-3) was introduced to consider the constrained conditions for the analysis of bimetallic material. In addition, the constrained condition for Debye Waller factors was considered in Equation (5-4). As

the results of introducing Equation (5-4) to CTS analysis, significant results were obtained. As shown Figure 5-7 and 5-8, the distributions in the results of CTS method were changed. The coordination number and bond length between Ru and Pt in Ru K-edge EXAFS in both PtRu/C samples were largely changed. And the distribution of Debye Waller factor between Pt and Ru in Ru K-edge EXAFS also became sharp. The results of CTS analysis were satisfied constrained condition for bimetallic material, of course. In $PtRu_{1.3}$/KB1600 sample, $r_{Pt\text{-}Ru}=2.74\pm0.01\approx r_{Ru\text{-}Pt}=2.73\pm0.01$ Å, $N_{Pt\text{-}Ru}/N_{Ru\text{-}Pt}=1.31\pm0.31$, and $X_{Pt}N_{Pt}+X_{Ru}N_{Ru}=10.2$. In Pt_2Ru_3/KB800 sample, $r_{Pt\text{-}Ru}=r_{Ru\text{-}Pt}=2.72\pm0.01$ Å, $N_{Pt\text{-}Ru}/N_{Ru\text{-}Pt}=1.50\pm0.38$, and $X_{Pt}N_{Pt}+X_{Ru}N_{Ru}=10.6$. The results of CTS analysis with additional constrained condition reproduced experimental data well as shown in Figure 5-9. The problem remains in *R*-factor $_{PtRu}$ is how to decide the weight for each term. These constants were decided from following estimation. For constant *c*, I expected that the 0.01 Å order difference between $r_{Pt\text{-}Ru}$ and $r_{Ru\text{-}Pt}$ is accepted and this difference affects to *R*-factor $_{PtRu}$ in 0.01 order so that 100 was applied. For constant *d*, I expected that the difference between $N_{Pt\text{-}Ru}$ and $N_{Ru\text{-}Pt}$ is accepted in 0.5 to 1.0 and this difference affects to *R*-factor $_{PtRu}$ in 0.01 order so that 0.1 was applied. For constant *e*, I expected that the same order as the constant *d*. For constant *f*, I expected that the difference between $\sigma_{Pt\text{-}Ru}^2$ and $\sigma_{Ru\text{-}Pt}^2+0.002$ is accepted in $0.002Å^2$ order and this difference affects to *R*-factor $_{PtRu}$ in 0.01 order so that 10000 was applied. There is a possibility that these constants are optimized like the LASSO method.[17] The another problem is optimization of survey ranges and steps. In this thesis, the distributions of coordination number were treated as one domain though it seems two peaks. The survey steps for coordination number were 1.0 to reduce the mass of calculation. Though the constrained conditions for bimetallic materials were satisfied and the significant results were obtained, it can be optimized to check the distribution of coordination number more precisely.

5.5. Conclusion

The CTS method was applied to the analysis of Pt L_3-edge and Ru K-edge EXAFS of PtRu/C samples, $PtRu_{1.3}$/KB1600 and Pt_2Ru_3/KB800. There were constrained conditions among the parameters for analyses of bimetallic materials. The general *R*-factor, *R*-factor$_{PtRu}$, were introduced to obtain the significant parameters under the constrained condition for bimetallic materials. As the result of analysis, significant parameters were obtained and reproduced the experimental data well. It is expected that the distribution of Pt and Ru atoms were cluster in cluster model in both sample.

Table 5-1. Surveyed range and steps of parameters for CTS analysis. M in the table is the element of measurement (Pt or Ru).

Parameter	Pt L_3-edge	Ru K-edge
S_0^2	1.10	1.05
$N_{\text{M-Pt}}$ $N_{\text{M-Ru}}$	1.0-12.0 / 1.0	1.0-12.0 / 1.0
ΔE_0 / eV	6.4	-4.6
$r_{\text{M-Pt}}$ / Å $r_{\text{M-Ru}}$ / Å	2.60-2.80 / 0.01	2.60-2.80 / 0.01
$\sigma^2_{\text{M-Pt}}$ / Å^2 $\sigma^2_{\text{M-Ru}}$ / Å^2	0.002-0.026 / 0.002	0.002-0.026 / 0.002

Table 5-2. The results of CTS analysis for $PtRu_{1.3}$/KB1600 sample under the additional constrained condition, Equation (5-3). M in the table is the element of measurement (Pt or Ru).

Parameter	Pt L_3-edge	Ru K-edge
S_0^2	(1.10)	(1.05)
$N_{\text{M-Pt}}$	6.3 ± 1.3	3.3 ± 0.6
$N_{\text{M-Ru}}$	4.3 ± 0.6	6.7 ± 1.4
ΔE_0 / eV	(6.4)	(-4.6)
$r_{\text{M-Pt}}$ / Å	2.74 ± 0.01	2.74 ± 0.01
$r_{\text{M-Ru}}$ / Å	2.74 ± 0.01	2.67 ± 0.01
$\sigma^2_{\text{M-Pt}}$ / Å^2	0.013 ± 0.003	0.014 ± 0.010
$\sigma^2_{\text{M-Ru}}$ / Å^2	0.011 ± 0.002	0.007 ± 0.001
R-factor $_{\text{M}}$	0.030	0.024

Table 5-3. The results of CTS analysis for Pt_2Ru_3/KB800 sample under the additional constrained condition, Equation (5-3). M in the table is the element of measurement (Pt or Ru).

Parameter	Pt L_3-edge	Ru K-edge
S_0^2	(1.10)	(1.05)
$N_{M\text{-}Pt}$	6.3 ± 1.6	2.6 ± 0.5
$N_{M\text{-}Ru}$	3.9 ± 0.4	8.1 ± 1.3
ΔE_0 / eV	(6.4)	(-4.6)
$r_{M\text{-}Pt}$ / Å	2.75 ± 0.01	2.72 ± 0.01
$r_{M\text{-}Ru}$ / Å	2.72 ± 0.01	2.67 ± 0.01
$\sigma^2_{M\text{-}Pt}$ / Å^2	0.010 ± 0.003	0.009 ± 0.006
$\sigma^2_{M\text{-}Ru}$ / Å^2	0.008 ± 0.002	0.008 ± 0.001
R-factor $_M$	0.034	0.028

Table 5-4. The results of CTS analysis for $PtRu_{1.3}$/KB1600 sample under the additional constrained condition, Equation (5-4). M in the table is the element of measurement (Pt or Ru).

Parameter	Pt L_3-edge	Ru K-edge
S_0^2	(1.10)	(1.05)
$N_{M\text{-}Pt}$	6.2 ± 1.4	3.2 ± 0.6
$N_{M\text{-}Ru}$	4.2 ± 0.6	6.8 ± 1.3
ΔE_0 / eV	(6.4)	(-4.6)
$r_{M\text{-}Pt}$ / Å	2.74 ± 0.01	2.73 ± 0.01
$r_{M\text{-}Ru}$ / Å	2.74 ± 0.01	2.67 ± 0.01
$\sigma^2_{M\text{-}Pt}$ / Å^2	0.012 ± 0.003	0.009 ± 0.002
$\sigma^2_{M\text{-}Ru}$ / Å^2	0.011 ± 0.002	0.007 ± 0.001
R-factor $_M$	0.027	0.009

Table 5-5. The results of CTS analysis for Pt_2Ru_3/KB800 sample under the additional constrained condition, Equation (5-4). M in the table is the element of measurement (Pt or Ru).

Parameter	Pt L_3-edge	Ru K-edge
S_0^2	(1.10)	(1.05)
$N_{M\text{-}Pt}$	6.5 ±1.8	2.6 ± 0.6
$N_{M\text{-}Ru}$	3.9 ± 0.4	8.1 ± 0.6
ΔE_0 / eV	(6.4)	(-4.6)
$r_{M\text{-}Pt}$ / Å	2.75 ± 0.01	2.72 ± 0.01
$r_{M\text{-}Ru}$ / Å	2.72 ± 0.01	2.67 ± 0.01
$\sigma^2_{M\text{-}Pt}$ / Å^2	0.010 ± 0.003	0.006 ± 0.001
$\sigma^2_{M\text{-}Ru}$ / Å^2	0.008 ± 0.001	0.008 ± 0.001
R-factor $_M$	0.032	0.012

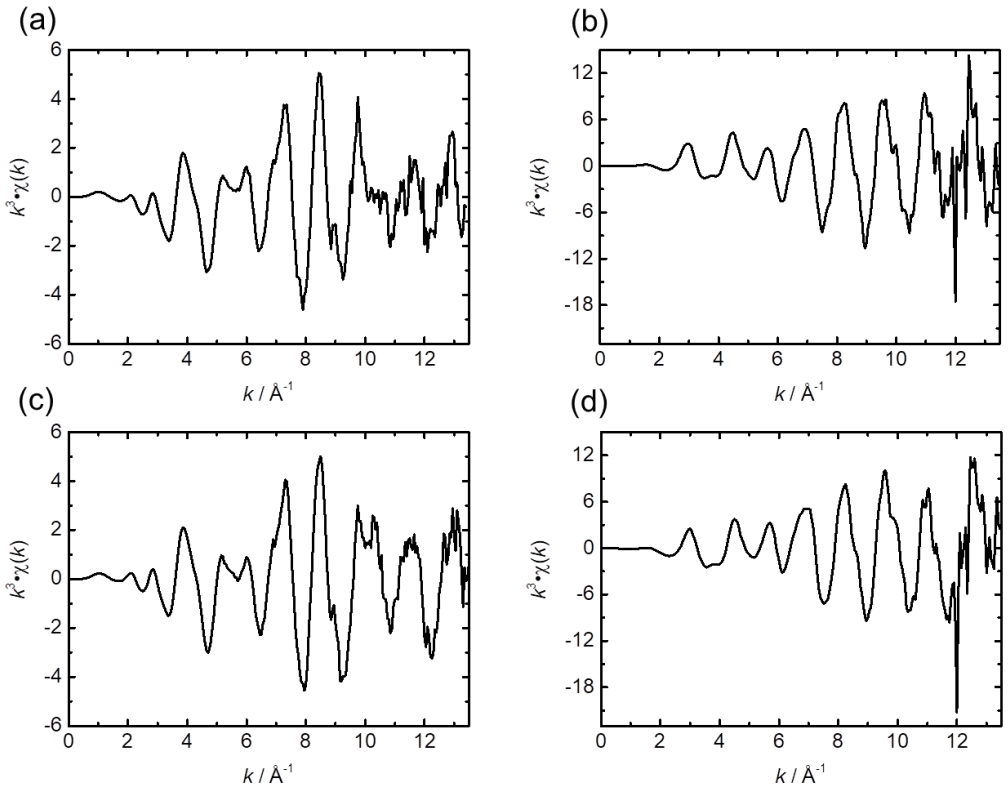

Figure 5-1. EXAFS spectra of (a) Pt L_3-edge and (b) Ru K-edge EXAFS of $PtRu_{1.3}$/KB1600 sample, (c) Pt L_3-edge and (d) Ru K-edge EXAFS of Pt_2R_3/KB800 sample, respectively.

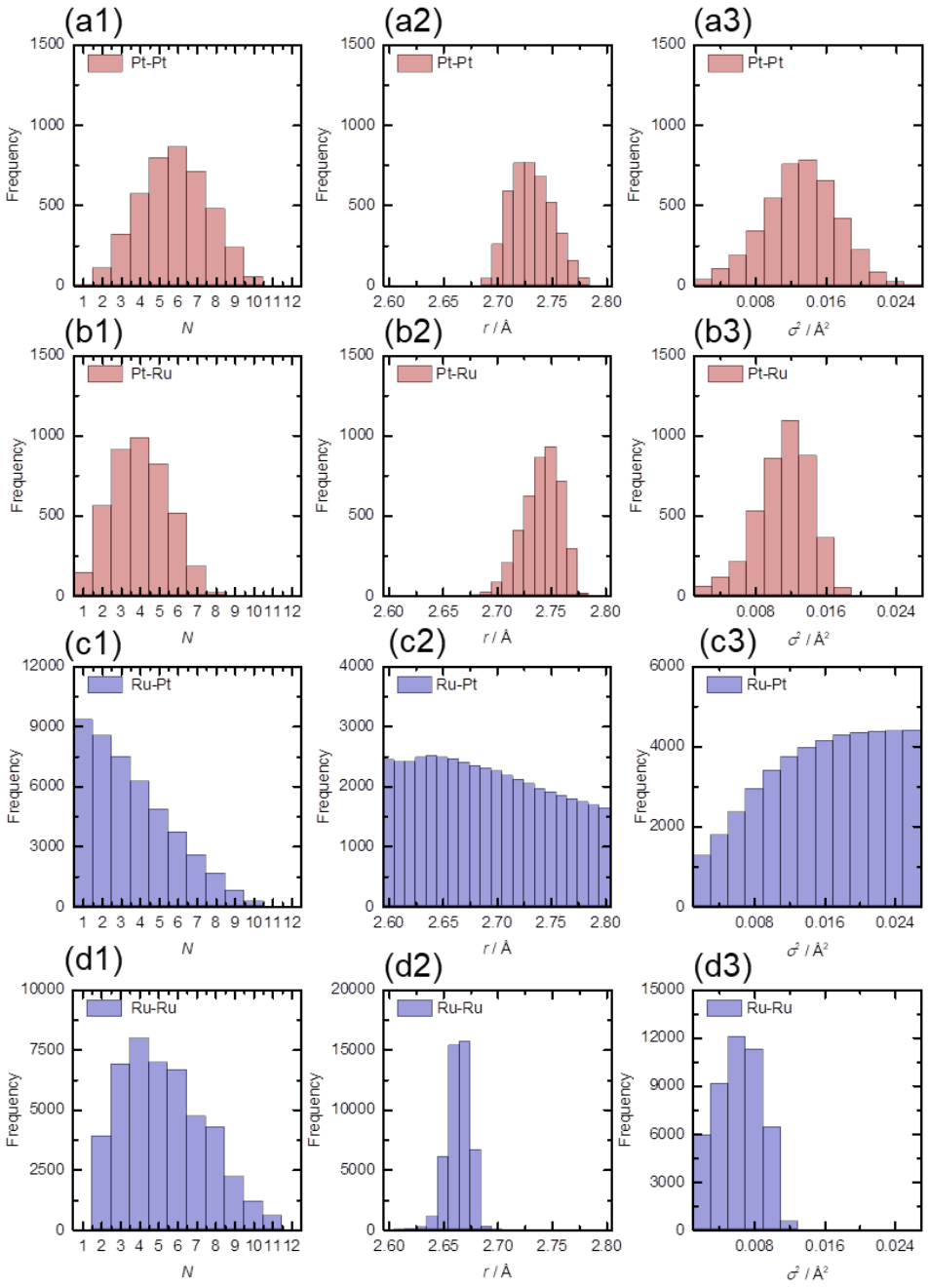

Figure 5-2. Frequency distribution of CTS analysis for Pt L_3-edge EXAFS (red) and Ru K-edge EXAFS (blue) of $PtRu_{1.3}$/KB1600 sample. The parameters which satisfied *R*-factor $_{PtRu}$ < 0.10 were picked up without any constrained conditions for bimetallic materials.

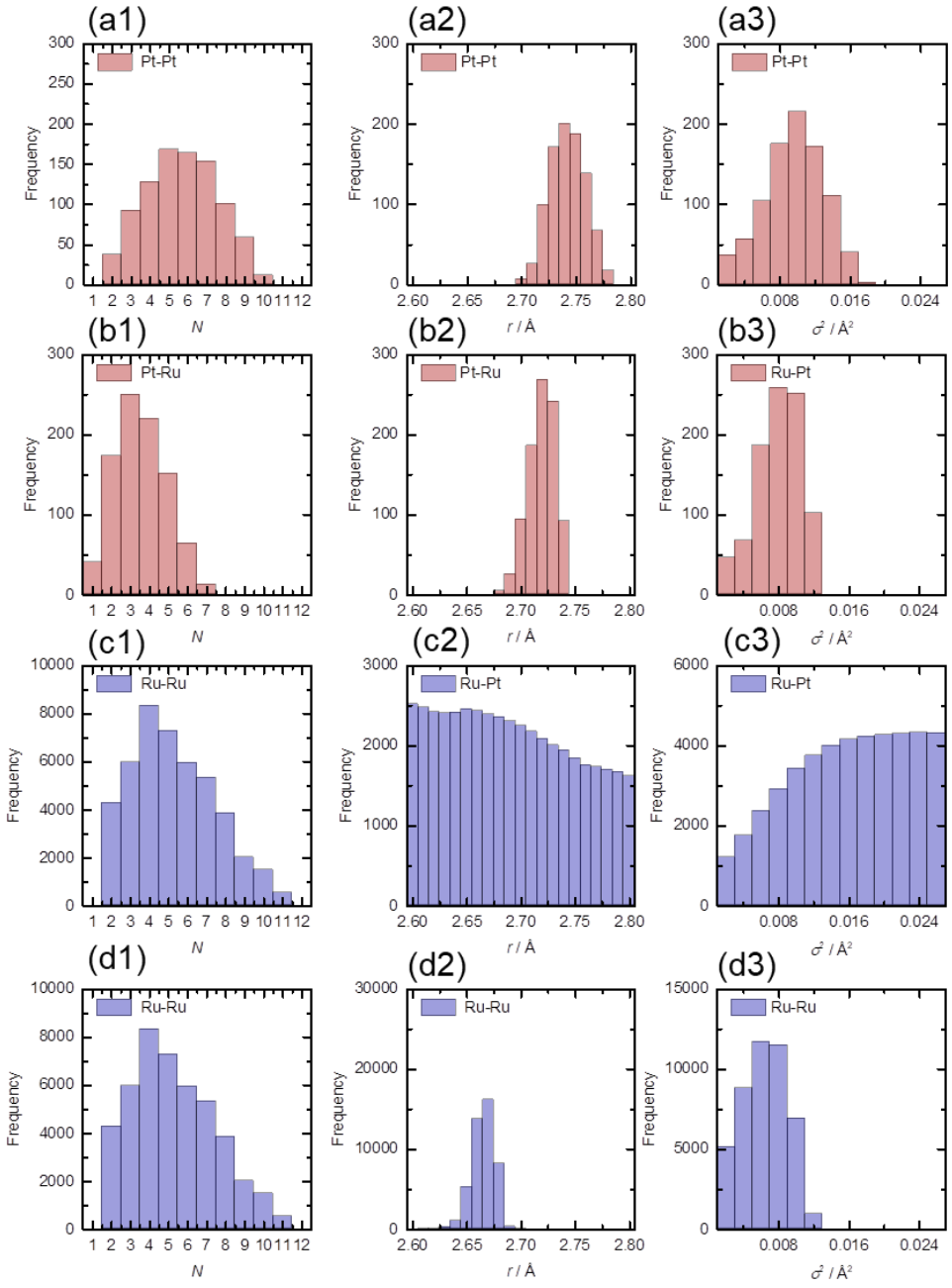

Figure 5-3. Frequency distribution of CTS analysis for Pt L_3-edge EXAFS (red) and Ru K-edge EXAFS (blue) of Pt_2Ru_3/KB800 sample. The parameters which satisfied *R*-factor $_{PtRu}$ < 0.10 were picked up without any constrained conditions for bimetallic materials.

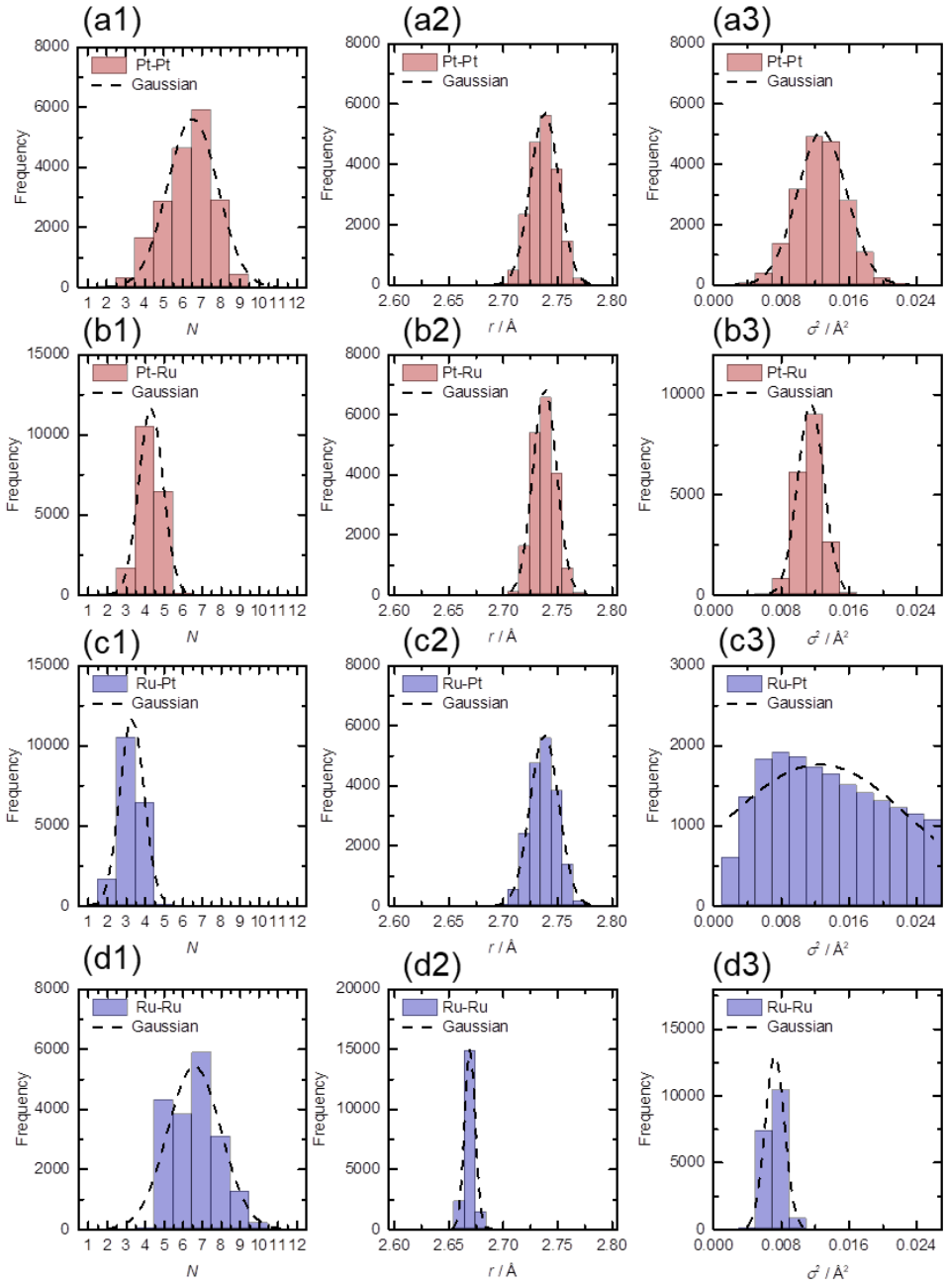

Figure 5-4. Frequency distribution of CTS analysis for Pt L_3-edge EXAFS (red) and Ru K-edge EXAFS (blue) of $PtRu_{1.3}$/KB1600 sample. The parameters which satisfied *R*-factor $_{PtRu}$ < 0.10 were picked up with constrained conditions for bond length and coordination number. Dashed line shows the results of Gaussian fitting.

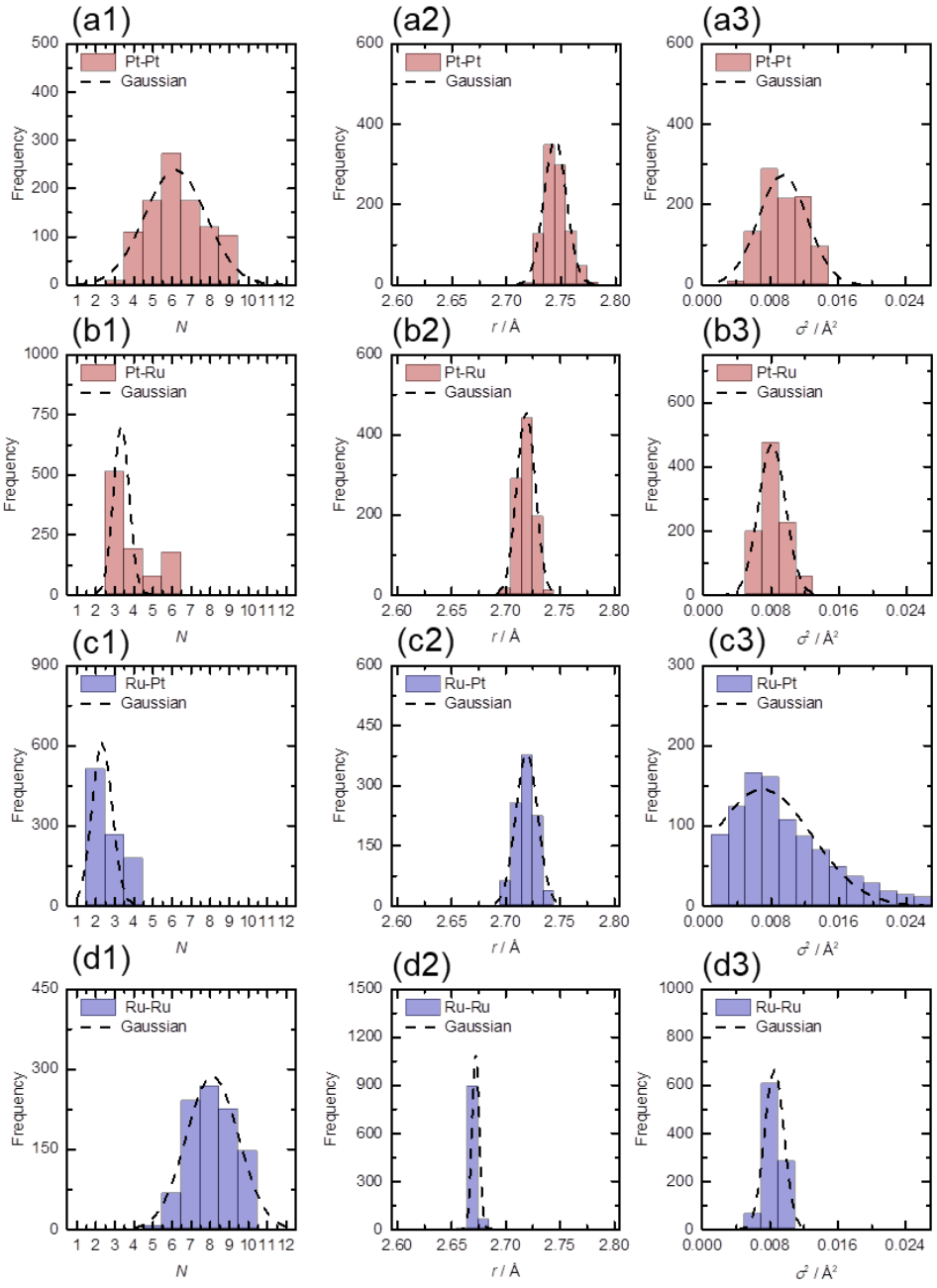

Figure 5-5. Frequency distribution of CTS analysis for Pt L_3-edge EXAFS (red) and Ru K-edge EXAFS (blue) of Pt_2Ru_3/KB800 sample. The parameters which satisfied *R*-factor $_{PtRu}$ < 0.10 were picked up with constrained conditions for bond length and coordination number. Dashed line shows the results of Gaussian fitting.

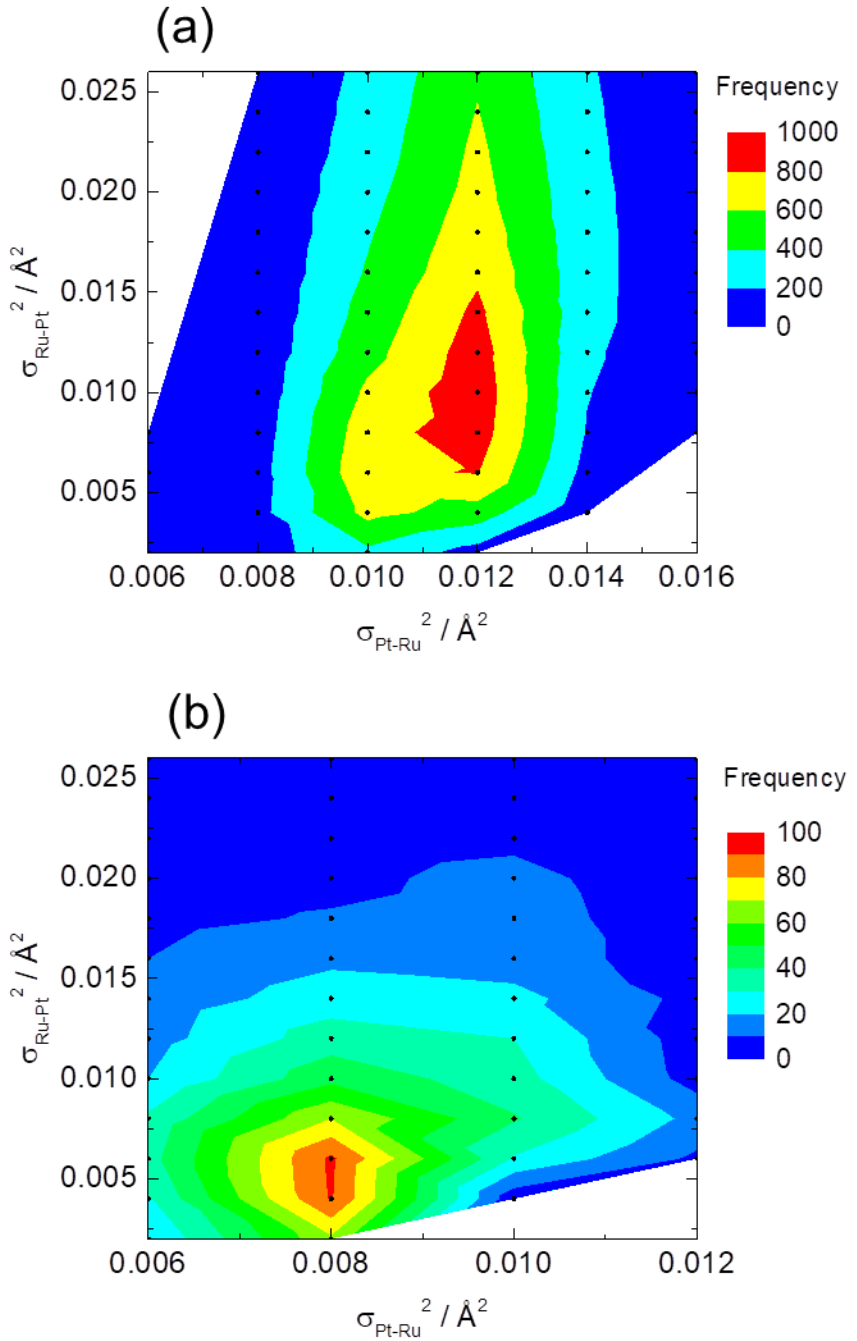

Figure 5-6. 2D plot between Debye-Waller factors ($\sigma_{Pt\text{-}Ru}^2$ and $\sigma_{Ru\text{-}Pt}^2$) for (a)$PtRu_{1.3}$/KB1600 and (b)Pt_2Ru_3/KB800 samples. Dots show the position of search.

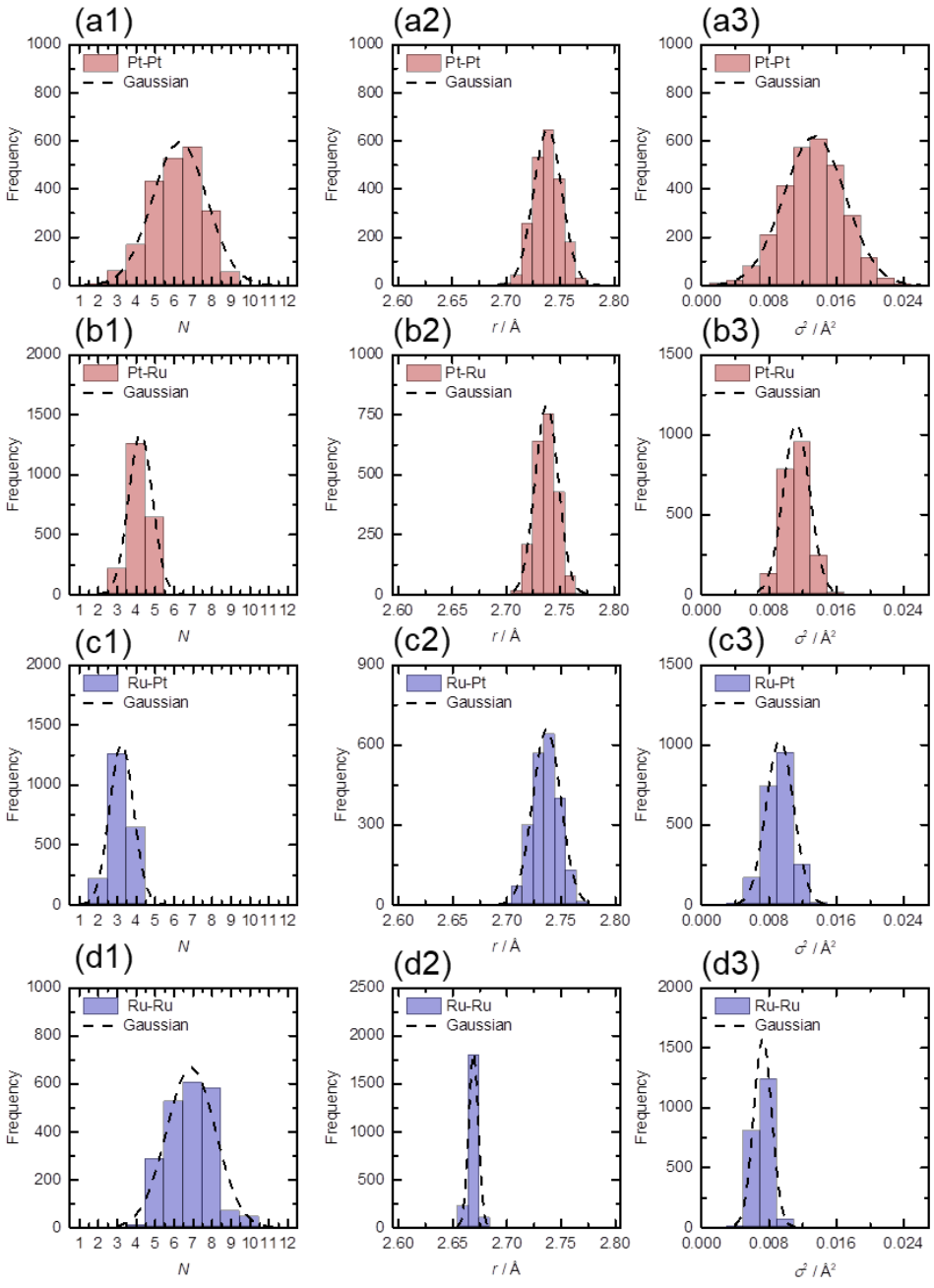

Figure 5-7. Frequency distribution of CTS analysis for Pt L_3-edge EXAFS (red) and Ru K-edge EXAFS (blue) of $PtRu_{1.3}$/KB1600 sample. The parameters which satisfied *R*-factor $_{PtRu}$ < 0.10 were picked up with constrained conditions for bond length, coordination number and Debye Waller factor. Dashed line shows the results of Gaussian fitting.

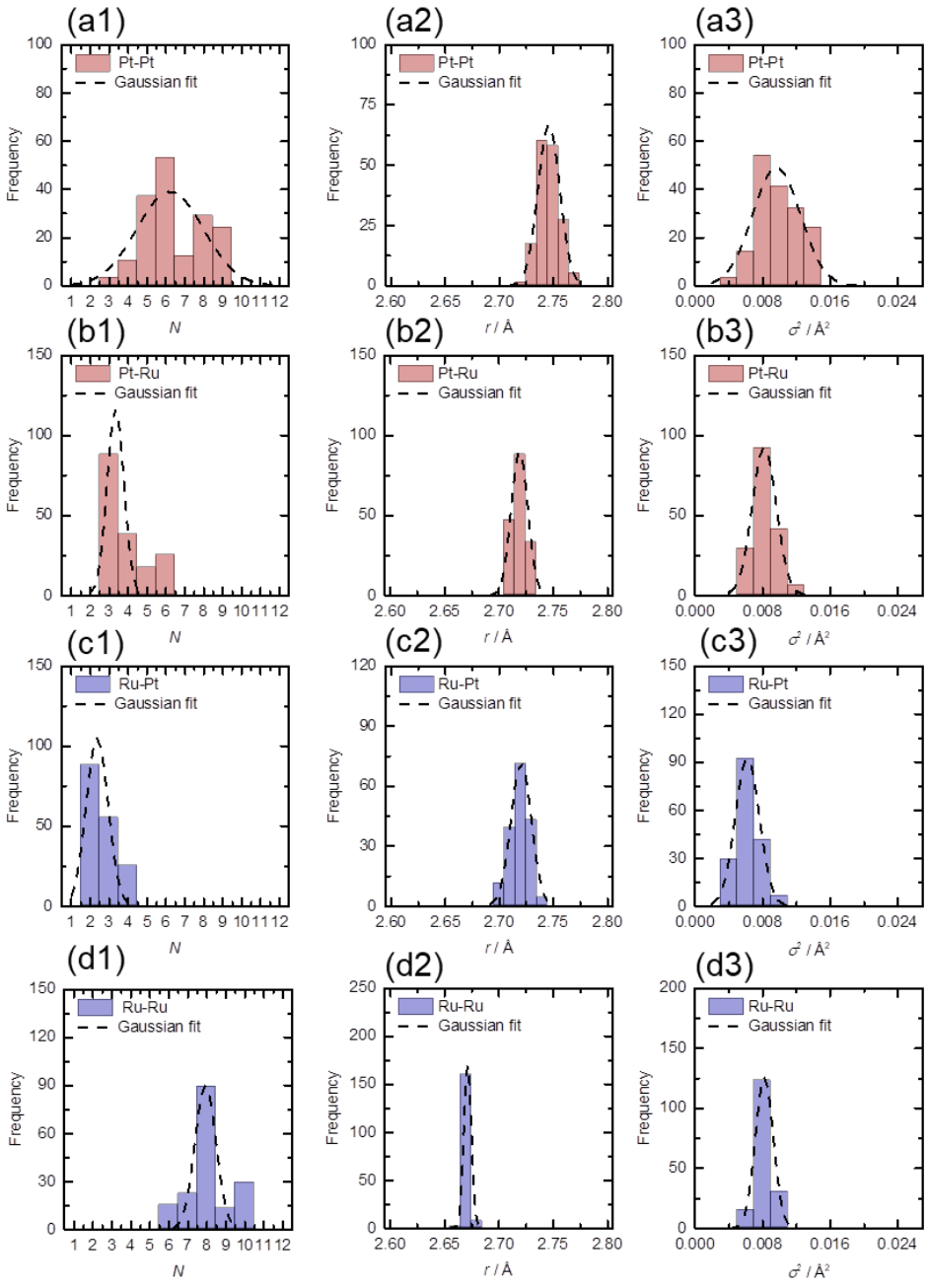

Figure 5-8. Frequency distribution of CTS analysis for Pt L_3-edge EXAFS (red) and Ru K-edge EXAFS (blue) of Pt_2Ru_3/KB800 sample. The parameters which satisfied *R*-factor $_{PtRu}$ < 0.10 were picked up with constrained conditions for bond length, coordination number and Debye Waller factor. Dashed line shows the results of Gaussian fitting.

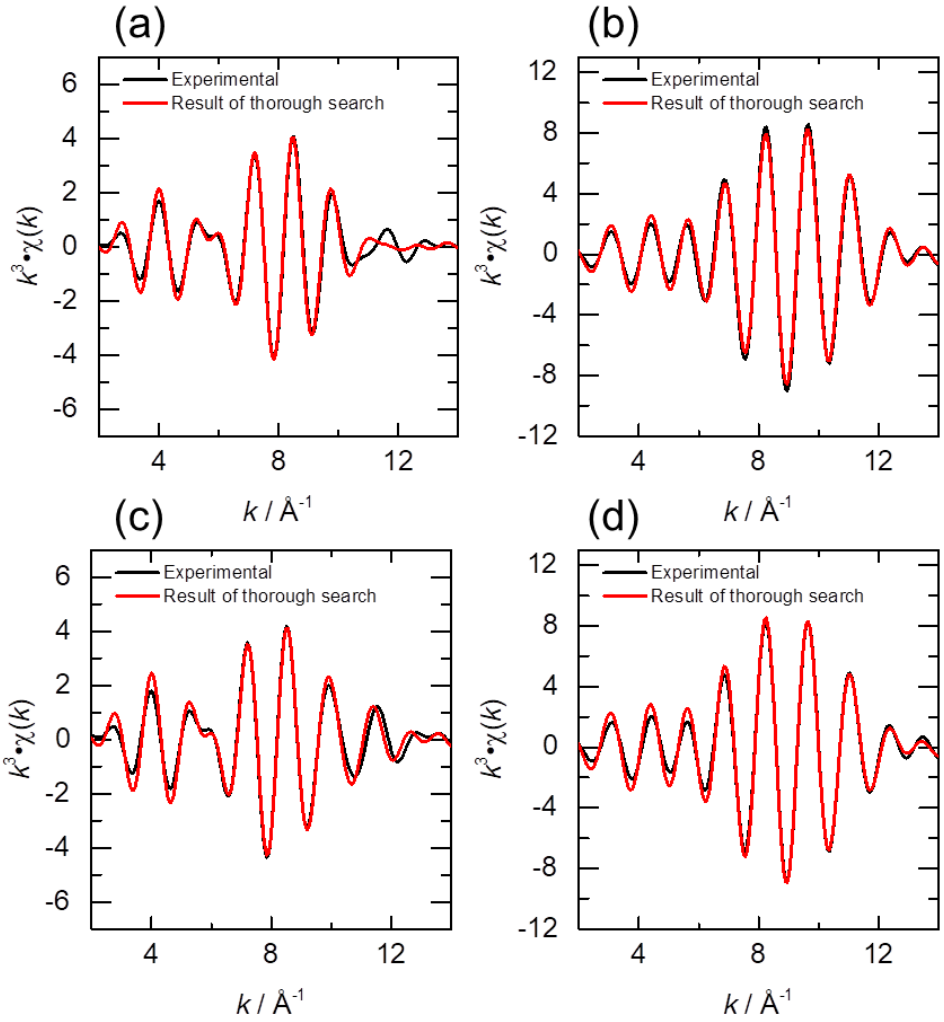

Figure 5-9. Comparison between the experimental data and the results of CTS analysis for EXAFS spectra of (a) Pt L_3-edge and (b) Ru K-edge EXAFS of $PtRu_{1.3}$/KB1600 sample, (c) Pt L_3-edge and (d) Ru K-edge EXAFS of Pt_2Ru_3/KB800 sample, respectively.

Reference

1. Y. Iwasawa, K. Asakura, M. Tada, XAFS techniques for catalysts, nanomaterials, and surfaces, Springer, 2017.
2. M. Tada, S. Murata, T. Asakoka, K. Hiroshima, K. Okumura, H. Tanida, T. Uruga, H. Nakanishi, S.-I. Matsumoto, Y. Inada, M. Nomura, Y. Iwasawa, In Situ Time-Resolved Dynamic Surface Events on the Pt/C Cathode in a Fuel Cell under Operando Conditions, Angew. Chem. Int. Ed., 46 (2007) 4310-4315.
3. H. Uehara, Y. Uemura, T. Ogawa, K. Kono, R. Ueno, Y. Niwa, H. Nitani, H. Abe, S. Takakusagi, M. Nomura, Y. Iwasawa, K. Asakura, In situ back-side illumination fluorescence XAFS (BI-FXAFS) studies on platinum nanoparticles deposited on a HOPG surface as a model fuel cell: a new approach to the Pt-HOPG electrode/electrolyte interface, Phys. Chem. Chem. Phys., 16 (2014) 13748-13754.
4. S. Yamashita, Y. Yamamoto, H. Kawabata, Y. Niwa, M. Katayama, Y. Inada, Dynamic chemical state conversion of nickel species supported on silica under CO–NO reaction conditions, Catal. Today, (2017).
5. G.H. Via, K.F. Drake, G. Meitzner, F.W. Lytle, J.H. Sinfelt, Analysis of EXAFS data on bimetallic clusters, Catal. Lett., 5 (1990) 25-33.
6. N. Toshima, M. Harada, Y. Yamazaki, K. Asakura, Catalytic activity and structural analysis of polymer-protected gold-palladium bimetallic clusters prepared by the simultaneous reduction of hydrogen tetrachloroaurate and palladium dichloride, The Journal of Physical Chemistry, 96 (1992) 9927-9933.
7. E.P. Maris, W.C. Ketchie, M. Murayama, R.J. Davis, Glycerol hydrogenolysis on carbon-supported PtRu and AuRu bimetallic catalysts, J. Catal., 251 (2007) 281-294.
8. A.I. Frenkel, Applications of extended X-ray absorption fine-structure spectroscopy to studies of bimetallic nanoparticle catalysts, Chem. Soc. Rev., 41 (2012) 8163-8178.
9. T. Takeguchi, T. Yamanaka, K. Asakura, E.N. Muhamad, K. Uosaki, W. Ueda, Evidence of Nonelectrochemical Shift Reaction on a CO-Tolerant High-Entropy State Pt–Ru Anode Catalyst for Reliable and Efficient Residential Fuel Cell Systems, J. Am. Chem. Soc., 134 (2012) 14508-14512.
10. T. Kaito, H. Mitsumoto, S. Sugawara, K. Shinohara, H. Uehara, H. Ariga, S. Takakusagi, Y. Hatakeyama, K. Nishikawa, K. Asakura, K-Edge X-ray Absorption Fine Structure Analysis of Pt/Au Core–Shell Electrocatalyst: Evidence for Short Pt–Pt Distance, J. Phys. Chem. C, 118 (2014) 8481-8490.
11. T. Kaito, H. Tanaka, H. Mitsumoto, S. Sugawara, K. Shinohara, H. Ariga, H.

Uehara, S. Takakusagi, K. Asakura, In Situ X-ray Absorption Fine Structure Analysis of PtCo, PtCu, and PtNi Alloy Electrocatalysts: The Correlation of Enhanced Oxygen Reduction Reaction Activity and Structure, J. Phys. Chem. C, 120 (2016) 11519-11527.

12. J. Timoshenko, K.R. Keller, A.I. Frenkel, Determination of bimetallic architectures in nanometer-scale catalysts by combining molecular dynamics simulations with x-ray absorption spectroscopy, The Journal of Chemical Physics, 146 (2017) 114201.
13. J. Timoshenko, Z. Duan, G. Henkelman, R.M. Crooks, A.I. Frenkel, Solving the Structure and Dynamics of Metal Nanoparticles by Combining X-Ray Absorption Fine Structure Spectroscopy and Atomistic Structure Simulations, Annual Review of Analytical Chemistry, 12 (2019) 501-522.
14. D. Kido, Y. Uemura, Y. Wakisaka, H. Ariga-Miwa, S. Takakuasgi, K. Asakura, Thorough Search Analysis of Extended X-ray Absorption Fine Structure Data for Complex Molecules and Nanomaterials Applications, e-J. Surf. Sci. Nanotech., 18 (2020) 249-261.
15. T. Taguchi, T. Ozawa, H. Yashiro, REX2000 Yet Another XAFS Analysis Package, Phys Scripta, T115 (2005) 205.
16. J.J. Rehr, R.C. Albers, Theoretical approaches to x-ray absorption fine structure, Rev. Mod. Phys., 72 (2000) 621-654.
17. R. Tibshirani, Regression Shrinkage and Selection via the Lasso, Journal of the Royal Statistical Society. Series B (Methodological), 58 (1996) 267-288.

Chapter 6. General Conclusion

EXAFS has been widely used to reveal the structures of many kinds of materials such as nanoparticle catalysts. However, conventional analysis method, or curve fitting (CF) method have problems especially for analyzing the EXAFS of complex materials. The large problems are 1) limitation of degrees of freedom, 2) correlations of parameters, and 3) dependence of initial parameter. In addition, local minima in parameter space sometimes can show the correct structure especially for complex material. I have tried solving these problems and developed the new analysis method, "Constrained Thorough Search" (CTS) method.

In chapter 3, I introduced the CTS method and compared it with CF method and micro Reverse Monte Carlo (m-RMC) method. Pt L_3-edge EXAFS of Pt foil and Mo K-edge EXAFS of α-MoO_3 powder were analyzed as the example of simple case and complex structure, respectively. The significant results were obtained and the limitation of CTS method was revealed with changing parameters on Pt L_3-edge EXAFS analysis. The candidates which reproduced experimental data were obtained from Mo K-edge EXAFS analysis and selected correct one combining with bond valence theory. From these results, the advantages and disadvantages of CTS method were revealed. The important advantages of CTS method are 1) to search the whole parameter space, or independent of the selection of initial parameters, 2) to visualize the distribution of the parameter space and their correlation, 3) to pick up the local minima to confirm that the obtained structure is unique or not in the parameter space, and 4) to automatically consider the limitation of degree of freedom. These advantages overcome the problems of the CF analysis, or parameter correlation and dependence of initial parameter. On the other hand, disadvantages are 1) to take much time to search the whole parameter space, and 2) to treat huge data. However, a recent development of computer hardware has lessened these disadvantages and these may not be the practical problems.

In chapter 4, I analyzed the picosecond time-resolved EXAFS to reveal the structural change of WO_3 in the photoexcited state. W L_3-edge EXAFS spectrum of WO_3 was changed in the photoexcitation. The range of EXAFS was limited. However, the detail of structural change was obtained using CTS method. It was insured that the structural model which reproduced the experimental data well in searched parameter space was only one to apply the CTS method. As the result of CTS analysis, the

shortest W-O bond became 0.09 Å shorter with the photoexcitation was obtained. It means that the symmetry around W ion became worse in the photoexcited state. This result was consistent with the result which reported from W L_1-edge XANES timeresolved measurement.

In chapter 5, I analyzed the EXAFS spectra of PtRu bimetallic nanoparticles. There were additional constrained conditions among the parameters in two EXAFS, Pt L_3-edge and Ru K-edge. When the two EXAFS were analyzed separately, the additional constrained conditions for bimetallic materials were not satisfied. Therefore, I introduced general *R*-factor to pick up the significance models under the additional constrained conditions. The general *R*-factor consisted of 6 terms, or 2 terms for *R*-factor in separately analyses, 2 terms for coordination numbers, 1 term for bond lengths and 1 term for Debye Waller factors. As the result of CTS analyses with general *R*-factor, the structures of bimetallic materials were obtained with satisfying constrained conditions well.

I developed the new analysis method, “Constrained Thorough Search” method, for EXAFS analysis. As the results, two problems of CF analysis, 2) correlations of parameters, and 3) dependence of initial parameter were solved. Especially, the visualization of candidates in the parameter space was revolutionary for EXAFS analysis. The problem 1) limitation of degree of freedoms was not solved by CTS method. This problem mainly depends on the quality of experimental data. However, the limitation of degrees of freedom was automatically included in CTS method. CTS method didn’t show the meaningful result when the number of parameters were larger than degrees of freedom. Therefore, CTS method is useful especially for beginners of EXAFS analysis because it is difficult for beginners to obtain significant results with dealing with these problems.

As shown in chapter 4 and 5, the complex structures such as the WO_3 in the photoexcited state and PtRu bimetallic nanoparticles were obtained by CTS method. From the results of chapter 4, it is expected that the CTS method has advantages in the analysis of the structural change because the survey range can be estimate easily. In case of Quick XAFS measurement, continuous changes of EXAFS spectra can be obtained. The number of spectra is 100 or more. It is hard work for analyzing the 100 spectra using CF method, one by one. However, CTS method has the potential to analyze all spectra. For example, two steps procedure can be considered. At first, the EXAFS spectra of initial and final state of change are analyzed by CTS method. Then, the procedure of the change can be traced using the created theoretical calculations

during the CTS analysis. On the other hand, from the results of chapter 5, it is expected that the two results which measured or calculated with different method can be combined such as the combination of EXAFS analysis of CTS method and DFT calculation. In chapter 4, additional constrained conditions between the results and parameters between the EXAFS spectra of two absorption edges with general *R*-factor. This general *R*-factor can be applied to the combination between the results of EXAFS and another method. However, the constants for general *R*-factor need to be improved even though the combination of two EXAFS spectra. Therefore, more consideration for general *R*-factor is needed to realize the combination of another method.

The goal of CTS method is to search the almost whole parameter space and to pick up the candidates which reproduce the experimental data well with their statistical probability. I would like to extract all significant parameters from an EXAFS spectrum and then select the meaningful structure which consistent with other experimental and/or theoretical results. This goal is based on the idea that if all local minima in the parameter space which reproduced experimental data in certain significance level are picked up and evaluated, the arbitrariness which can be included by selection of initial parameter should be removed. To achieve searching the almost whole parameter space, the decision of survey range and steps and the improvement of searching speed are important. As shown in chapter 3, the procedure that rough step search following by fine step search worked well. The selection of parameters was appropriate and meaningful result was obtained. However, it is difficult to choose appropriate parameters for unknown samples. Ideally, fine steps search for whole estimated parameter range is the best way. Therefore, the improvement of calculation speed is important. This improvement can be achieved by optimization of hardware and software. In present script, the memory and CPU of PC is concerned with the speed of calculation directly from the aspect of hardware. The threads for multiprocessing is decided by the number of core in CPU. Therefore, usage of supercomputer such as “Fugaku” is the best way in the aspect of hardware. On the other hand, the programing language and script is concerned with the speed from the aspect of software. Python is used for present calculation and its calculating speed is slower than C++ because Python is interpreter type language. Cython can combine the C++ and Python. Therefore, to introduce or combine another programing language is one of the solutions. As mentioned above, present script use the CPU for calculating. Recently, machine learning which treats the huge data is carried out using GPU (Graphic Processing Unit) because GPU has more cores than CPU. Thus, to modify the scripts for using GPU is another way. On the other hand, it is difficult to pick up

the candidates with their statistical probability. In this thesis, I introduced *R*-factor to obtain the degree of fitting and decide the limitation as 0.10. As mentioned in chapter 3, to introduce the χ^2 test is almost impossible because the calculation of standard deviation is difficult. One of the solutions is the Hamilton's method. It is used in chapter 3. However, when the degrees of freedom were very small such as the WO_3 in the photoexcited state case, very bad results such as *R*-factor = 0.80 can be picked up in 0.05 significance level. On the other hand, there was no candidate when the χ^2 test is applied with 0.05 significance level from the strictly estimation of standard deviation. Another reason to make the statistical treatment difficult is that the multidimensional parameter space has to be considered for the EXAFS analysis. The histograms for each parameter are approximated to the projection of parameter vs. *R*-factor space. However, the limitation of visualization of parameters' correlation is 3 dimensions as shown in chapter 3. Another evaluation method should be considered. Ideal treatment is introduction of weight coefficients. If weight coefficients for all parameters are applied, the histograms can represent the projection of parameter vs. *R*-factor space more precisely. In addition, the precision of the CTS method also will become higher. One of the ideas for weight coefficient is ratio of *R*-factor of a parameter set to *R*-factor of the best in a searched parameter space. This idea is based on Hamilton's method and I would like to try introducing such weight coefficient as the future plan.

The problems such as the speed of calculation, the decision of significant level, and the optimizations of the general *R*-factor remain. However, CTS method has the potential to analyze more complex structure with high precision and to contribute the development of characterizations in chemistry, nanomaterial science, and so on.

Acknowledgement

In my works described in this thesis was supported by a lot of people from not only Hokkaido University but many facilities. First, I would like to express my gratitude to my supervisor, Prof. Kiyotaka Asakura. I wouldn't meet very attractive theme without him. He gave me many opportunities to challenge including this research topic and guided me to proceed with my research. He gave me not only the many supports for research and this thesis but many suggestions to enrich my life.

I would like to make acknowledgement to Dr. Yohei Uemura in Paul Scherrer Institute, Switzerland, for many supports. He gave me fruitful suggestions and discussions. In the beamtime at Photon Factory and SPring-8, he helped me during the long time experiments. I also express thank to Prof. Tatsuya Takeguchi, in Iwate University for providing me interesting EXAFS spectra of PtRu samples and discussing the results.

I also greatly appreciate Associate Prof. Satoru Takakusagi and Assistant Prof. Hiroko Ariga-Miwa for their advice, technical supports and encouragement. I would also like to thank members of Prof. Asakura's group who spent the same time. They gave me many fruitful discussions and technical supports. Especially, I would like to thank Dr. Yuki Wakisaka for his support and discussion.

I would like to thank all professors and staffs in Division of Quantum Science and Engineering, Institute for Catalysis, Photon Factory, and SPring-8 (including SACLA).

Finally, I would like to greatly thank my family for all supports and encouragement.